

Alma Mater Studiorum – Università di Bologna

DOTTORATO DI RICERCA IN  
SCIENZE DELLA TERRA DELLA VITA E DELL'AMBIENTE

Ciclo 29

**Settore Concorsuale di afferenza: 04/A3**

**Settore Scientifico disciplinare GEO/05**

INVESTIGATING THE DEFORMATION OF SLOW MOVING LANDSLIDES  
IN THE NORTHERN APENNINES OF ITALY WITH DIFFERENTIAL  
INTERFEROMETRY (INSAR)

**Presentata da: Benedikt Bayer**

**Coordinatore Dottorato**

**Barbara Mantovani**

**Relatore**

**Alessandro Simoni**

**Esame finale anno 2017**



**Titolo Tesi di Dottorato: Investigating the deformation of slow moving landslides in the northern Apennines of Italy with differential interferometry (INSAR)**

Il dott. Benedikt Bayer si è laureato in Geologia e Territorio il 13/12/2013 presso l'Università di Bologna con voti 110/110 e lode, discutendo la tesi: "Carta geomorfologica di Vidiciatico (Bo) con ausilio di tecniche di telerilevamento.". Da Gennaio 2014 a Dicembre 2016 ha svolto la propria attività relativa al Dottorato di Ricerca in Scienze della Terra, della Vita e dell'Ambiente (XXIX ciclo), Università di Bologna (Tutor Alessandro Simoni) occupandosi dello studio della Investigazione degli spostamenti di frane a movimento lento nell'Appennino Settentrionale tramite interferometria radar (InSAR).

**PRESENTAZIONE DELLA TESI**

Il lavoro si è concentrato sull'analisi di grandi frane a cinematica lenta nell'Appennino Settentrionale. Per la misura degli spostamenti a scala regionale e locale è stata usata una tecnica remote sensing conosciuta come interferometria radar da satellite (InSAR). I movimenti gravitativi selezionati sono stati oggetto di rilevamento geologico-geomorfologico sul campo cui è seguita l'attenta interpretazione del meccanismo deformativo. Partendo da tecniche esistenti e codici a libero accesso, il candidato ha testato le potenzialità e i limiti tramite analisi di sensitività sui numerosi parametri coinvolti. Il lavoro comprende anche la modifica dei codici esistenti e lo sviluppo di nuovi codici per il trattamento di dati satellitari recentemente introdotti (Sentinel 1A.). Il lavoro si è poi concentrato su alcuni casi selezionati tra cui movimenti gravitativi indotti da scavi in sotterraneo. In questo caso, la ricerca si è concentrata sulla relazione tra spostamenti superficiali e posizione dello scavo della gallerie, velocità di avanzamento e forzante climatica. A scala regionale, sono state analizzate le risposte deformative alle precipitazioni stagionali e le differenti cinematiche di frane profonde che interessano i litotipi più comuni nell'area di studio.

Durante il periodo di dottorato, il dott. Benedikt Bayer ha inoltre svolto:

- periodo all'estero: Earth and Space Science Dept., University of Washington, Seattle, USA, September 2014 - February 2015. Prof. David Schmidt.

- congressi:

AGU Fall meeting San Francisco 14.-19 December 2014;

EGU General Assembly 2016 17-22 Aprile (Vienna);

International Symposium on landslides 2016, Napoli, Italy - 12-17 June, 2016;

AIGA 2016: Convegni degli ricercatori nella geologia applicata, Bologna.

- attività didattica:

Seminario: Introduzione della tecnica Interferometria radar (nell'ambito del corso di telerilevamento tenuto da F. Brardinoni).

Seminario: Esempi di applicazione dell'interferometria da satellite (nell'ambito del corso di Geologia Tecnica tenuto da A. Simoni).

- pubblicazioni:

Benedikt Bayer, Alessandro Simoni, David Schmidt, Lara Bertello, Matteo Berti Mauro Generali, Marco Pizziolo (2016). Ground surface deformations induced by tunneling on a deep-seated landslides in the Northern Apennines of Italy imaged using advanced InSAR techniques. *Landslides and Engineered Slopes. Experience, Theory and Practice. Proceeding of the International Symposium on landslides 2016, Napoli, Italy - 12-17 June, 2016. Vol. 2, pp. 363-370.*

Mulas M., Bayer B., Bertolini G., Bettelli G., Bonacini F., Leuratti E., Pizziolo M., Simoni A., & Corsini, A. (2016). Impulsive ground movements in the mud volcanoes area of "Le Sarse" (Northern Apennines, Modena province, Italy): field evidences and multi-approach monitoring. *Rendiconti online della Società Geologica Italiana, 41, 251-254.*

Villi F., Bayer B., Simoni A., Schmidt D. (2016). Long-term deformation of slow moving landslides in the Northern Apennines of Italy imaged by SAR interferometry. *Rendiconti online della Società Geologica Italiana, 41, 263-266.*

B. Bayer; D. Schmidt; A. Simoni; (2017) "The Influence of External Digital Elevation Models on PS-InSAR and SBAS Results: Implications for the Analysis of Deformation Signals Caused by Slow Moving Landslides in the Northern Apennines (Italy)," in *IEEE Transactions on Geoscience and Remote Sensing*, vol.PP, no.99, pp.1-14. doi: 10.1109/TGRS.2017.2648885.

B. Bayer, A. Simoni, Bertello, L., Schmidt, D., (in review) "Using advanced InSAR techniques to monitor landslide deformations induced by tunneling in the Northern Apennines, Italy". *Engineering Geology*.

B. Bayer, A. Simoni, Mulas M., Corsini, A., Schmidt, D., (to be submitted) "Deformation responses of slow moving landslides to seasonal precipitation in the Northern Apennines, measured by InSAR." - To be submitted in *Geomorphology*

Il dott. Benedikt Bayer ha affrontato il lavoro affidato dando prova di autonomia, capacità di organizzazione e sviluppo del lavoro di ricerca; l'impegno dimostrato ha consentito di acquisire numerose conoscenze sia nel trattamento di grandi moli di dati tramite tecniche complesse che nello sviluppo di codici di elaborazione. Il Dott. Bayer ha sempre dimostrato passione per il lavoro di campo, per il lavoro di analisi e per l'interpretazione dei dati; ha dimostrato eccellenti competenze riguardo alla ricerca svolta; ha svolto il suo lavoro con costanti dedizione e impegno, dimostrando ottime doti applicative e capacità di analisi che hanno largamente superato le normali aspettative. Il candidato si è distinto per l'attitudine alla cooperazione con

B2



---

## Acknowledgements

Three years are a long time and many people helped me during the different stages of my work. It is most certainly impossible to thank all of them in and hence I will report here an, in all likelihood incomplete, list of acknowledgements in the hope that I did not miss anybody. First of all I would like to thank my advisor Alessandro Simoni, who helped me throughout the whole time, not getting lost in unimportant details and focus on the principal aspects of my work. His door was always open and I often came by (of course without warning) and asked for advise. I am also very grateful to David Schmidt, who hosted me for six months at the University of Washington. He helped me to understand the fundamentals of radar inteferometry. Without him the colourful images would look nice but yield no information.

I would like to thank my applied geology colleagues Lara Bertello, Silvia Franceschini, Martina Morandi and Gabriela Squarzoni for nice discussions, field work including encounters with dogs, dog owners, evil goats and wild boars. I thank also Silvia Katò, Maria Filippini, Bruno Campo, Luigi Bruno and everybody from the third floor for the nice company at Bologna, excellent lunches, dinners, coffee breaks and sunny moments on the department's terrace.

The discussions with Alexander Handwerker helped a lot to improve my understanding of InSAR processing strategies for landslide applications. I am glad that I visited him at the University of Oregon, where he introduced me to local beer, burgers and milestones in American college culture. Also the discussions with Xiaopeng Tong and Marc Welsh helped me to learn a lot about InSAR and especially Xiaopeng's enthusiam convinced me to try out GMTSAR.

I would also like to thank my co-authors Marco Mulas, Alessandro Corsini and Matteo Berti for fruitful discussions on various topics regarding landslides and geology. I really enjoyed working with them. I am also grateful for the comments of Janusz Wasowski and Veronica Tofani who made useful comments on an earlier draft of this dissertation. I think that they improved the present work significantly.

Finally but even more I thank my girlfriend Emanuela Bologna, my parents Ludwig and Andrea Bayer as well as my sister Hannah Bayer for great support throughout my studies.

---

# Contents

<b>1</b>	<b>Introduction</b>	<b>1</b>
1.1	Motivation and main focus of the Dissertation . . . . .	1
1.2	Geographical and geological background . . . . .	2
1.3	General guide through the thesis . . . . .	4
1.4	References . . . . .	6
<b>2</b>	<b>Methodological notes: Using StaMPS for the analysis of slow moving landslides</b>	<b>9</b>
2.1	State of the art and general aspects of the processing workflow . . . . .	9
2.2	InSAR datasets and sensitivity analysis of processing parameters . . . . .	11
2.3	Radar interferometry measures relative displacements . . . . .	14
2.4	Influence of processing parameters during pixel selection . . . . .	18
2.4.1	Variability on the regional scale . . . . .	18
2.4.2	Pixel selection on a local landslide case . . . . .	19
2.5	Main parameters that influence unwrapping . . . . .	22
2.5.1	Variations on the regional scale . . . . .	22
2.5.2	Calibrating the interferometric signal for a single landslide cases . . . . .	24
2.6	Strategical notes and concluding discussion . . . . .	26
2.7	References . . . . .	28
<b>3</b>	<b>Influence of digital elevation models on InSAR results</b>	<b>32</b>
3.1	Introduction . . . . .	34
3.2	Materials and Methods . . . . .	36
3.2.1	Satellite datasets and InSAR processing . . . . .	36
3.2.2	The External Elevation data . . . . .	38
3.2.3	Sensitivity analysis . . . . .	39
3.2.4	Theoretical and statistical evaluation of the DEM influence on InSAR processing . . . . .	40
3.3	Impact of the external digital elevation models on InSAR-results . . . . .	43
3.3.1	DEM comparison in geographic coordinates . . . . .	43
3.3.2	DEM comparison in radar-coordinates . . . . .	45
3.3.3	Comparison of stacked interferograms . . . . .	47
3.4	Qualitative analysis of the PS- and SB-results . . . . .	48
3.4.1	Differences on a regional scale . . . . .	48
3.4.2	The Carbona landslide: An example of local differences for Envisat . . . . .	50
3.4.3	Lama Mocogno: An example of local differences in SB-results with Cosmo-SkyMed . . . . .	52
3.5	Discussion and concluding remarks . . . . .	56

---

3.6	Time series analysis of Carbona and Lama Mocogno . . . . .	59
3.7	References . . . . .	61
<b>4</b>	<b>Deformations induced by tunneling under deep-seated landslides</b>	<b>67</b>
4.1	Introduction . . . . .	69
4.2	Materials and Methods . . . . .	72
4.2.1	InSAR processing . . . . .	72
4.2.2	Monitoring data . . . . .	73
4.2.3	Field survey and geophysical investigation . . . . .	74
4.3	Geological description of the slope . . . . .	74
4.3.1	Geological and geomechanical background . . . . .	74
4.3.2	Geomorphology and landsliding . . . . .	77
4.4	Kinematic behaviour of the landslide complexes . . . . .	81
4.4.1	InSAR derived displacement maps . . . . .	81
4.4.2	Deformation history at Santa Maria Maddalena . . . . .	83
4.4.3	Spatial and temporal development of the displacements . . . . .	85
4.5	Discussion and concluding remarks . . . . .	89
4.6	References . . . . .	94
<b>5</b>	<b>Deformation responses of landslides to seasonal precipitation</b>	<b>101</b>
5.1	Introduction . . . . .	105
5.2	Geological and geographical background . . . . .	106
5.3	Materials and Methods . . . . .	107
5.3.1	InSAR processing details . . . . .	107
5.3.2	Combining interferograms from different orbits . . . . .	110
5.4	InSAR results at the catchment scale . . . . .	111
5.4.1	Morphology of InSAR-detectable landslides . . . . .	111
5.4.2	Differences in spatial displacement patterns . . . . .	114
5.5	Kinematics of selected landslides . . . . .	116
5.5.1	Local variations of different landslide types . . . . .	117
5.5.2	Deformation responses to long enduring rainfall events . . . . .	118
5.5.3	Relationship between deformation response and precipitation . . . . .	121
5.6	Discussion . . . . .	124
5.7	Conclusions . . . . .	126
5.8	References . . . . .	126
<b>6</b>	<b>Discussion and General conclusions</b>	<b>134</b>

## Abstract

The present work addresses different aspects of the analysis of landslide motion in the Northern Apennines of Italy by means of spaceborn radar interferometry (InSAR). Datasets from the satellite systems Envisat, COSMO SkyMed and Sentinel 1A were processed with different open source packages and exploited in order to investigate technical issues related to different InSAR processing techniques and to obtain precise deformation measurements.

One particular technical issue was the influence of the external digital elevation model, that is used to calculate and subtract the topographic phase, on final PS-InSAR and SBAS-results (chapter 3). It is common that different digital elevation models are available for a study area and often differences in final PS-InSAR/SBAS results can be observed. An experiment was designed that involved the InSAR processing with data from COSMO SkyMed and Envisat with different external digital elevation models. A Monte Carlo approach was used to test the theoretical impact on the InSAR datasets and the observed differences were described and statistically evaluated. Although the evaluation of DEM quality is complicated, low quality digital elevation models caused a clear decrease in the number of selected pixels. Differences in the deformation fields, obtained for different digital elevation models are related to pixel selection and problems during unwrapping. Two local case studies showed that an accurate digital elevation model can improve the interferometric signal.

Due to the high landslide density in Northern Apennines, slope instabilities often interfere with man made structures. The case of Ripoli and Santa Maria Maddalena, which are two small villages located in the Reno river catchment South of Bologna, show in a particularly interesting way this interaction between human activity and landslide deformation (chapter 4). Here, a double road tunnel was excavated under a slope that hosts several old deep seated landslides. The tunnel is part of the highway project "variante di valico" and connects Bologna with Florence. Soon after excavation started in 2011 first deformations and also damages on a number of buildings were registered. InSAR datasets derived from Envisat, COSMO SkyMed and Sentinel 1A show the slopes in relatively stable conditions before excavation started, document the landslide acceleration during the construction phase and show a decrease in displacement rates after the construction ceased. The InSAR

derived spatio-temporal deformations were used together with GPS, seismic ambient noise and inclinometer measurements to develop a detailed geotechnical model of the slope. Displacement time series from the inclinometers confirm the InSAR measurements. A comparison between displacement rates, tunnel position, excavation rate and precipitation suggests that the down-slope oriented displacements are caused by the excavation and that the hydrological regime had only a minor impact on the observed deformations.

Although human interaction maybe the cause of landslide deformation, precipitation is typically the main driving agent of landslide displacement and slope failure. During the years 2013 and 2014 Northern Italy was struck by long enduring persistent rainfalls that caused numerous landslide reactivations. Radar interferometry provides the possibility to measure the deformation responses of slow moving landslides to climatic forcing on a regional scale. InSAR datasets that span the period between 2011 and 2016 were used to assess kinematics of 25 landslides during the years 2013 and 2015, hosted either by chaotic clay shales or pelitic turbidites (chapter 5). Deformation responses to precipitation were analysed in detail for eight selected cases, four of which are located in pelitic turbidites and four that are hosted by chaotic clay shales. These cases can be considered representative examples for these lithologies and were chosen in part due to their morphological characteristics and in part due to their position in the study area. The InSAR derived displacements show that landslides in pelitic flysch formations accelerated abruptly and reached peak displacement rates approximately 30 days after the onset of the persistent precipitations of 2013 and 2015. On the contrary earthflows in chaotic clay shales reached lower displacement rates and the deformation response was smoother in time. This different behaviour is in all likelihood caused by different hydrological properties of the landslide materials. While landslide material in chaotic clay shales has a low permeability and the groundwater table is close to the ground surface throughout the year, enduring rainfalls are necessary to saturate the landslide bodies in the pelitic flysch formations and trigger a deformation response.

# 1 Introduction

## 1.1 Motivation and main focus of the Dissertation

In the present document, I present the main findings of my PhD project at the University of Bologna. The work concentrates on the analysis of slow moving landslides in the Northern Apennines of Italy. I used a remote sensing technique, termed space-born radar interferometry (InSAR in the following) to infer spatial and temporal displacement patterns of naturally deforming slopes as well as man-induced landslides. Due to the large areal extend of mechanically weak rocks, like tectonic and sedimentary melanges (PINI, 1999) and turbidites (RICCI LUCCHI, 1986), earthflows and complex landslides are prominent features of the Northern Apennine landscape (BERTOLINI et al., 2004; BERTOLINI et al., 2005; BORGATTI et al., 2006; SIMONI et al., 2013). Because the study area has also a moderate population density, landslides also often interfere with human action and cause periodically economic loss.

InSAR presents a promising technique that helped to address several major questions that developed before and during this dissertation. What are the main reason for landslide motion? What is the temporal displacement response to precipitation or anthropogenic activities of selected landslides? Do landslides respond to seasonal precipitation and single rainfall events? What are the major limitations of the technique and which drawbacks need to be considered during the interpretation of InSAR derived deformation? The present work was inspired by promising results that were reported by HANDWERGER et al. (2013) in a Northern Californian river catchment. In particular the fact that strong non linear displacement patterns in time were resolved on earthflows in lithologically similar conditions to those of the Northern Apennines was appealing.

All software packages that were used for InSAR processing are available in the public domain and are free for scientific purposes. The main program for InSAR

processing was the Stanford Method of persistent scatterers (StaMPS in the following, HOOPER et al., 2007; HOOPER, 2008), which uses the InSAR packages DORIS (KAMPES & USAI, 1999) and ROI-PAC (ROSEN et al., 2004) for interferometric processing. The reported results are fruit of efficient collaborations with various co authors. We addressed technical questions related to uncertainties in the interferometric signal, as well as scientific question that concern the spatial and temporal deformation patterns of different landslide types. Among the most important technical issues was the sensitivity of selected InSAR datasets to errors in the digital elevation model that is used to calculate and subtract the topographic phase. We also had the possibility to compare our InSAR derived displacements to inclinometer measurements, which gave interesting insights regarding the accuracy of our InSAR results. We investigated landslide motion that was induced by the excavation of a tunnel, but also deformation responses to seasonal precipitation on the catchment scale. In the first case we focussed on the displacement rate in relation to the tunnel position and the comparison between InSAR derived displacements and conventional monitoring results. In the second case we were interested in the kinematic behaviour of different landslide types hosted by different lithologies.

## 1.2 Geographical and geological background

The study area is located in the Northern Apennines of Italy and extends over the catchments of the Reno, Panaro and Secchia rivers South of Modena and Bologna (Fig. 1.1). It spans a total area of 3500 km<sup>2</sup> and topographic heights range from approximately 50 m at the foothills in the North to maximum 2165 m at the crest of Monte Cimone. The Northern Apennines are a fold and thrust belt that formed due to the collision of the Adriatic and the European plate (e.g. BOCCALETTI et al., 1971). The surrection of the Apennine chain occurred in three phases during the Tortonian, the Messinian and the Plio-Pleistocene (RICCI LUCCHI, 1986). The uplift over the sea level occurred during the Middle and Upper Pleistocene (BARTOLINI, 2003). CYR & GRANGER (2008) inferred erosion rates of 0.28 to 0.58 mm/year were from cosmogenic nucleid data and suggested a dynamic equilibrium between uplift and erosion. The estimated erosion rate are in line with estimates of earth flow sediment yield in the (SIMONI et al., 2013).

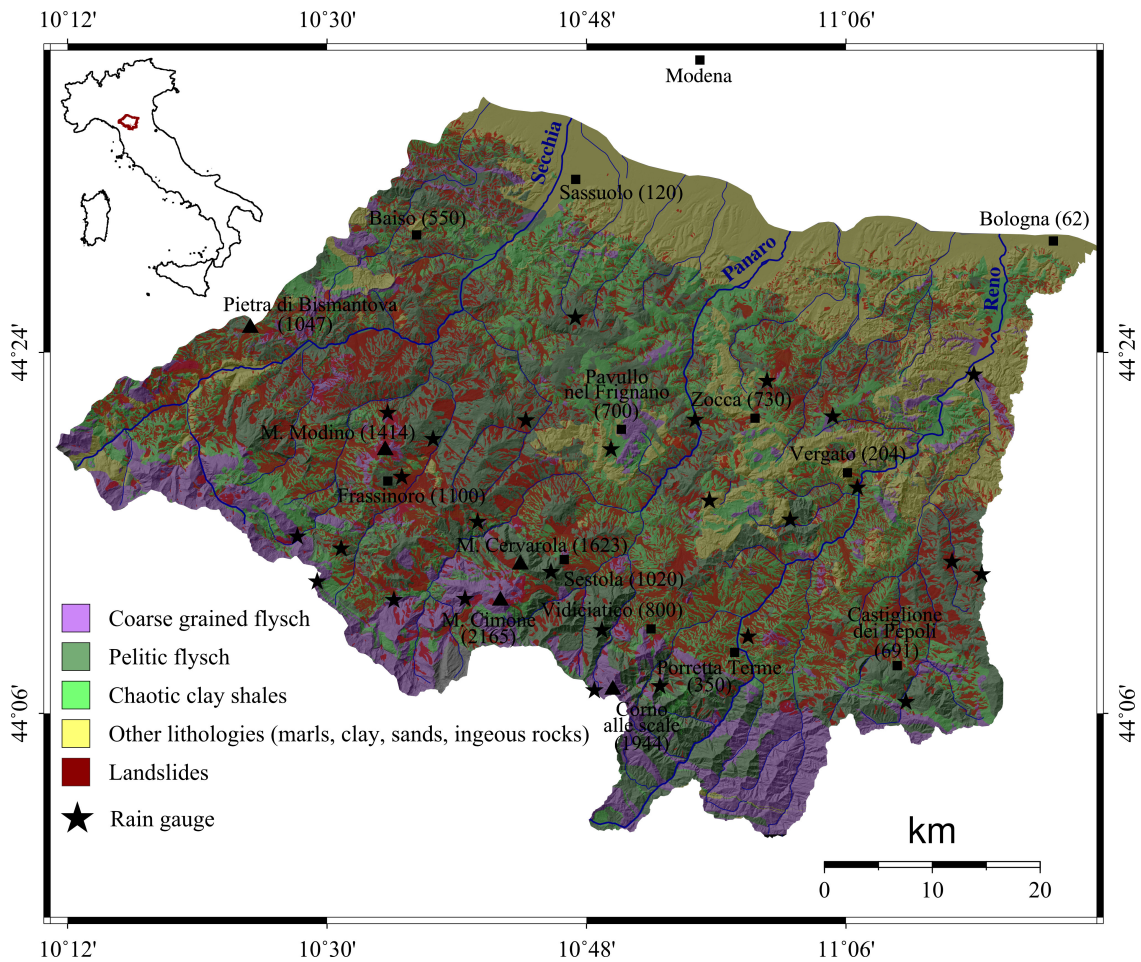


**Figure 1.1:** The simplified lithological map of the study area was compiled from a digital version of the regional geological Map (BERTI & GENERALI, 2000) and the regional inventory SERVIZIO GEOLOGICO, SISMICO E DEI SUOLI DELLA REGIONE EMILIA-ROMAGNA, 2014

In the study area, tectonically sheared Flysch with a major pelitic component (dark green colours in Fig. 1.1) and chaotic clay shales with typical block in matrix fabric are the most common lithologies (dark green colours in Fig. 1.1). In the study area, both pelitic Flysch and chaotic clay shales form the substrate of large parts of the slopes. They also host the major part of the landslides in terms of total area (Fig. reffig.litorelation a), but also in terms of landslide density (Fig. reffig.litorelation b). Although these lithologies can occur in many structural and stratigraphical formation of the Northern Apennines, here, they correspond to the heavily sheared Flysch rocks of the Ligurian Monghidoro and Monte Venere formations (MAXWELL, 1959; RICCI LUCCHI, 1986; PINI, 1999). The most common

melanges type rocks are the Palombini shales as well as the Varicoloured and Variegated shales (PINI, 1999; BETTELLI & VANNUCCHI, 2003). Also other lithologies like the coarser turbidite formations of the Tuscan units (purple colours in Fig. 1.1) or the marls and sandstones of the Epi-Ligurian formations (summarized together with other formations yellow colours in Fig. 1.1) occur frequently. They host however few landslides both in terms of total area as well as in terms of landslide density (Fig. 1.2 a and b).

The mediterranean climate in the study area is characterized by two peaks in hydrological year (PAVAN et al., 2008), one of which occurs in late winter to early spring, while the second one occurs in autumn (see also Fig. 1.2c). Winters are moderately humid, although a decrease in winter precipitation was observed since the 1960s (TOMOZEIU et al., 2002). Summers are generally dry, but intense thunderstorms may occur. This precipitation regime explains why the landslides in the study area undergo both seasonal accelerations, but also why catastrophic reactivations occur with respect to rainfall events during the rain seasons (BERTI et al., 2012).

### 1.3 General guide through the thesis

This document has six main chapters, the first one of which serves as a general introduction. Chapters three, four and five are articles that were submitted to peer review journals and can be considered on the one hand as independent works. On the other hand they should be seen in the framework of the general motivation of this dissertation. The second chapter is dedicated to a few general methodological aspects of my work. It contains information that due to the focus of the journals could not be included in one of the articles, yet might be helpful for other scientists or students that want to use one of the described packages for InSAR processing.

The third chapter is dedicated to a technical problem that emerged in the early stages of my PhD. InSAR requires as external digital elevation model to forward model and subtract the phase term that is caused by the topography. Generally SRTM is used for this purpose. However, in our study area several digital elevation models are available that can differ considerably on the local scale. We observed that final InSAR results vary if different DEMs are used during InSAR processing. In literature this problem is rarely described and was never addressed in detail,

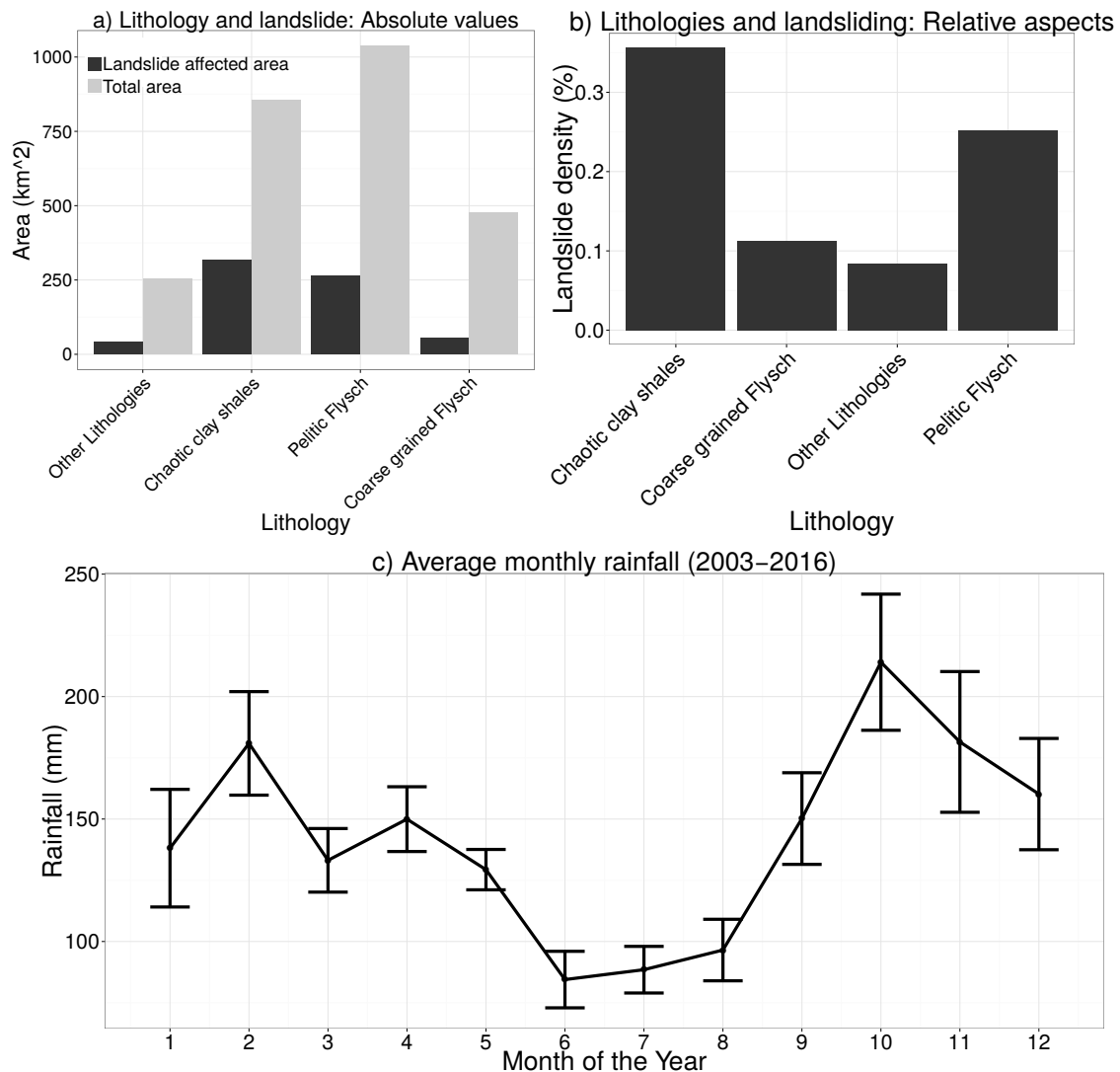


**Figure 1.2:** a) Absolute area for a given lithology in the study area the portion of the lithology that is affected by landsliding. b) Landslide density for the different lithologies. c) Average monthly rainfall for all raingauges in the study area (stars in Fig. 1.1)

although different theoretical strategies for DEM error estimation were proposed. We developed an experimental framework to evaluate the sensitivity of two InSAR datasets to the quality of the DEM.

The fourth chapter treats in detail a local landslide study that is located ca. 40 km South of Bologna in the localities Santa Maria Maddalena and Ripoli. Here, the excavation of a double road tunnel at relatively shallow depths caused the deformation several deep seated landslides. The case was chosen due to the high quality

of the InSAR signal and because detailed external monitoring data was available for a comparison with our InSAR results. This gave us the possibility to evaluate eventual uncertainties of our InSAR results and the processing tools in our study area. Another important aspect that led to the selection of this case was the fact that here rainfall is not the main reason for the deformation but the excavation of the tunnel. Hence it provided a case that shows different displacements in time than the cases that are treated in chapter five.

In the fifth chapter slope displacements are addressed on the catchment scale by means of radar interferometry. We processed data from Cosmo SkyMed and Sentinel 1A and compared the morphological characteristics of the landslides that yielded signals in our InSAR datasets. Moreover, we obtained detailed time series products covering the years 2013 and 2015 for eight representative landslides. It was possible to measure non linear deformation responses with respect to seasonal precipitation. We also measured different displacement styles for two different landslide types.

## 1.4 References

- BARTOLINI, C. (2003): When did the Northern Apennine become a mountain chain? – *Quaternary International*, **101-102** (1), pp. 75–80; United Kingdom.
- BERTI, M. & GENERALI, M. (2000): Carta litologica dell’Emilia-Romagna (modificata dalla carta geologica). – ed. by REGIONE EMILIA-ROMAGNA. SERVIZIO GEOLOGICO, SISMICO DEI SUOLI versione digitale non pubblicata; <http://www.regione.emilia-romagna.it/> (Regione Emilia Romagna).
- BERTI, M., MARTINA, M. L. V., FRANCESCHINI, S., PIGNONE, S., SIMONI, A. & PIZZIOLO, M. (2012): Probabilistic rainfall thresholds for landslide occurrence using a Bayesian approach. – *Journal of Geophysical Research-earth Surface*, **117** (), F04006;
- BERTOLINI, G., CASAGLI, N., ERMINI, L. & MALAGUTI, C. (2004): Radiocarbon data on lateglacial and Holocene landslides in the Northern Apennines. – *Natural Hazards*, **31** (3), European Geophys Soc;

- BERTOLINI, G., GUIDA, M. & PIZZIOLLO, M. (2005): Landslides in Emilia-Romagna region (Italy); strategies for hazard assessment and risk management. – *Landslides*, **2** (4), pp. 302–312; Heidelberg.
- BETTELLI, G. & VANNUCCHI, P. (2003): Structural style of the offscraped Ligurian oceanic sequences of the Northern Apennines; new hypothesis concerning the development of melange block-in-matrix fabric. – *Journal of Structural Geology*, **25** (3), pp. 371–388; Oxford.
- BOCCALETTI, M., ELTER, P. & GUAZZONE, G. (1971): Plate Tectonic Models for the Development of the Western Alps and Northern Apennines. – *Nature*, **234** (49), pp. 108–111; Oxford.
- BORGATTI, L., CORSINI, A., BARBIERI, M., SARTINI, G., TRUFFELLI, G., CAPUTO, G. & PUGLISI, C. (2006): Large reactivated landslides in weak rock masses; a case study from the Northern Apennines (Italy). – *Landslides*, **3** (2), pp. 115–124; Berlin, New York etc.
- CYR, A. J. & GRANGER, D. E. (2008): Dynamic equilibrium among erosion, river incision, and coastal uplift in the northern and central Apennines, Italy. – *Geology*, **36** (2), pp. 103–106;
- HANDWERGER, A. L., ROERING, J. J. & SCHMIDT, D. A. (2013): Controls on the seasonal deformation of slow-moving landslides. – *Earth and Planetary Science Letters*, **377–378** (1), pp. 239–247; Amsterdam.
- HOOPER, A., SEGALL, P. & ZEBKER, H. (2007): Persistent scatterer interferometric synthetic aperture radar for crustal deformation analysis, with application to Volcan Alcedo, Galapagos. – *Journal of Geophysical Research-solid Earth*, **112** (B7), B07407; Washington DC.
- HOOPER, A. (2008): A multi-temporal InSAR method incorporating both persistent scatterer and small baseline approaches. – *Geophysical Research Letters*, **35** (16), p. L16302; Washington DC.
- KAMPES, B. & USAI, S. (1999): “Doris: The delft object-oriented radar interferometric software” In: 2nd International Symposium on Operationalization of Remote Sensing, Enschede, The Netherlands vol. 16 Citeseer, 1999, p. 20.

- MAXWELL, J. C. (1959): Orogeny, gravity tectonics, and turbidites in the Monghidoro area, northern Apennine mountains, Italy. – Transactions of the New York Academy of Sciences, **21** (4), pp. 269–280;
- PAVAN, V., TOMOZEIU, R., CACCIAMANI, C. & DI LORENZO, M. (2008): Daily precipitation observations over Emilia-Romagna: mean values and extremes. – International Journal of Climatology, **28** (15), pp. 2065–2079;
- PINI, G. A. (1999): Tectonosomes and olistostromes in the argille scagliose of the Northern Apennines, Italy. – Special Paper - Geological Society of America, **335** (1), pp. 1–70; Boulder.
- RICCI LUCCHI, F. (1986): The Oligocene to Recent foreland basins of the Northern Apennines. – In: A., P. & HOMEWOOD, P. [eds.] (1986): Special Publication of the International Association of Sedimentologists, pp. 105–139; Oxford (Blackwell).
- ROSEN, P. A., HENSLEY, S., PELTZER, G. & SIMONS, M. (2004): Updated repeat orbit interferometry package released. – Eos Trans. AGU, **85** (5), pp. 47–47; Malden.
- SERVIZIO GEOLOGICO, SISMICO E DEI SUOLI DELLA REGIONE EMILIA-ROMAGNA (2014): Carta Inventario delle frane a scala 1:10000 della Regione Emilia-Romagna. URL: <http://ambiente.regione.emilia-romagna.it/geologia/cartografia/webgis-banchedati/cartografia-dissesto-idrogeologico>; –.
- SIMONI, A., PONZA, A., PICOTTI, V., BERTI, M. & DINELLI, E. (2013): Earth-flow sediment production and Holocene sediment record in a large Apennine catchment. – Geomorphology, **188** (1), pp. 42–53; Amsterdam.
- TOMOZEIU, R., LAZZERI, M. & CACCIAMANI, C. (2002): Precipitation fluctuations during the winter season from 1960 to 1995 over Emilia-Romagna, Italy. – Theoretical and Applied Climatology, **72** (3-4), pp. 221–229;

# **2 Methodological notes: Using StaMPS for the analysis of slow moving landslides**

## **2.1 State of the art and general aspects of the processing workflow**

After the launch of the first ERS satellite in the early nineties, InSAR became a valuable tool for the measurement of deformation fields (MASSONNET & FEIGL, 1998; HANSEN, 2001; BÜRGMANN et al., 2000). Although generic interferometry can yield high quality results for landslides, if imagery from L-band satellites is used (ROERING et al., 2005; STROZZI et al., 2005), in our study area interferograms from satellites with shorter wavelengths are often disturbed by decorrelation and atmospheric noise (CORSINI et al., 2006). Advanced processing schemes like Persistent scatterers (FERRETTI et al., 1999; FERRETTI et al., 2001) or Small Baseline approaches (BERARDINO et al., 2002; SCHMIDT & BÜRGMANN, 2003) were developed to derive deformation time series and address some of the problems due to decorrelation. In the last decade these two techniques were used by different groups to successfully derive landslide deformation in space and time (HILLEY et al., 2004; FARINA et al., 2006; GUZZETTI et al., 2009; LAUKNES et al., 2010; BOVENGA et al., 2012; HANDWERGER et al., 2013; WASOWSKI & BOVENGA, 2014). Still, decorrelation remains a problem in the less urbanized parts of the Northern Apennines (POGGI & RICELLI, 2011). Focussing on the investigation of volcanic processes, the Stanford Method of Persistent scatterers was developed with improvement of interferometric results in rural areas in mind (HOOPER et al., 2004; HOOPER et al., 2007).



selected, the results from the single patches are merged and the sparse interferograms can be multilooked in order to reduce noise at the cost of spatial resolution. The interferograms can be unwrapped either in two dimensions (CHEN & ZEBKER, 2001) or in addition the time domain can be considered (HOOPER & ZEBKER, 2007). When successfully unwrapped, the interferograms are inverted with respect to the common master date in order to solve for incremental range change in each time step. In two final steps the spatially correlated look angle error and the spatially correlated noise, which includes part of the atmospheric contribution, are estimated.

Although a software manual of the program exists [*pdf-01*], a detailed guide on how to use StaMPS for the analysis of slow moving landslides is missing. Given the high number of processing parameters that can be modified in order to improve the final products, it is difficult for people who are new to the field, to adjust the processing chain for the specific needs. The interferometric signal that is caused by slow moving landslides is reduced in space compared to large scale deformation fields like those caused by tectonic creep, earthquakes or urban subsidence. Also landslide kinematics may vary in space on a single landslide, causing steep phase ramps and decorrelation. Even though single landslides are small scale features, they model whole landscapes, where mechanically weak rocks form the substrate. Hence works that seek to analyse landslide processes can have both regional and local problems that need to be addressed. Here, we do not aim to report an exhaustive description of all processing parameters that can be adjusted in StaMPS, still we would like to illustrate the effect of selected processing parameters and concepts that had a high influence on the final interferometric result.

## 2.2 InSAR datasets and sensitivity analysis of processing parameters

In this PhD thesis, data from different satellites were processed in order to derive deformation maps and time series products. The works use data from Envisat (chapter 3 to 4), Cosmo SkyMed (chapter 3 to 5) and Sentinel (chapter 4 and 5).

Here, we will illustrate the sensitivity of the final interferometric product obtained by the Small Baseline module of StaMPS to selected processing parameters. The experiments are carried out for one ascending Cosmo SkyMed dataset (Fig. 2.2), but

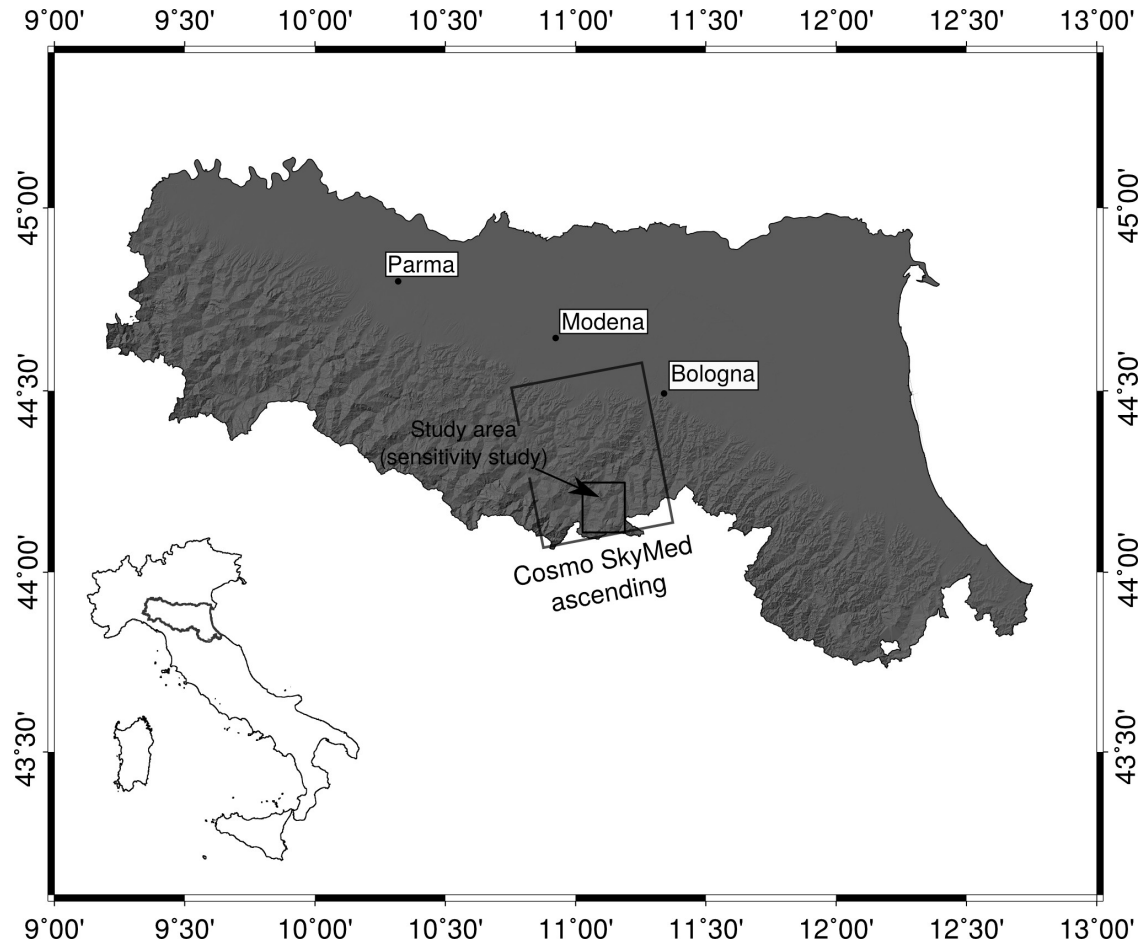


**Figure 2.2:** Location of the reduced study area that was included in the sensitivity study. We used 38 SAR scenes from an ascending Cosmo SkyMed swath to form 60 interferograms.

the herein described effects are valid also for all other datasets that were used in this dissertation. We chose to focus on the small baseline module because in our study area the results are less affected by noise. Generally more pixels are selected, time series contain less high frequency scatter and also the spatial signal was clearer compared to the PS results. AGRAM (2010, p. 105 ff.) and LAUKNES et al. (2010) found that the Small Baseline method selected a higher density of pixels in rural terrain with little vegetation of a Norwegian rockslide. They suggested that the better performance of the Small baseline approach is due to the scattering characteristics of the terrain in these areas. SBAS selects pixels that are dominated by multiple scatterers (distributed scatterers concept), while PS approaches select pixels that are dominated by a single dominant scatterer (persistent scatterer concept). HOOPER

(2008) showed that both strategies select different pixels that can be combined in order to optimize the results. We believe that in our study area the SB-module selects a higher number of pixels because, SB-datasets contain interferograms that are less decorrelated and hence less pixels are rejected. Compared to the PS-InSAR approach a higher number of interferograms is used to solve for incremental range change in single, which makes the inversion more stable and less affected by high frequency noise. On the downside it requires more memory, longer processing times and a small amount of information might be lost because real persistent scatterers maybe rejected.

We systematically tested processing parameters for pixel selection and unwrapping from an ascending Cosmo SkyMed dataset on a reduced part of the Reno river catchment. We chose the case of Camugnano to illustrate the effects of these parameters on the scale of a single landslide. Although we tested more parameters we will focus only on parameters during pixel selection and unwrapping, because they had in our view the highest impact on the final solution.

**Pixel selection:** Pixel selection is carried out in 3 steps that involve the estimation of coherence, pixel selection and pixel weeding. In total 10 parameters can be used to govern the processing. We will focus however only on two main parameters during the pixel selection and pixel weeding. It is possible to admit a certain amount of noisy pixels in the selection routine, which can be defined in terms of a density (parameter `density_rand`, noisy pixels/ $km^2$ ). After the selection, a standard deviation for weeding (`weed_standard_dev`) can be defined to reject pixels. We tested random densities between 1 and 80 noisy pixels per  $km^2$  and standard deviations between 0.5 and 1.4 for Cosmo SkyMed.

**Unwrapping:** StaMPS offers two main unwrapping methods, the first one of which unwraps only in two dimensions, while the second strategy considers also the time domain to guide the unwrapping. Again many parameters can be modified and some of them have a strong impact while others do not seem to affect the final solution. In this chapter we will limit ourselves to discuss the differences between the 2D and 3D approach as well as between various grid sizes (parameter `unwrap_grid_size`) in combination with different time windows (parameter `unwrap_time_win`) for regional and local scale applications. We

tested systematically grid sizes between 25 and 250 meters and time windows between 30 and 365 days.

## 2.3 Radar interferometry measures relative displacements

Before going into details of pixel selection and unwrapping, we would like to illustrate a key concept of InSAR that had particular impact on the results that were obtained over our study area. Radar interferometry measures relative displacements with respect to a stable reference area. In StaMPS the reference area can be defined with the parameters `ref_centre_lonlat`, which is the central point of the reference area, and `ref_radius`, which defines a radius around this central point. Both mean velocities and cumulative displacements of the final results are calibrated with respect to the average phase of the pixels inside this radius. If no pixels falls inside the defined region, the mean of all pixels is subtracted in order to eliminate signal that is present in all scenes.

The interferometric phase contains besides the differential phase due to displacements also nuisance terms (HANSSEN, 2001; AGRAM & SIMONS, 2015) that, together with unwrapping errors, often obscure the spatial signal in areas at a certain distance from the stable reference pixels. In order to evaluate the effect of this problem we chose different reference areas (Fig.2.3) and inspected the deformation maps. Positive values and red colors are range increases and relative movement away from the satellite, while blue values are range decreases and relative movements towards the satellite. The first reference area was set with respect to a non deforming region on houses at Maranino (Fig. 2.3 a). The reference area is also located at a relative distance of more than 10 km with respect to the landslides of Camugnano (Fig. 2.3 b), Bargi and Badi di Suviana (Fig. 2.3 c) and Creda (Fig. 2.3 d).

The absolute signal at Camugnano is not well visible, when the reference area is set to Maranino, while absolute displacements are overestimated, when the reference area is chosen with respect to Suviana or Creda. Absolute mean velocities become sharper in space and numerically more reasonable when the reference area was set as close as possible to Camugnano. The relative signal in the deformation maps appear identical in all cases. On the contrary, the deformation signal of Bargi di Suviana is

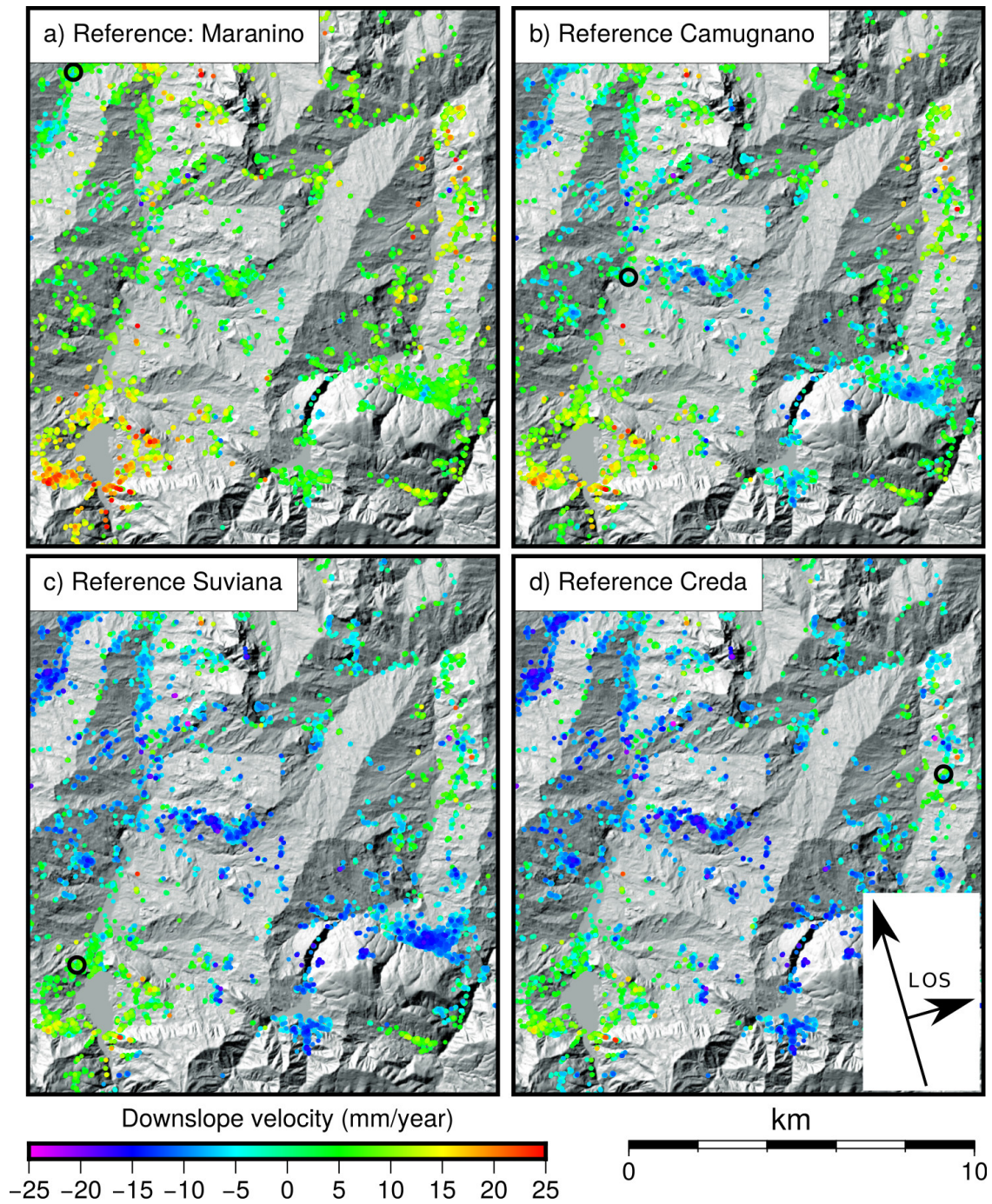


**Figure 2.3:** Deformation maps for different stable reference areas at a) Maranino b) Camugnano c) Bargi di Suviana and d) Creda. Maranino was chosen because it is located at distance from the landslides in b-d and it should be stable. Positive values and red colours are range increases (movement away from the satellite), while negative values and blue colours are range decreases and hence movement towards the satellite.

overestimated, when the reference area is set to Camugnano. We believe that this effect is due to the different atmospheric conditions over Suviana and Caugnano. Since this difference is present also in datasets from other satellites, it is possible that the lake of Suviana might contribute to these different conditions. In analogy to the signal at Camugnano, the absolute signal at Creda is clear when the reference area is set to Creda or Suviana and is not well visible with the reference area close to Camugnano.

The variations due to different reference areas are best illustrated when looking at a single landslide case like Camugnano with the reference area in vicinity to the landslide (Fig.2.4 a) and at distance (Fig.2.4 b). The relative displacement signal is in both cases the same, only the absolute values differ. This problem affects also the time series. The landslide of Camugnano suffered a strong acceleration during the Spring of 2013 that caused significant damage on infrastructure and houses. This acceleration is only evident, when the reference is set close to Camugnano (Fig. 2.4 c). With a reference area at greater distance (Fig. 2.4 c) it is masked by a steeper slope in combination with high frequency scatter.

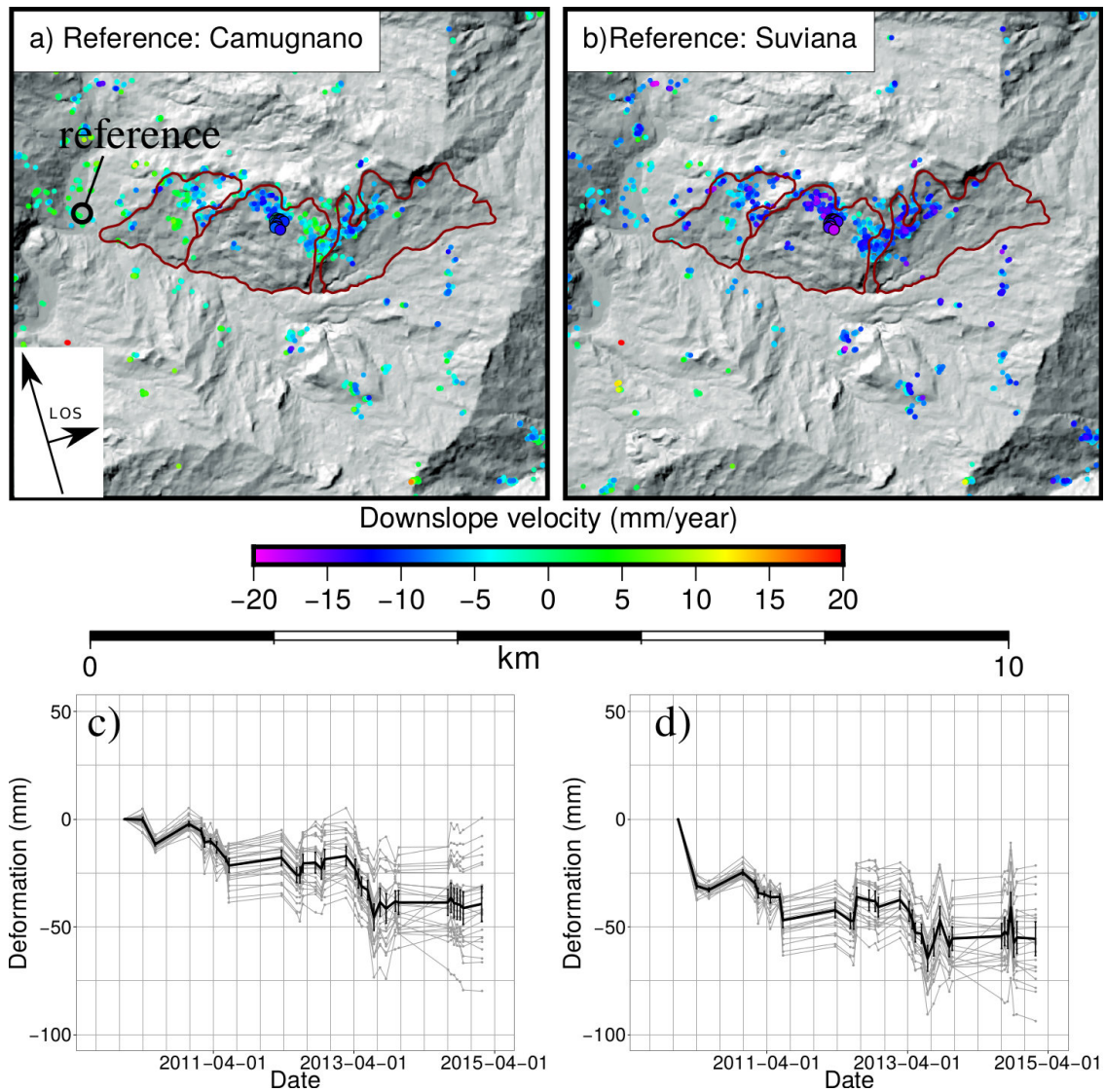


**Figure 2.4:** a) Deformation maps for Camugnano with the stable reference area close to the unstable slope, b) with the stable area at Suviana. c) Cumulative displacement in time when the reference area is selected close to Camugnano and d) when set to Suviana. An acceleration pattern during spring 2013 appears only clear when the reference area is located at Camugnano.

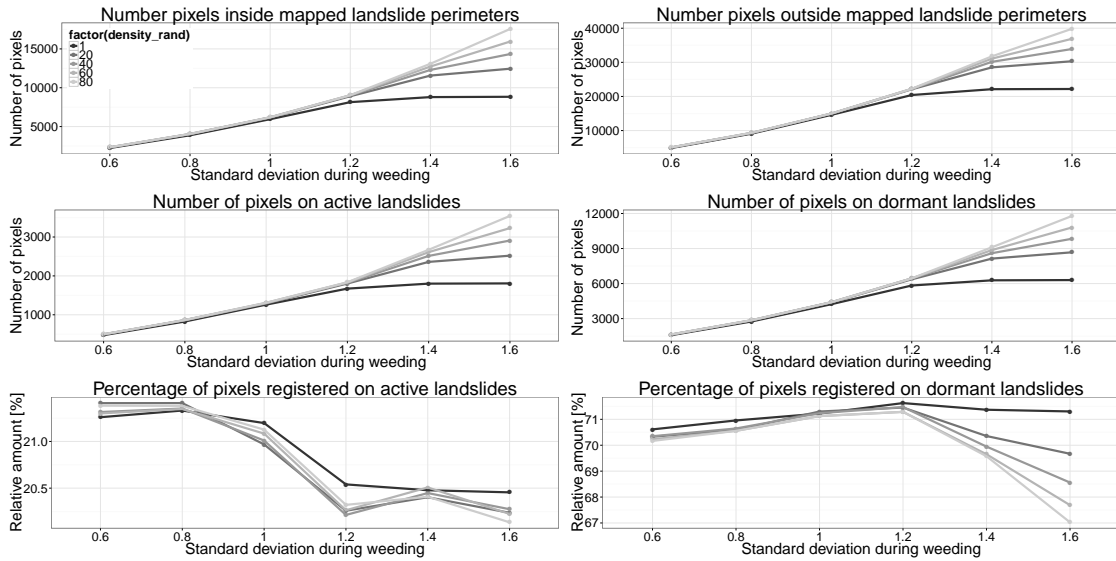


**Figure 2.5:** a) Number of pixels registered inside landslide mapped landslide perimeters for different densities of noisy pixels and standard deviations during weeding b) Number of registered pixels outside mapped landslide bodies. c) Number of pixels selected on active and d) on dormant landslides. e) relative amount of pixels selected on landslide bodies mapped as active and f) mapped as dormant. The relative amount is with respect to pixels that were selected inside landslides and not with respect to the overall number of pixels.

## 2.4 Influence of processing parameters during pixel selection

### 2.4.1 Variability on the regional scale

The pixel selection routines in StaMPS are time intensive, in particular when looking at larger areas. The pixel rejection (pixel weeding), is faster and systematic testing is less problematic for applications on the regional scale. The parameters that control pixel selection and rejection can be combined to work as a threshold. For high random densities also a high number of pixels are registered and with decreasing standard deviation during weeding, more pixels are rejected. Comparing the distributions of registered pixels inside and outside mapped landslide perimeters (Fig. 2.5 a and b), it appears that numerically less pixels are selected inside mapped landslide perimeters. However, the distribution of number of pixels in function of the two processing parameters is identical. For weeding standard deviations below 1, the number of selected pixels are comparable for any density of admitted noisy pixels. For example, given a standard deviation of 1.2, more pixels are selected if the

density of noisy pixels is more than 20. This difference occurs however for pixels that are located outside mapped landslides as well as for pixels inside mapped perimeters. Also, the relative distribution remains identical when looking for pixels located on active or dormant landslide bodies (Fig. 2.5 c-d). For all pixels that are located inside landslides, the relative percentage of pixels on active landslides is higher for high densities of noisy pixels in combination with low standard deviations during weeding (Fig. 2.5 e). On the contrary the relative contribution of pixels located on dormant landslide bodies becomes higher for all values of densities in combination with moderate standard deviations of weeding (Fig. 2.5 f).

Since the variation in relative contribution is only between 1.5 (Fig. 2.5 e) and 3 (Fig. 2.5 f) percent, we consider a statistical evaluation of the pixel selection regarding their position with respect to mapped landslides as problematic. Instead we believe that a visual inspection of the InSAR results for different processing parameters is necessary.

When looking at the mean velocity maps, it becomes clear that not only the number of pixels is influenced by the two tested parameters, but also the deformation signal becomes more or less evident if different thresholds are defined (Fig. 2.6). Large landslides like the case of Camugnano or Bargi di Suviana (see labels in Fig. 2.6 e) are visible in all solutions, although the spatial distribution and magnitude varied. In our view this has two main reasons. Either too many pixels are rejected and with them the pixels in those parts of that they have the highest displacement rates (Fig. 2.6 a-c). Or too many noisy pixels are selected, which damp the signal during unwrapping (Fig. 2.6 g). An efficient way to find a compromise between selecting pixels in areas of high displacement and not introduce too many noisy pixels is to start with high density of admitted noisy pixels and successively lower the standard deviation until the spatial signal is optimized. Densities of random pixels between 40 and 80 pixels/km<sup>2</sup> in combination with weeding parameters between 0.8 to 1.2 delivered in all cases reasonable results.

### **2.4.2 Pixel selection on a local landslide case**

In complicated topographic conditions and in areas where the spatial sampling of pixels is sparse, InSAR results can become very sensitive to processing parameters. Once landslide signals were identified, we cropped the InSAR results in space to fit

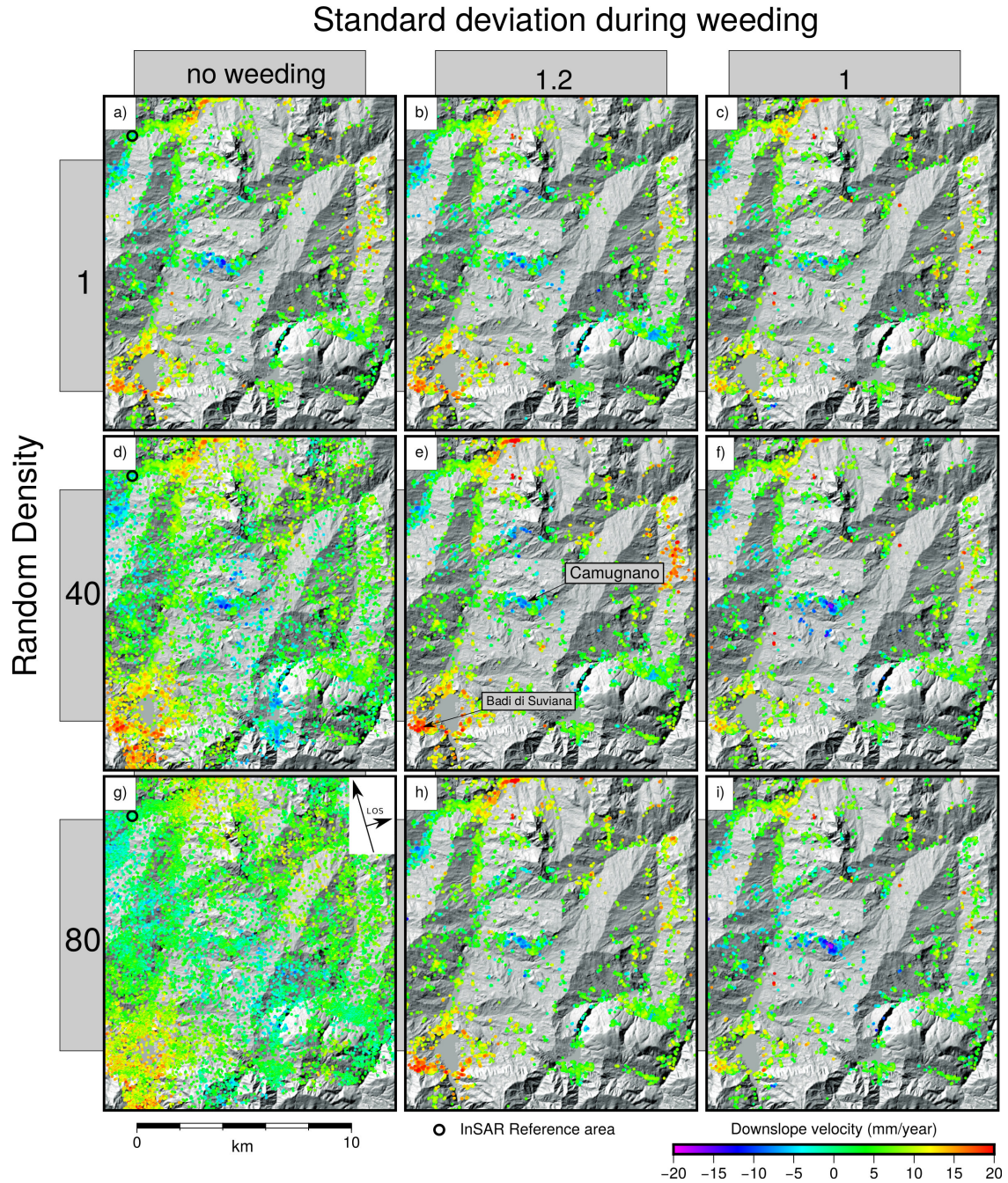


**Figure 2.6:** Mean velocities for different processing parameters a)-c) low density of admitted random pixels for three degrees of weed standard deviation. d)-f) Medium and g)-i) high density for variable weeding parameters. In the left column weeding has been skipped. The interferograms were corrected by the spatially correlated look angle error and orbital errors. Unwrapping was carried out in 2 dimensions in order to reduce processing time during the sensitivity experiments. The stable reference area is the same in all cases and located with respect to Maranino.

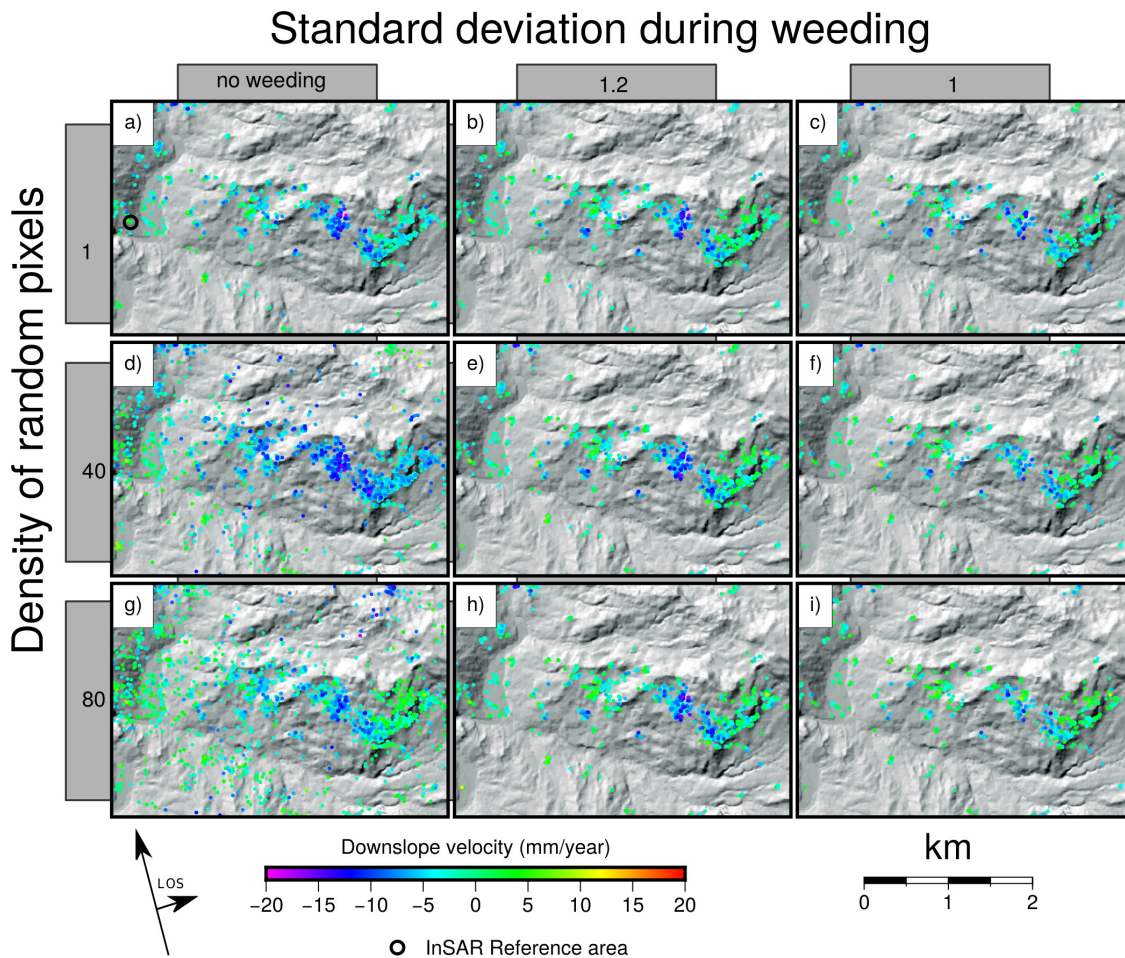


**Figure 2.7:** Local deformation maps at Camugnano for different parameters of pixel selection and rejection. Line of sight velocities were corrected by the spatially correlated look angle error and orbital ramps. Unwrapping was carried out with a grid size of 100 m and a time window of 60 days. First row: Low admitted density of noisy pixels if a) no pixel weeding was carried out, b) if a standard deviation of 1 and c) a standard deviation of 0.8 is used during weeding. Second row: Medium density of noisy pixels if d) no weeding was applied, e) a standard deviation of 1 and f) a standard deviation of 0.8 was used during weeding. Third row: High density of noisy pixels if g) no weeding is applied, h) a standard deviation of 1 or i) 0.8 was used during weeding window.

the landslide in question. This approach has several advantages: i) The effect of single processing parameters can be tested faster, because processing time is reduced. ii) Focussing on a single case makes the visualization easier. iii) Verification of a landslide signal is straight forward because single interferograms can be inspected faster.

In analogy to pixel selection on the regional scale, we varied densities of admitted random pixels and the standard deviation for pixel weeding. We also experimented with the exclusion of single noisy interferograms from pixel selection but found no improvement. Once a clear signal is obtained, it is important at this stage to assure that pixels are selected with respect to physical features on the ground. In our case, the pixels correspond typically to houses, hamlets or the concrete manufactured parts of the infrastructure. In our study area pixels are rarely chosen on agricultural terrain, even if large boulders are present.

When focussing on the landslide of Camugnano, a variation of pixel selection and rejection parameters causes a variation of the signal. For low densities and no weeding the moderate velocities were measured (Fig. 2.7 b-c), while lower standard deviations during weeding tend to eliminate the signal (Fig. 2.7 b-c). With a medium density of noisy pixels, high displacement rates are registered and pixels are selected with respect to the lower part of the landslide body (Fig. 2.7 d). In these zones houses or infrastructure is absent and the time series of the pixels contain high frequency scatter. Once weeding is applied (Fig. 2.7 e-f) the pixels are immediately rejected, which is why we do not believe it is worth keeping those pixels in the analysis. When a high density of noisy pixels is admitted (Fig. 2.7 g), the magnitude of the spatial deformation signal is reduced and the velocity maps contain a speckle like pattern in space. As soon as weeding is applied, the quality of the signal improves. The speckle pattern vanishes and also the magnitude of the velocity becomes comparable with the solutions obtained with medium densities in combination with different standard deviations during weeding.

## **2.5 Main parameters that influence unwrapping**

### **2.5.1 Variations on the regional scale**

Just as pixel selection and rejection, also the unwrapping routines can be cost intensive in terms of processing time. The two dimensional method runs fast compared to the three dimensional strategy (left column of Fig. 2.8). While large landslides like Camugnano appear again throughout all results, relative signals of smaller cases, like Lagora, are clear only with the three dimensional approach. On a regional scale, longer time windows take longer to unwrap, but may be capable of resolving a rela-

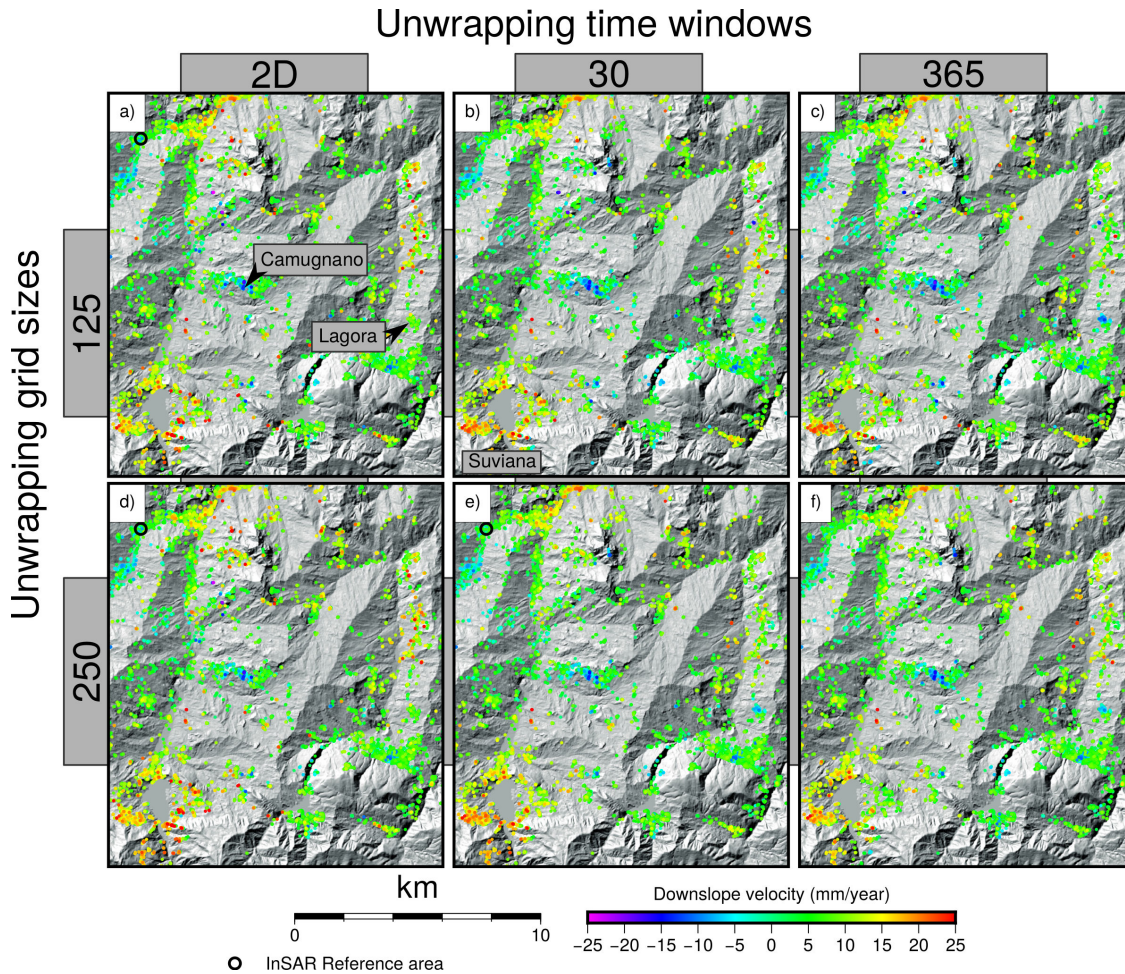


**Figure 2.8:** Regional deformation maps for different unwrapping parameters. First row: Small unwrap grid size (125 m) when a) unwrapping is carried out only in two dimensions, b) when also the time domain is taken into account with a time window of 30 days and c) 365 days. Second row: Large unwrap grid size with 250 m for d) unwrapping in 2 dimensions, e) 3D-unwrapping with 30 days and f) 365 days time window.

tive signal on landslides where no signal was visible before (see for example Lagora in Fig. 2.8 b and c). Small unwrapping grid sizes require longer times to unwrap, but small variations in the displacement field can be better resolved. On the contrary, coarser grid sizes (Fig. 2.8 c-e) unwrap faster, but might also damp the magnitude of the spatial signal (compare Fig. 2.8 b and e). In our view unwrapping grid sizes between 100 and 125 m in combination with time windows between 60 and 365 days are a good compromise to obtain clear spatial signals if the purpose is to identify landslide signals on a regional scale.

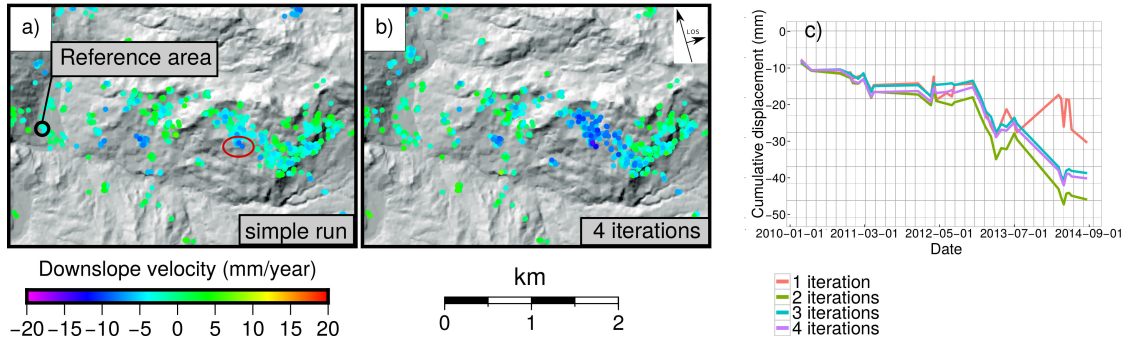


**Figure 2.9:** When running unwrapping and DEM error estimation in an iterative way, mean velocity maps between a) a simple first run and b) running the unwrapping and DEM error estimation four times differ significantly in terms of spatial distribution and magnitude of the displacement signal. c) Time series of the pixels inside the red ellipse in a) for different iterations.

## 2.5.2 Calibrating the interferometric signal for a single landslide cases

Similar to the problem of the reference area, another aspect had significant influence on the final results. As it is also described in the StaMPS manual [pdf-01] and in DUCRET et al. (2014), if unwrapping and DEM error estimation are run in an iterative way, the unwrapped solution can be improved. In a first run the interferograms are unwrapped and the spatially correlated look angle error is estimated. In a second run, the error estimate is subtracted from the wrapped interferograms, the interferograms are unwrapped and the error estimate is added back. Then the spatially correlated look angle error is re-estimated from this new unwrapped solution. Mean velocity maps at Camugnano varied after each iteration and after ca. 4 runs the results remained stable (Fig. 2.9a-b). Also the time series varied. In a first run the deformation in time is underestimated and the relative acceleration during spring 2013 is not clearly visible. In a second run the acceleration period becomes visible, but the results might be slightly overestimated because after a third run the total cumulative displacement is again reduced (Fig. 2.9). After a fourth iteration, little difference occurred with respect to the third run and also after additional repetition the time series remains stable. It is important to note that the time series of the first run might be interpreted in the sense that the landslide came to a halt during the year 2014, while the other solutions indicate a persistent deformation also for the period after the strong deformations of Spring 2013. The latter scenario is in line

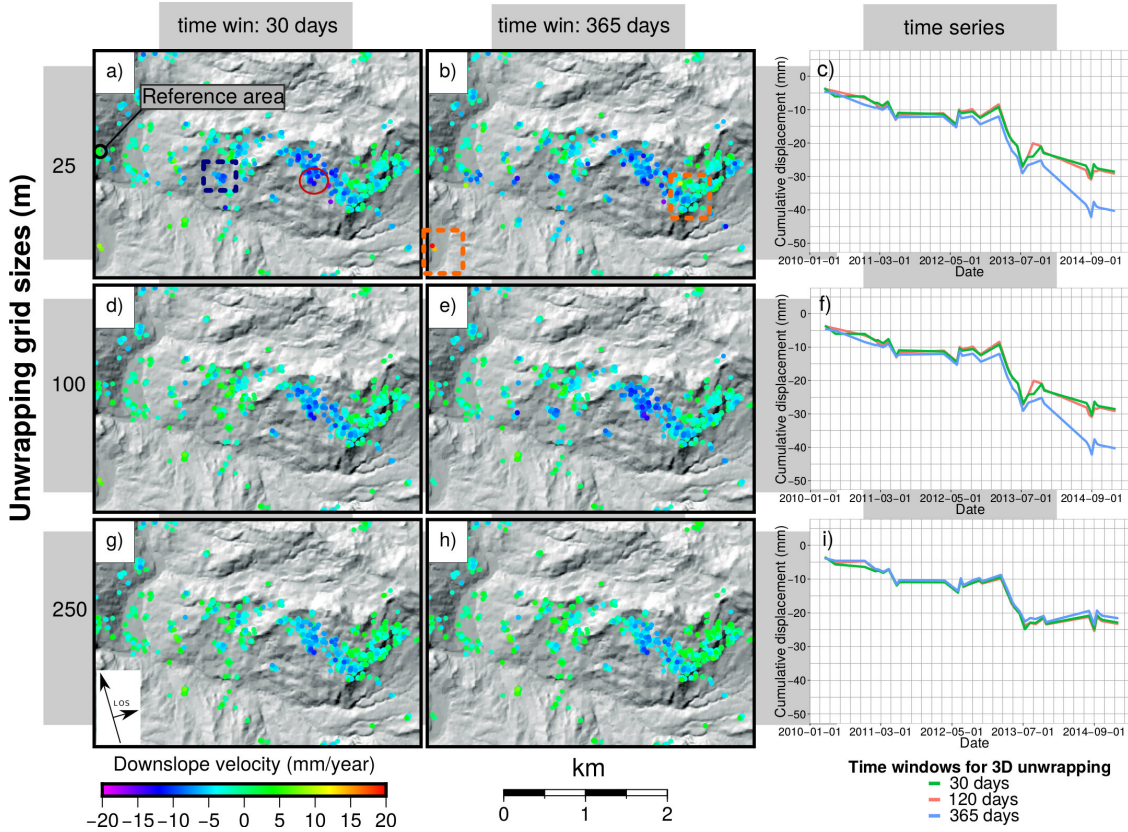


**Figure 2.10:** Mean velocities corrected by the spatially correlated look angle error and orbital ramps for different grid sizes and time windows. First row: small unwrap grid sizes (25 m) for a) 30 days time window during unwrapping, b) 365 days time window during unwrapping. c) time series of the pixels inside the red circle in a). Second row: Medium unwrap grid size (125 m) for d) a time window of 30 days and e) 365 days during unwrapping. f) time series for different unwrapping time windows. Bottom row: Coarse unwrapping grid size (250 m) for g) 30 days unwrapping time window and h) 365 days unwrapping time window. i) Time series for different unwrapping time windows.

with continuing deformation during 2015 that were measured by Sentinel (chapter 5).

The two main processing parameters that influenced the unwrapped solution, are the grid size that is used to downsample interferograms before unwrapping and the time window that is used during unwrapping in three dimensions. As mentioned earlier, also the unwrapping routines can be cost intensive and generally small unwrapping grid sizes and long unwrapping time windows require longer times to solve the unwrapping problem.

Small unwrapping grid sizes often resolve better small scale displacements but may also introduce a speckle like pattern in space. For example the range decreases at

Carpineta (blue rectangle in Fig. 2.10 a) are resolved well only for small unwrapping grid sizes (Fig. 2.10 a-b), while for medium grid (Fig. 2.10 d-e) sizes it only becomes apparent in combination with long unwrapping time windows (Fig. 2.10 e). For coarse grid sizes (Fig. 2.10 g-h), these small scale deformations are undersampled and also the magnitude of the mean velocities is damped. On the other hand, high mean velocities that are measured only on single pixels (orange rectangles in Fig. 2.10 b) should in most cases be interpreted as noise. The signal of these noisy pixels can be smoothed out by larger unwrapping grid sizes.

The two unwrapping parameters have also an effect on the time series products. All grid sizes and time windows resolve an acceleration of the Camugnano landslide during the spring of 2013 (time series in Fig. 2.10 c, f, i). However, for the period after the reactivation, only small and medium grid sizes report continuing deformation, while for coarse grid sizes the signal would suggest a cease of landslide motion. The time windows that were used during unwrapping have only an effect for small and medium unwrapping grid sizes (Fig. 2.10 c, f). Longer time windows appear to solve for higher displacements in time, although the difference is rather small for the years before 2014. The difference becomes more evident for the period after the strong reactivation 2013. After 2014 was characterized only a low number of SAR acquisitions were available and only few of high quality interferograms could be formed. It is possible that longer time windows are capable of recovering the deformation signal in noisy interferograms, as it is suggested by HOOPER & ZEBKER (2007) and HOOPER (2010), which is why the time series for longer unwrapping time windows have a steeper slope. Again, we believe that this solution is the most realistic one, since we show in chapter 5 that during 2014-2015 displacements were measured by Sentinel.

## 2.6 Strategic notes and concluding discussion

In this chapter we showed how the final interferometric result varied according to selected processing parameters. Variation occurred both on the regional and on the local scale. In particular the position of the reference area, pixel selection thresholds and unwrapping parameters had a relatively strong influence on displacements in time and space.

The processing parameters that govern pixel selection and rejection affect the deformation maps. It is important to exclude as many noisy pixels as possible without eliminating those that contain valuable signal. For the results in chapter 4 and 5 we typically started with an analysis of regional scale InSAR results, with low coherence thresholds that admit many noisy pixels and successively adjusted the parameters during pixel weeding to a more restrictive level until the spatial signal became sharper. For regional scale applications we chose medium unwrapping grid sizes between 125 and 150 m in combination with long unwrapping time windows around 365 days. Unwrapping and DEM error estimation was run in an iterative way until the final solution became stable and different reference areas were selected in order to identify relative displacement patterns in space. Then interferometric results can be subsetted in space with respect to single landslide cases that yielded clear signals.

On the local scale pixel selection can be optimized faster and positioning as well as signal can be compared better to field observation. Unwrapped solutions for different processing parameters can be analysed easier and in particular unwrapping with small grid sizes and long time windows, which might be capable of restoring small scale displacements, can be tested because the processing time becomes shorter. In addition different suitable reference areas can be evaluated, which is often a difficult task in areas where most slopes are affected by small displacements and atmospheric conditions might vary on the scale of few kilometers. This is also the reason why we chose to calibrate the InSAR results in chapter 5 on the scale of a single landslide.

We would like to point out that none of the documented variations are actual errors or false solutions and that it is reasonable to systematically test different combinations of processing parameters. This approach has the advantage that one can choose between a signal that is stable for many different parameters or a signal that corresponds best to expected deformation in time and space. On the downside the final result is not an objective solution and depends on the experience and the focus of the operator. Also a significant amount of time needs to be dedicated to the calibration of the InSAR signal.

## 2.7 References

- ADAM, N., EINEDER, M. & KAMPES, B. (2004): Development of a scientific persistent scatterer system: Modifications for mixed ERS/Envisat time series. – ENVISAT & ERS Symposium, **6–10 settembre** (Austria), pp. 1–9; Salzburg.
- AGRAM, P. S. (2010): Persistent scatterer interferometry in natural terrain. – PhD Thesis, Stanford University, 144 pp.; Ph.D. dissertation, Department of electrical engineering, Stanford University.
- AGRAM, P. S. & SIMONS, M. (2015): A noise model for InSAR time series. – Journal of Geophysical Research-solid Earth, **120** (4), pp. 2752–2771;
- BERARDINO, P., FORNARO, G., LANARI, R. & SANSOSTI, E. (2002): A new algorithm for surface deformation monitoring based on small baseline differential SAR interferograms. – Ieee Transactions On Geoscience and Remote Sensing, **40** (11), pp. 2375–2383; New York.
- BOVENGA, F., WASOWSKI, J., NITTI, D. O., NUTRICATO, R. & CHIARADIA, M. T. (2012): Using COSMO/SkyMed X-band and ENVISAT C-band SAR interferometry for landslides analysis. – Remote Sensing of Environment, **119** (1), pp. 272–285; New York.
- BÜRGMANN, R., ROSEN, P. A. & FIELDING, E. J. (2000): Synthetic aperture radar interferometry to measure Earth’s surface topography and its deformation. – Annual Review of Earth and Planetary Sciences, **28** (), pp. 169–209;
- CHEN, C. W. & ZEBKER, H. A. (2001): Two-dimensional phase unwrapping with use of statistical models for cost functions in nonlinear optimization. – Journal of the Optical Society of America A-optics Image Science and Vision, **18** (2), pp. 338–351;
- CORSINI, A., FARINA, P., ANTONELLO, G., BARBIERI, M., CASAGLI, N., COREN, F., GUERRI, L., RONCHETTI, F., STERZAI, P. & TARCHI, D. (2006): Space-borne and ground-based SAR interferometry as tools for landslide hazard management in civil protection. – International Journal of Remote Sensing, **27** (12), pp. 2351–2369; London.

- DUCRET, G., DOIN, M.-P., GRANDIN, R., LASSERRE, C. & GUILLASO, S. (2014): DEM Corrections Before Unwrapping in a Small Baseline Strategy for InSAR Time Series Analysis. – *Ieee Geoscience and Remote Sensing Letters*, **11** (3), pp. 696–700;
- FARINA, P., COLOMBO, D., FUMAGALLI, A., MARKS, F. & MORETTI, S. (2006): Permanent Scatterers for landslide investigations: outcomes from the ESA-SLAM project. – *Engineering Geology*, **88** (3-4), European Geosci Union;
- FERRETTI, A., PRATI, C. & ROCCA, F. (1999): Monitoring terrain deformations using multitemporal SAR images. – *Proceedings CEOS99 (Committee on Earth Observation Satellites)*, **26 –29 October** (1999), p. 4; Toulouse.
- FERRETTI, A., PRATI, C. & ROCCA, F. (2001): Permanent scatterers in SAR interferometry. – *Ieee Transactions On Geoscience and Remote Sensing*, **39** (1), pp. 8–20; New York.
- GUZZETTI, F., MANUNTA, M., ARDIZZONE, F., PEPE, A., CARDINALI, M., ZENI, G., REICHENBACH, P. & LANARI, R. (2009): Analysis of Ground Deformation Detected Using the SBAS-DInSAR Technique in Umbria, Central Italy. – *Pure and Applied Geophysics*, **166** (8-9), pp. 1425–1459; Basel.
- HANDWERGER, A. L., ROERING, J. J. & SCHMIDT, D. A. (2013): Controls on the seasonal deformation of slow-moving landslides. – *Earth and Planetary Science Letters*, **377–378** (1), pp. 239–247; Amsterdam.
- HANSEN, R. F. (2001): *Radar interferometry: data interpretation and error analysis*. – 308 pp.; New York, Boston, Dordrecht, London, Moscow (Kluwer Academic Publishers).
- HILLEY, G. E., BURGMANN, R., FERRETTI, A., NOVALI, F. & ROCCA, F. (2004): Dynamics of slow-moving landslides from permanent scatterer analysis. – *Science*, **304** (5679), pp. 1952–1955;
- HOOPER, A., ZEBKER, H., SEGALL, P. & KAMPES, B. (2004): A new method for measuring deformation on volcanoes and other natural terrains using InSAR persistent scatterers. – *Geophysical Research Letters*, **31** (23), p. L23611; Washington DC.

- HOOPER, A., SEGALL, P. & ZEBKER, H. (2007): Persistent scatterer interferometric synthetic aperture radar for crustal deformation analysis, with application to Volcan Alcedo, Galapagos. – *Journal of Geophysical Research-solid Earth*, **112** (B7), B07407; Washington DC.
- HOOPER, A. (2008): A multi-temporal InSAR method incorporating both persistent scatterer and small baseline approaches. – *Geophysical Research Letters*, **35** (16), p. L16302; Washington DC.
- HOOPER, A. (2010): “A statistical-cost approach to unwrapping the phase of InSAR time series” In: proceeding of international workshop on ERS SAR interferometry, Frascati, Italy vol. 30 2010.
- HOOPER, A. & ZEBKER, H. A. (2007): Phase unwrapping in three dimensions with application to InSAR time series. – *Journal of the Optical Society of America A-optics Image Science and Vision*, **24** (9), pp. 2737–2747;
- KAMPES, B. & USAI, S. (1999): “Doris: The delft object-oriented radar interferometric software” In: 2nd International Symposium on Operationalization of Remote Sensing, Enschede, The Netherlands vol. 16 Citeseer, 1999, p. 20.
- LAUKNES, T. R., SHANKER, A. P., DEHLS, J. F., ZEBKER, H. A., HENDERSON, I. H. C. & LARSEN, Y. (2010): Detailed rockslide mapping in northern Norway with small baseline and persistent scatterer interferometric SAR time series methods. – *Remote Sensing of Environment*, **114** (9), pp. 2097–2109;
- MASSONNET, D. & FEIGL, K. L. (1998): Radar interferometry and its application to changes in the earth’s surface. – *Reviews of Geophysics*, **36** (4), pp. 441–500;
- POGGI, F. & RICELLI, G. (2011): PSI technique for analysing slow landslides: a useful tool to handle with care. – *International Journal of Remote Sensing*, **32** (24), pp. 9521–9546; London.
- ROERING, J. J., KIRCHNER, J. W. & DIETRICH, W. E. (2005): Characterizing structural and lithologic controls on deep-seated landsliding: Implications for topographic relief and landscape evolution in the Oregon Coast Range, USA. – *Geological Society of America Bulletin*, **117** (5-6), pp. 654–668; Boulder.

- ROSEN, P. A., HENSLEY, S., PELTZER, G. & SIMONS, M. (2004): Updated repeat orbit interferometry package released. – *Eos Trans. AGU*, **85** (5), pp. 47–47; Malden.
- SANDWELL, D., MELLORS, R., TONG, X., WEI, M. & WESSEL, P. (2011): GMT-SAR: An InSAR Processing System Based on Generic Mapping Tools, URL: <http://www.escholarship.org/uc/item/8zq2c02m>; – retrieved 05.06.2016.
- SCHMIDT, D. A. & BÜRGMANN, R. (2003): Time-dependent land uplift and subsidence in the Santa Clara valley, California, from a large interferometric synthetic aperture radar data set. – *J. Geophys. Res.* **108** (B9), pp. 1–13; International.
- STROZZI, T., FARINA, P., CORSINI, A., AMBROSI, C., THURING, M., ZILGER, J., WIESMANN, A., WEGMÜLLER, U. & WERNER, C. (2005): Survey and monitoring of landslide displacements by means of L-band satellite SAR interferometry. – *Landslides*, **2** (3), pp. 193–201;
- [pdf-01]:HOOPER, A., SPAANS, K., BEKAERT, D., CUENCA, M. C., ARIKAN, M. & OYEN, A. (2010): StaMPS/MTI Manual Version 3.2, URL: [http://radar.tudelft.nl/~ahooper/stamps/StaMPS\\_Manual\\_v3.2.pdf](http://radar.tudelft.nl/~ahooper/stamps/StaMPS_Manual_v3.2.pdf); – consultato il 10.07.2013.
- WASOWSKI, J. & BOVENGA, F. (2014): Investigating landslides and unstable slopes with satellite Multi Temporal Interferometry: Current issues and future perspectives. – *Engineering Geology*, **174** (), pp. 103–138;

### **3 The influence of external digital elevation models on PS-InSAR and SBAS results: Implications for the analysis of deformation signals caused by slow moving landslides in the Northern Apennines (Italy)**

**Authors:** Benedikt Bayer, David Schmidt and Alessandro Simoni

**Publication details:** Published in Transactions on Geoscience and Remote Sensing (Volume 55, Issue 5)

## **Abstract**

Advanced InSAR post processing, like PS-InSAR, offer the possibility to investigate slow moving landslides, where standard interferometry is problematic. These advanced algorithms involve the analysis of a series of SAR acquisitions in both time and space. One input that requires particular attention for landslide applications is the external digital elevation model that is used to correct the interferograms for the topographic phase term. When multiple elevation datasets are available for a given study area, it is difficult to decide which one should be used. In this paper, we test the sensitivity of PS-InSAR/SBAS results to different digital elevation models. The study area is located in the Northern Apennines of Italy, where chaotic clayshales and fine-grained flysch host slow moving earth flows and ancient rock-slides. C-Band (Envisat) and X-Band (Cosmo-SkyMed) data are processed with different digital elevation models. We describe a simple framework to statistically analyse the influence of these models on the final PS-InSAR/SBAS results. We find that individual interferograms do not vary much depending on the DEM, while the results from PS-InSAR and SBAS analysis do vary. This is likely caused by the way the DEM error is estimated. We find also that the quality of the DEM is more important than the resolution and that X-Band InSAR data is more sensitive to the choice of the DEM than C-band. The significance of the results are discussed with reference to two landslide areas.

### 3.1 Introduction

Over the last two decades, interferometric synthetic aperture radar (InSAR) has revolutionized the measurement of small displacements on the earth surface. To resolve these small displacements, differential interferograms are produced by interfering two synthetic aperture radar (SAR) scenes and removing the topographic component of the phase, which would otherwise obscure the displacement for SAR pairs with non-zero perpendicular baseline. The phase term due to topography is linearly related to the height at a given point, the distance between sensor and target, the perpendicular baseline of an interferogram and the wavelength of the satellite (MASSONNET & FEIGL, 1998; ROSEN et al., 2000; HANSSEN, 2001; FERRETTI et al., 2001; HOOPER et al., 2007). Since the interferometric phase is measured in modulo  $2\pi$ , a certain height, generally referred to as height of ambiguity, will introduce a  $2\pi$  phase cycle and as a consequence a spatial pattern that is known as topographic fringes (HANSSEN, 2001). An independent digital elevation model (DEM) provides a means to forward model and remove the aforementioned topographic phase. However, artefacts or systematic errors in the DEM will introduce a phase term that is again proportional to the perpendicular baseline and may be misinterpreted as a signal (MASSONNET & FEIGL, 1998, p. 462). Even in stacking approaches, the contribution by this error term to the InSAR derived velocities averages out only if the sum of all baselines in the stack is close to zero (SAMSONOV, 2010). This is a known problem for satellites with drifting baselines like ALOS and has been reported in works related to volcanic processes (SAMSONOV, 2010; VAJEDIAN et al., 2015) and landslides (SUN et al., 2015).

Several studies have developed processing strategies that help to mitigate the effects of DEM artefacts (FATTAHI & AMELUNG, 2013; BERARDINO et al., 2002; HOOPER et al., 2007; SAMSONOV, 2010), and these strategies have been incorporated into different InSAR processing schemes. The two most common advanced schemes are the Persistent Scatterers (PS in the following, e.g. FERRETTI et al., 2001; HOOPER et al., 2007) and Small Baseline time series (SB in the following, e.g. BERARDINO et al., 2002; SCHMIDT & BÜRGMANN, 2003) approaches. Recently, both techniques have been implemented in a common open source framework of StaMPS (Stanford Method of Persistent Scatterers, HOOPER, 2008).

Some authors contend that the influence of the DEM on PS-InSAR processing is of minor importance, since the processing chain corrects for the phase caused by DEM error (FERRETTI et al., 2001, p. 11), (HOOPER et al., 2007, paragraph 26). Other authors deem that greater accuracy/precision of the DEM benefits the InSAR processing when it comes to landslide applications (COLESANTI & WASOWSKI, 2006, p. 180, MASSONNET & FEIGL, 1998, p. 485).

The influence of the external DEM on PS-InSAR results has been discussed for an InSAR study on slope movements in the three Gorges region in China (TAN-TIANUPARP et al., 2012). The authors found that both the selected PS-pixels and the deformation maps deviated if different DEMs were used. Despite the clear description of the problem, several questions have not been answered: How sensitive are InSAR results to the choice of DEM? How does it influence the pixel selection in the PS and SB algorithms? How can a DEM artefact be distinguished from a deformation signal that is caused by a landslide?

When several DEMs are available for a study area, one must decide which of them will be used during the processing. For remote areas, a performance evaluation of these digital elevation models for InSAR purposes might be of interest. More recently, several X-band SAR data sets have become available. The cited works use imagery from the C-band satellites Envisat/ERS or L-band data from ALOS . Given the shorter wavelengths and the lower height of ambiguities in X-band data, the accuracy of the external DEM might be of greater concern.

In the present paper, we quantify how the choice of DEM influences InSAR results for the purposes of resolving the movement of active landslides. We assess PS- and SB-results derived from Envisat and Cosmo SkyMed imagery for the Northern Apennines of Italy using a collection of regional and global DEMs for topographic correction. The study area is located approximately 50 km south of Bologna in the Northern Apennines of Italy (Fig. 3.1) where chaotic clay-shales and turbidites are among the dominant lithologies (PINI, 1999; PANINI et al., 2002). Both lithotypes are highly prone to landslides that are mostly classified as slow-moving earthflows (CRUDEN & VARNES, 1996; BERTI & SIMONI, 2010; SIMONI et al., 2013). The Mediterranean climate of the study area is characterized by high precipitation in the winter, intense rainstorms in the spring and autumn months, and relatively dry periods during the summer. The topography is generally gentle, rarely exceeding 20 degrees of slope. And moderate vegetation, in combination with high displacement

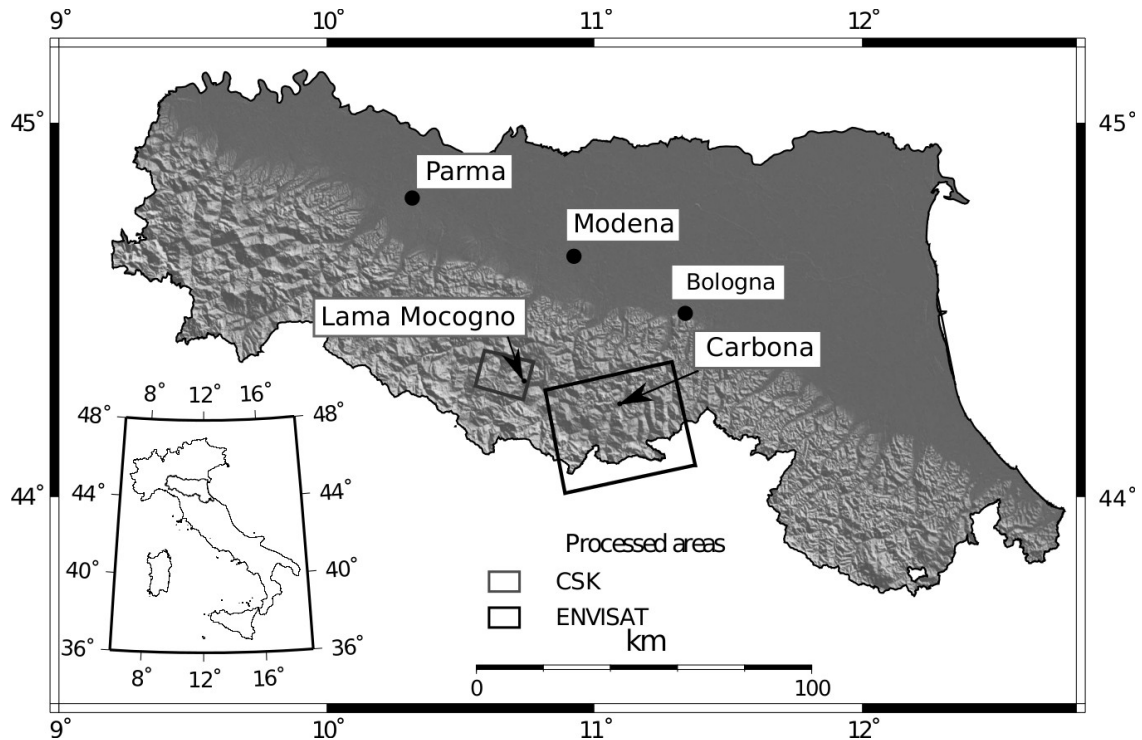


**Figure 3.1:** The study areas are situated approximately 40 km S of Bologna and Modena in the northern Apennines of Italy.

rates on the slopes, cause decorrelation in many areas. Standard 2-pass interferometry is of limited use (CORSINI et al., 2006, p.2365), and the aforementioned post-processing techniques give more promising results. We document movement at two local study sites and compare how the results vary given the DEM. The geological conditions at the local study areas are common in the Northern Apennines, and hence they can be considered representative from a geological and geomorphological point of view. The SAR frames used in the analysis are plotted in Fig.3.1 together with the two study sites.

## 3.2 Materials and Methods

### 3.2.1 Satellite datasets and InSAR processing

We use the Stanford Method of Persistent Scatterers (StaMPS, HOOPER et al., 2007) to process satellite data from Envisat (C-Band, 5.6 cm) and Cosmo-SkyMed (X-Band, 3.1 cm). Raw data were focussed with ROI-PAC (ROSEN et al., 2004) and

interferometric processing was carried out with DORIS (KAMPES & USAI, 1999). 20 Envisat scenes from an ascending pass are processed with the Persistent Scatterer (PS) implementation of StaMPS. The single master stack for PS-processing contains 19 interferograms spanning a period from March 2004 to August 2010 (Fig. 3.2 a). Additionally, 24 Cosmo-SkyMed scenes on a descending pass are processed using the independent Small Baseline module of StaMPS. The Cosmo-SkyMed interferograms used in the SB-analysis are pre-selected for short temporal and spatial baselines. 54 Interferograms were considered for the period between September 2012 and December 2013 (Fig. 3.2 b). Only those interferograms with a clear phase signal were included in the PS-/SB-analysis. This strategy improved the quality of the spatial and the temporal signal and helped to overcome many problems caused by temporal decorrelation. In the following we will refer to the results from the different processing strategies as PS- and SB-results. For both approaches we used consistent processing parameters for the different DEMs, i.e. one set of parameters for PS-processing and another set for Small Baseline processing.

Early PS-InSAR algorithms (FERRETTI et al., 2001) used amplitude dispersion for an initial selection and estimated coherence for each pixel assuming a deformation model in order to identify PS pixels. After pre-selection of candidates by amplitude dispersion, StaMPS uses phase stability instead of a deformation model to estimate coherence and select PS/SB-pixels. As explained in detail in (HOOPER et al., 2007, paragraphs 38 to 44), the estimation of the phase stability requires that the spatially uncorrelated look angle error in the interferograms, which contains the spatially uncorrelated parts of the topographic error, is calculated and removed. During the selection procedure, this is done by inverting the wrapped phase for a linear relationship between phase and perpendicular baseline. The inferred proportionality constant is the phase term related to the DEM error and before the unwrapping procedure, the wrapped phase is corrected by this spatially uncorrelated phase term. In a separate step after unwrapping, StaMPS also estimates the spatially correlated look angle error from the unwrapped phase. This is done in an iterative procedure that involves inverting for the relationship between perpendicular baseline/unwrapped phase and low pass filtering in space. This error estimate contains both spatially correlated and uncorrelated parts of the topographic error.

In the SB- implementation of StaMPS this can be done in either in the interferogram domain, as it is described in BERARDINO et al. (2002) or in the time domain,

**Table 3.1:** DEM statistics containing the RMSE from the literature and the standard deviation  $\sigma_h$  obtained from the accuracy assesment. The ascending Envisat data has been processed for an area of ca. 1700km<sup>2</sup> and the descending Cosmo-SkyMed data for 250km<sup>2</sup>. The backslash separate results for Envisat and Cosmo-SkyMed.

Parameter	RDEM	NDEM	ASTER	SRTM	XSAR
Year of acquisition	1974	1954	2001-2002	2000	2000
Published RMSE [m]	ca. 3	–	ca. 15	8	–
Resolution [m]	10	20	ca. 30	ca. 30	ca. 30
$RMSE_{h(geo)PS/SB}$ [m]	7.33 / 13.05	9.96/ NA	7.64 / NA	6.06/ 13.25	NA / 25.98
$RMSE_{h(radar)PS/SB}$ [m]	2.66 / 3.79	4.42 / NA	3.16 /NA	2.47/3.01	NA/6.674
$RMSE_{vPS/SB}$ [mm/a]	3.424/ 3.451	3.969 / NA	3.581 / NA	3.265/ 3.455	NA / 3.497
Registered points (Envisat/CSK)	26211/45935	25937/NA	26218/NA	26712 /45121	NA/43156

as it is described in FATTAHI & AMELUNG (2013). While DEM artefacts should be removed through the aforementioned methods, it is not always clear how successful this is.

### 3.2.2 The External Elevation data

For the study area in the Northern Apennines, five digital elevation models are available that differ in acquisition mode of the elevation data (i.e. optical versus radar), acquisition date, and spatial resolution. The most frequently used DEM in interferometric processing is the 1-arc second (ca. 30 m) SRTM digital elevation model (RODRIGUEZ et al., 2006), which was acquired using a C-band radar system. During the SRTM mission, X-band SAR data was also collected, and used to produce a DEM (XSAR in the following) with a resolution of ca. 25 m (RABUS et al., 2003). Due to the narrow illumination swath of the X-Band antenna, only a limited area of the earth surface is covered and this DEM contains large deviations from other topographic data in steep terrain (HOFFMANN & WALTER, 2006; KOLECKA & KOZAK, 2014).

Another global digital elevation model is provided by ASTER, which has a reported resolution of 1 arcsecond and is derived from infra-red satellite imagery (WELCH et al., 1998; ECKERT et al., 2005). Additionally, there are two digital elevation models available in the study area that are derived from optical imagery. One covers the whole terrain of Italy (NDEM in the following). It has a resolution of 20 m, but unfortunately there are no accuracy estimates available from the literature. The other optical DEM covers the region of Emilia Romagna in Italy (RDEM

in the following) and has a resolution of ca. 10 m. It is based on topographical data originally acquired during the 1970s. A RMSE value of ca. 2 m for RDEM has been reported (DAEHNE, 2014, chapter 5), when compared to higher resolution optical and LIDAR imagery in areas that are regarded stable and not affected by landsliding. The RMSE values for the other DEMs found in the cited works are summarized in Table 3.1. It is important to note that the elevation data from SRTM and ASTER contain the heights of houses and tree tops and are hence digital surface models. RDEM and NDEM on the other hand report only the bare ground. For simplicity we will refer throughout the work to both types as DEMs. All DEMs report the height with respect to the geoid (EGM2008).

### 3.2.3 Sensitivity analysis

The accuracy of digital elevation models is usually assessed by comparing a given DEM to other elevation datasets, which can include GPS transects or other independent DEMs (e.g. RABUS et al., 2003; RODRIGUEZ et al., 2006). We will use the term DEM accuracy to indicate the deviation from the true value of the topography as the SAR satellite would measure it, i.e. containing the heights of the houses and the tree tops. Moreover an accurate DEM would minimize the phase term that scales with the baseline after the topographic phase has been subtracted from the interferogram. For the purpose of using DEMs from InSAR, precision is a problematic term since it relates in part to the resolution of the elevation data and in part to its random error. For instance, if the resolution of a digital elevation model is approximately 30 m, the spatial sampling is relatively low. In this work only to the terms accuracy and resolution. In order to analyze the general influence of the DEM on PS-InSAR processing, we process Envisat SAR data using SRTM, ASTER, RDEM and NDEM elevation models. A framework to evaluate the influence of the DEM on the various processing steps has been established following similar procedures for DEM comparison in the literature (RABUS et al., 2003; HOFFMANN & WALTER, 2006; RODRIGUEZ et al., 2006):

1. **DEM comparison in geographic coordinates:** Each digital elevation model has been oversampled by bicubic interpolation to a common resolution of 10 m and compared to the mean of all DEMs. We decided to oversample in order to maintain differences due to detail in the high resolution elevation

data, which might be an advantage for our Cosmo SkyMed dataset. The residual height maps are compared statistically by means of the root mean squared error.

2. **DEM comparison in radar-coordinates:** In order to subtract the topographic phase from the interferograms, the digital elevation models are resampled into the radar geometry (range and azimuth). Each radar-coded DEM is then compared again to the mean of all DEMs.
3. **Comparison of stacked interferograms:** The wrapped interferograms that are corrected by the topographic phase are stacked to obtain mean velocities. In analogy to the first two steps, each stack is differenced with respect to the mean of all stacks. Then the residuals are compared statistically to determine the influence of the DEM before any post-processing algorithm is run or corrections are applied.
4. **Qualitative analysis of the PS-InSAR and SBAS results:** In a last step, regional and local differences in the line-of-sight (LOS) results for PS-InSAR/SBAS are visually inspected and compared, with special attention given to the number, location, and phase signal of the selected PS pixels. A reference area that is deemed stable is selected as close as possible to the areas of interest.

Due to the large file size of the X-band SAR imagery, the framework described above is only partly applied to Cosmo-SkyMed SAR data. The Cosmo-SkyMed data has been processed with the XSAR, the normal C-Band SRTM, and RDEM in order to analyze the influence of the acquisition mode, the reference surface, and the resolution. Because XSAR contains large areas with no data values, a common mask has been applied to all DEMs to make the results comparable.

#### **3.2.4 Theoretical and statistical evaluation of the DEM influence on InSAR processing**

As mentioned before, the phase that is introduced by error in the digital elevation model is proportional to the perpendicular baseline. For each pixel of a given in-

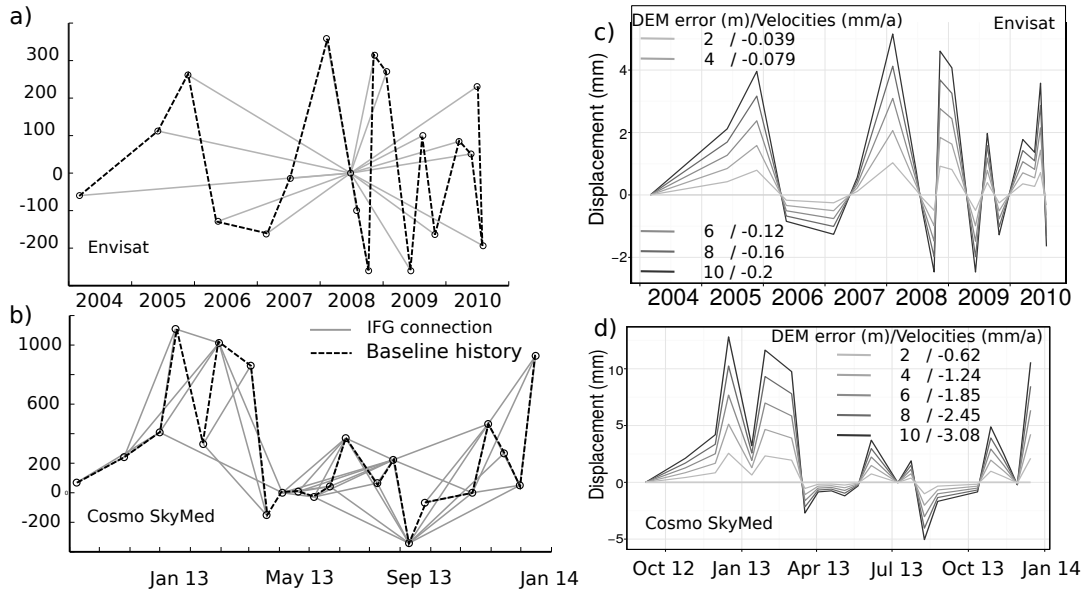


**Figure 3.2:** a) Interferogram combinations and baseline history for the PS-processing with Envisat. b) Interferogram combinations and baseline-history for SB-processing with Cosmo-SkyMed. c) Theoretical displacement in time and mean velocities that would be introduced by a DEM artefact for our Envisat network and d) for the Cosmo SkyMed dataset.

terferogram this phase term can be written as (HANSSEN, 2001, p. 66, HOOPER et al., 2007 FATTAHI & AMELUNG, 2013):

$$\phi_{DEM} = \frac{4\pi}{\lambda} \frac{B_{\perp}}{R \sin(\theta)} \Delta h \quad (3.1)$$

Where  $\lambda$  is the wavelength of the satellite,  $R$  is the distance between sensor and target,  $B_{\perp}$  is the perpendicular baseline,  $\theta$  is the incidence angle and  $\Delta h$  is the DEM error. Although this relationship is rather simple for standard interferometry, the fact that the interferometric phase is measured in modulo  $2\pi$  (DUCRET et al., 2014), the probabilistic nature of PS-selection (HOOPER et al., 2007), as well as filtering and plane fitting operations (HANSSEN, 2001) introduce non linearities during multi-temporal InSAR processing. It has recently been demonstrated that a time-dependent artefact in InSAR time series that is caused by DEM errors scales with baseline history (see FATTAHI & AMELUNG, 2013 for a detailed mathematical description of the problem). The dashed lines in Fig. 3.2 a and b show the baseline history for the two processing strategies that have been employed. We calculated synthetic time series for a theoretical PS that would be caused by different degrees

of DEM errors using the inversions implemented in the StaMPS. Fig. 3.2 c) and d) show these theoretical time-series and document the influence of the baseline networks and the wavelength of the satellites. The effect of the DEM error on the mean velocities of our datasets is in both cases low. For Envisat a DEM error of 10 m would reduce the mean velocities by only 0.1 mm/a, while for Cosmo SkyMed a DEM error of 10 m would reduce the mean velocities by ca. 3 mm/a (Fig. 3.2 c, d). The influence of the topographic error on the time series is however more complicated. If the DEM error is not estimated, the time series for Envisat (Fig. 3.2 a, c) would simply be dominated by a higher scatter. But for Cosmo-SkyMed, a non linear signal might be visible (Fig. 3.2 b, d) with strong displacements during Spring 2013. Also, our baseline network for Cosmo SkyMed is more sensitive to topographic errors. A DEM error of 2 m would introduce displacements up to 5 mm in the time steps of Spring 2013. This effect can be explained by the short wavelength of Cosmo SkyMed together with the presence of large perpendicular baselines.

The altitude of ambiguity evaluate the general sensitivity of the dataset towards DEM errors. After the removal of the topographic phase, DEM artefacts will introduce a spatial fringe pattern that is proportional to the perpendicular baseline and the value of the DEM error (MASSONNET & FEIGL, 1998, p. 462). For our Envisat dataset, the lowest height of ambiguity is 23 m, the mean height of ambiguity is 88 m with a standard deviation of 128 m. Cosmo SkyMed has a mean height of ambiguity of 15 m (standard deviation: 83 m), which is still beyond the accuracy of most digital elevation models. However, the lowest height of ambiguity for this dataset is only 3 m. It is important to note that it depends on the spatial nature of the DEM artefact. If it occurs on long spatial wavelengths it would simply introduce a signal which is similar to an orbital ramp. If the artefact is very local it might produce a fringe pattern in large-baseline interferograms, cause problems during unwrapping, and introduce the aforementioned baseline correlated scatter.

In order to correctly evaluate the observed differences in the statistical sensitivity analysis, we developed a Monte Carlo approach to test the influence of a phase term due to DEM error on the final InSAR results. We first generated a grid with the same dimensions of the interferograms, and calculated random DEM errors  $N(\mu = 0, \sigma^2 = 5)$ . For each interferogram we calculated a phase term due to this error using the relationship from equation 3.1. We added the grid of the DEM error phase term to the corresponding interferogram and repeated the operation for all interferograms

in our datasets. Then we averaged the modified interferograms in a stack that we compared to the original stack by means of the root mean squared error. This procedure has been repeated for 80 error ranges between 0.5 and 40 m in steps of 0.5 m. The results of this experiment are reported in Fig. 3.4 h-j and are discussed in detail together with the statistical results.

As mentioned earlier, the topographic error term should not have a great influence on the mean velocity maps. However, the spatially uncorrelated DEM error is calculated in StaMPS in order to estimate the phase stability and select PS/SB-pixels. It is difficult to describe mathematically the relationship of the DEM error and the pixel selection in StaMPS. This is why we used a Monte Carlo sampling strategy to evaluate the sensitivity of the pixel selection procedures and our baseline network to topographic errors. On a subset of the overall PS- and SB-results we introduced random phase terms due to the topographic error into the phase of the PS-candidates and executed the processing chain. We repeated this procedure for 40 error ranges and compared the number of registered points to the introduced DEM error. The results are reported in the Fig. 3.4 k.

## **3.3 Impact of the external digital elevation models on InSAR-results**

### **3.3.1 DEM comparison in geographic coordinates**

A comparison of DEMs shows that all of them contain locally large differences in height. The top row of Fig. 3.3 reports the residual heights, in geographic coordinates, for all DEMs that have been used to process the Envisat data. NDEM shows the largest differences with respect to all other models, especially in the mountainous area. In part, these differences can be interpreted as a relative offset between the digital elevation models. This is illustrated in the histograms of residual height that show a small offset of their mean value (Fig. 3.4 a).

We also observe localized differences that may be inherited from the source imagery or data. While RDEM and NDEM are elevation models in the strict sense that give a measure for the elevation of the ground, SRTM and ASTER are digital surface models that also contain the heights of houses and trees. It is also possible that

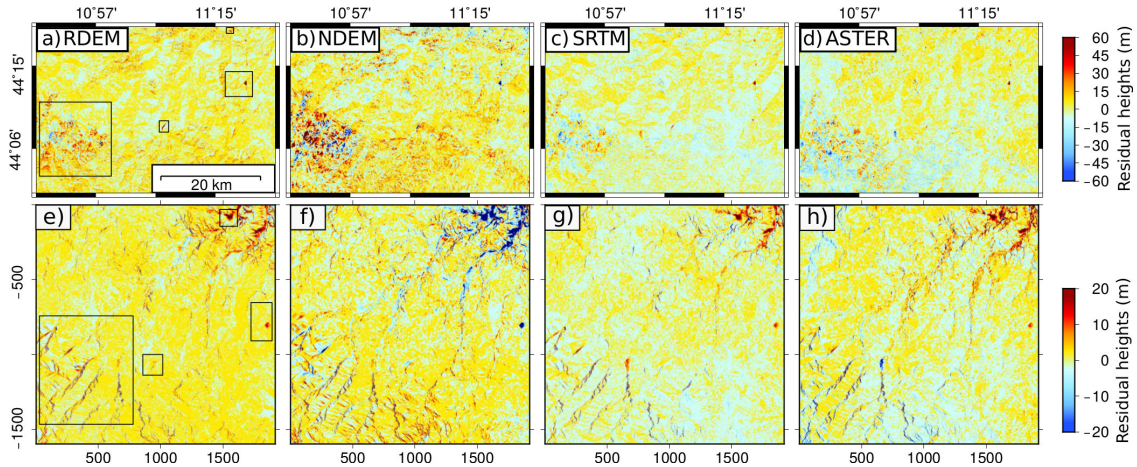


**Figure 3.3:** The top row (a-d) shows the residual heights of the digital elevation models in geographic coordinates (east-north axes), relative to a mean height. In the bottom row (e-h), the residual re-sampled heights of the radar-coded DEMs are reported (range-azimuth axes). In geographic coordinates, differences in the elevation data are caused by relative shifts and localized discrepancies. In radar geometry, many of those differences disappear when the DEMs are resampled to radar coordinates. The rectangles in a) and e) show corresponding areas in geographic and radar coordinates.

differences in the elevation models are caused by the alteration of the surface over time. Differences may result from the different acquisition dates since the RDEM and NDEM are derived optical datasets dating back to the 1970s. An alteration of the topography can be caused by landslides as well as by human activities such as excavation, construction, and the associated accumulation of material. A comparison with LIDAR derived datasets showed that on active landslides the elevation can change up to 12 m since the acquisition of RDEM (DAEHNE, 2014, p. 86 f.).

Finally, local differences may be due to intrinsic errors from post-processing, i.e. interpolation problems during the digitalization of optical data or the errors described for SRTM (RODRIGUEZ et al., 2006). Also the orthorectification process in case of elevation data derived from optical imagery can introduce errors. These aspects should be kept in mind when the DEMs are compared statistically and the root mean squared error of the residual heights is taken as a measure of relative error. In the geographic domain, the SRTM has the smallest variance (Fig. 3.4 a) with an RMSE of only 6.06 m. The distributions of RDEM and ASTER show similar shapes with different means, although the RMSE for ASTER (7.64 m) is slightly larger than for the regional model (7.33 m). NDEM has a very wide distribution

and the highest RMSE (9.97 m), which might indeed indicate larger local errors. All statistical results are summarized in Table 3.1.

### 3.3.2 DEM comparison in radar-coordinates

In order to remove the topographic phase from the interferograms, the DEM is resampled to radar-coordinates at the resolution of the SAR scenes. Given that the resolution of SAR is coarser than some of the DEMs, this diminishes the advantages of using a higher-resolution DEM. The native resolution of Envisat is 5 m in azimuth and 20 m in range; Resampling the DEM to a coarser resolution might also introduce aliasing errors, if the DEM resolution is significantly higher than the radar resolution. The resampling process may also eliminate differences that are caused by horizontal and vertical offsets of the DEMs in geographic coordinates. Differences that are due to the orthorectification procedure and differences that can be found in complicated topographic zones of layover and shadow will also disappear. This is best illustrated for the Envisat results shown in Fig. 3.4 b, because all statistical distributions of the residual heights have almost the same mean values and the magnitude of the residuals decreases. The residual height maps in Fig. 3.3 b also show that the absolute differences between the different DEMs become smaller. In particular, the high residuals visible in the geographic differential height maps of the NDEM, vanish almost completely after the transformation to radar coordinates, which is also reflected by a lower RMSE for all DEMs (Tab. 3.1). We find that the SRTM has the narrowest distribution with a root mean square error of 2.47 m, followed again by RDEM (2.66 m), ASTER (3.16 m). NDEM continues to exhibit the highest RMSE (4.42 m).

We also resampled and converted the DEMs into radar coordinates assuming a viewing geometry for Cosmo-SkyMed, which has a higher spatial resolution than Envisat. Given that SRTM and XSAR have coarser spatial sampling than Cosmo-SkyMed, these DEMs get oversampled. In geographic coordinates the RDEM has the lowest root mean squared error (13.05 m) followed by SRTM (13.25 m) and XSAR (25.98 m). In radar coordinates the ranking changes and SRTM has a lower RMSE (3.01 m) followed by the RDEM (3.79 m) and XSAR (6.674 m). We consider these values biased for two reasons. On the one hand only three DEMs have been compared for the Cosmo-SkyMed data, which might be not enough to identify er-

### 3 Influence of digital elevation models on InSAR results

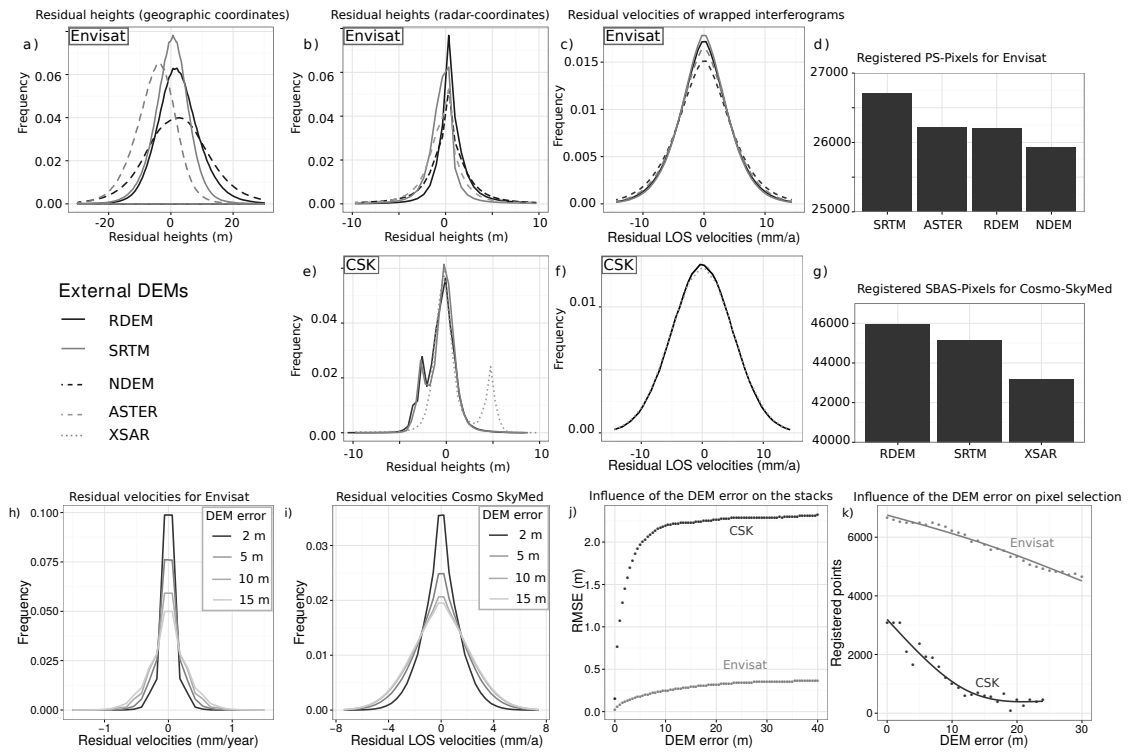


**Figure 3.4:** Statistical evaluation of the DEMs and the interferometric products for Envisat (top-row: a-d) and Cosmo-SkyMed (CSK, bottom row: e-g). The lower row (h-k) reports the results of the theoretical evaluation, based on a Monte Carlo sampling approach. a) Residual heights in geographic coordinates for the DEMs used during PS-processing with Envisat; b) Residual heights in radar geometry for the DEMs used during PS-processing; c) Residual velocities of the wrapped differential interferograms; d) Number of PS-pixels selected for Envisat. e) Residual heights in radar geometry for the DEMs used during SBAS-processing; The two peaks in the distributions are caused by systematic errors in XSAR (see text for details) f) Residual velocities of the stacked wrapped and filtered differential interferograms; g) Number of SBAS-pixels selected for Cosmo-SkyMed. h) Distribution of the residual velocities for modified Envisat stacks with respect to the original stack. i) Distribution of the residual velocities for modified Cosmo SkyMed stacks with respect to an unmodified stack. j) Relationship between the artificially introduced DEM error and the RMSE between the original stack and the modified stack for both Cosmo SkyMed and Envisat. k) Number of pixels selected for different DEM errors.

rors in the elevation data only by means of the standard deviations. Moreover the form of the residual heights in radar coordinates (Fig. 3.4e) show that XSAR has a systematic difference. The small peak on the right is caused in part by the limited coverage of both ascending and descending passes over the study area and in part due to overlay and shadow effects of the acquisition geometry of XSAR.

### 3.3.3 Comparison of stacked interferograms

To assess the influence of the external DEM on the interferometric results, we compare a common set of differential interferograms that are created using different DEMs. These differential interferograms contain the wrapped phase that has been corrected by the topographic term. The residual velocities are plotted for a stack of 19 Envisat interferograms (Fig. 3.4 c). All of these interferograms share a common master. While the distributions are nearly identical, the stacked interferograms can be ranked by lowest RMSE for SRTM (3.26 mm/a), RDEM (3.42 mm/a), Aster (3.58 mm/a) and NDEM (3.96 mm/a).

The residuals of the mean velocities for Cosmo-SkyMed interferograms show almost no difference in the distribution, although slight differences can be observed in the root mean squared error (Tab. 3.1). RDEM shows the smallest variation in the residual velocities (3.45 mm/a), followed by SRTM (3.46 mm/a) and XSAR (3.50 mm/a).

The results from the theoretical error analysis (Fig. 3.4h-j) illustrate that a systematic DEM error influences the shape of the distributions obtained by subtracting a stack of modified interferograms with respect to the original stack. Fig. 3.4 h shows the residual velocities for our Envisat interferogram stacks that contain different degrees of DEM errors with respect to the unaltered stack. For Envisat, the shape of the distributions for the different degrees of error are relatively narrow when compared to the results for CSK, which suggests that the present interferogram network is less sensitive to DEM errors. Fig. 3.4 i shows the distribution of the residual velocities obtained from subtracting the Cosmo SkyMed stacks that contain different degrees of DEM artefacts from an unmodified stack. Compared to the Envisat data the distribution is wider which suggests that DEM errors have a stronger impact on the interferogram network of Cosmo SkyMed. This is consistent with the presence of large baseline interferograms, short radar-wavelength and significantly lower height of ambiguities of the Cosmo SkyMed dataset compared to the Envisat network. Fig. 3.4 j shows the RMSE in relation to the introduced DEM error, and the rapid increase of the RMSE curve for the Cosmo SkyMed dataset suggests that the influence of the DEM error is also strong for small DEM errors (below 5 m). Despite the relatively low sensitivity of the Envisat network to an artificial DEM error, the strongest variations occur also in this dataset for small artefacts.

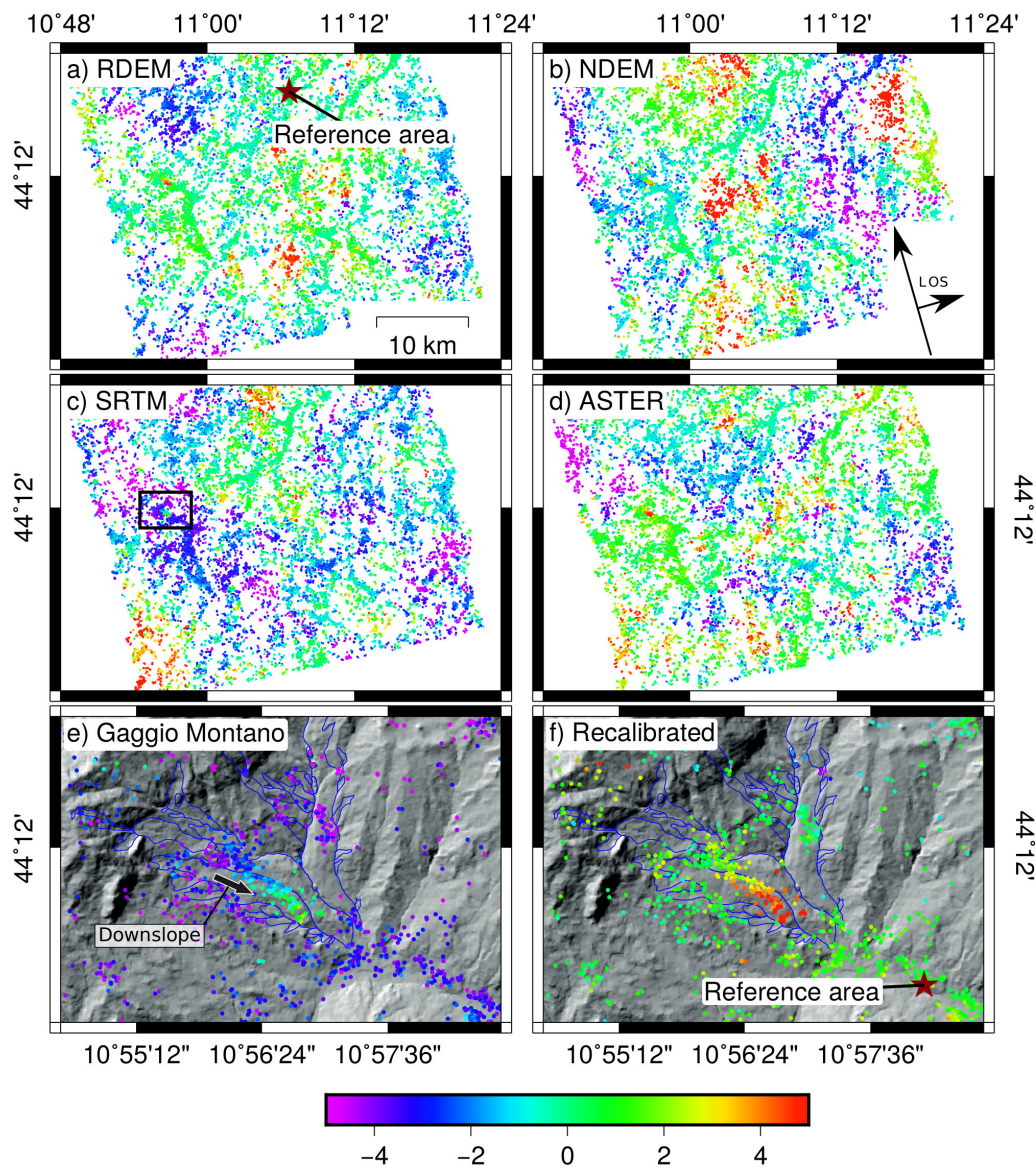
## 3.4 Qualitative analysis of the PS- and SB-results

### 3.4.1 Differences on a regional scale

While marginal differences are observed in the line-of-sight velocities when differential interferograms are stacked and compared, we observe more variability when the InSAR data are processed using the different DEMs. The selection of PS-pixels is moderately dependent on the DEM. Fig. 3.4 and Tab. 3.1 show that for our Envisat data, the most PS-pixels (26712) are registered using the SRTM for an area of ca. 1700 km<sup>2</sup>, followed by Aster and RDEM which yield almost identical numbers (26218 and 26211, respectively). The fewest points are selected if the NDEM is used (25937). For Cosmo-SkyMed, RDEM produced the highest number of SB-pixels (45935) compared to the SRTM (45121) and XSAR DEM (43156). The larger number of overall SB-pixels chosen for Cosmo-SkyMed compared to the Envisat reflects the different resolution of the two datasets.

As mentioned earlier, the spatially uncorrelated part of the DEM error is calculate during phase analysis in order to estimate coherence. An external constraint on the height of the topographic error can be imposed in the processing chain, which works as a threshold. The number of points that are registered is hence in part a function of the DEM error, the linear relationship between perpendicular baseline and wrapped phase, and this threshold. The theoretical analysis of the DEM error suggests that relatively small errors reduce the number of registered points (Fig. 3.4 k). Both baseline networks show already decrease in registered points for small errors (0.1 m to 5 m), and the X-band dataset is more sensitive to the artificial error. The relation between imposed error and number of registered points shows a non-linear relationship. In practice, the difference in the number of registered points is small compared to the theoretical evaluation, which is why the number of points can be considered as an indicator for DEM-accuracy only if it differs significantly for different DEMs.

The line-of-sight velocity maps obtained by PS-processing for the ascending Envisat data show significant differences on a regional scale if different DEMs are used during the processing (Fig. 3.5). The interferometric patterns appear patch-like and often follow topographic and morphological features like ridges or rivers. These differences are most likely introduced during the unwrapping step (phase-jumps), since



Mean velocity along LOS (mm/year)

**Figure 3.5:** PS-results using different external digital elevation data with Envisat data. All mean velocities are measured along the line-of-sight (LOS) and are corrected by DEM- and orbital error. Moreover atmospheric contributions are filtered statistically. a) RDEM, b) NDEM, c) SRTM, d) ASTER. e) A phase jump occurred between the reference area and the town of Gaggio Montano (black frame in c). f) Only after resetting the reference area closer to the slide the signal becomes easier to identify. The landslide perimeters have been compiled from a regional inventory (SERVIZIO GEOLOGICO, SISMICO E DEI SUOLI DELLA REGIONE EMILIA-ROMAGNA, 2014) and are represented by the blue lines.

wrapped interferograms show very view differences. Phase-jumps seem to appear more frequently in areas where few PS/SB-pixels are registered. Given that our primary interest is landslides, which produce a very localized deformation signal, these aerially extensive differences are not particularly important for our purposes. Setting the reference area close to the landslide of interest will often, but not always, eliminate the local differences. At a certain distance from the reference area, however, the aforementioned phase jumps can mask local gradients in the phase and make it challenging to identify a deformation pattern. This is well illustrated by a landslide complex in the town of Gaggio Montano (Fig. 3.5 e-f). This landslide has been studied in the past with standard two-pass interferometry (CORSINI et al., 2006) and the relative signal is well visible in all processed datasets. However for the SRTM it is not immediately clear, because a phase jump occurred between the reference area (Fig. 3.5 c) and the area of interest. After recalibrating using a reference pixel close to the slide, the landslide signal is more distinct and the absolute values are correct. The relative signal in both cases is consistent, only the absolute values differ.

#### **3.4.2 The Carbona landslide: An example of local differences for Envisat**

The Carbona landslide is located approximately 3 km South of Vergato and can be classified according to the scheme proposed in CRUDEN & VARNES (1996) as a slow-moving complex/composite earthflow. The substratum is composed of chaotic clay-shales (PANINI et al., 2002) that include marl- and limestone clasts (see also PINI, 1999). The maps in Fig. 3.6 show the PS-results for the ascending Envisat pass. A deformation signal is only resolved if the 30 m SRTM is used (Fig. 3.6 d-e). For all the other DEMs, no deformation pattern is discerned in the selected PS-pixels (Fig. 3.6 a-c). To validate the local deformation, we compare our PS-results to independent observations. The simplified landslide perimeter shown in the detailed map (Fig. 3.6 e) was compiled from a regional inventory (SERVIZIO GEOLOGICO, SISMICO E DEI SUOLI DELLA REGIONE EMILIA-ROMAGNA, 2014). Several reference points were selected in rural areas where vegetation is sparse. While the points on the ridges outside the landslide perimeter can be considered stable (green dots in Fig. 3.6 e), the mean velocities of the PS pixels in the source area (red dots) in-

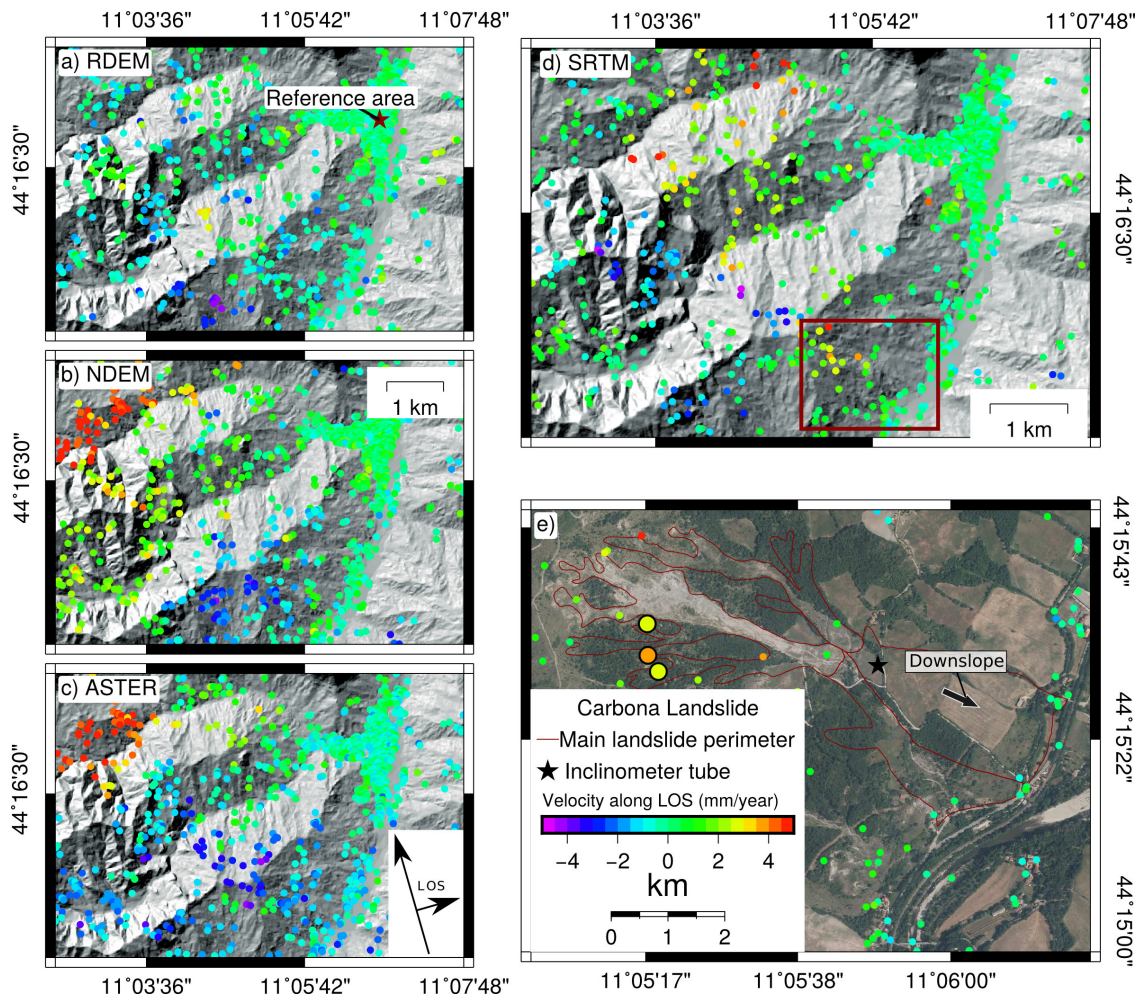


**Figure 3.6:** Left column (a-c): PS-results for the regional, the national and ASTER DEMs. Right column (d-e): PS-results for the 30 m resolution SRTM DEM. For all cases the same reference area has been used, as indicated by the star in (a). The mean velocities differ significantly on a regional scale, but show reasonable agreement locally. The highlighted deformation pattern (red box) appears only if SRTM is used. It corresponds to an active landslide that is represented by the dark red lines in e). The time series of the highlighted PS-pixels (big points with black margin) and the inclinometer measurements are reported in fig. 3.7.

indicate a movement away from the satellite along the line-of-sight, consistent with downslope movement of the ground.

In 2004, an inclinometer tube was installed in the central part of the landslide body (Fig. 3.6 e). The deformation profiles of the inclinometer measurements suggest that the active slip surface is at ca. 10 m depth (Fig. 3.7 a, b). The time series for the PS-pixels located in the source area of the landslide show an acceleration after

2006 and a deceleration after 2008 (Fig. 3.7 c). A projection of the inclinometer readings into the line-of-sight yields a displacement of approximately 20 mm for the period that the PS time series and the inclinometer measurements have in common. It should be noted that the position of the inclinometer is situated in the transport zone while the PS-pixels are in the source area, and the inclinometer measures movement at depth while the PS signal is at the surface. Nevertheless, we consider both measurements to be consistent within the common time period of observation.

It appears that only SRTM delivered a reasonable InSAR signal. The spatial pattern does not cross the ridges and the river valley and it is located inside a earthflow complex which is mapped as active by the regional inventory. Although the mean velocities are relatively low (4-5 mm/a), a careful analysis of the time series of all pixels that are located inside the landslide perimeter (Appendix A), suggests that the results derived from the other datasets contain high frequency scatter in time, which we interpret as noise. This high frequency scatter is almost absent for SRTM and the time series in Fig. 3.7 c show that the mean velocities between 2006 and 2008 (ca. 15 mm/a) are well beyond the noise level. For the results using ASTER DEM, it appears that the scatter is correlated with the perpendicular baselines in time and hence it is likely caused by local inaccuracies in the DEM. An analysis of the residual heights around the area of interest shows that the DEMs deviate up to 10 m from the mean. However this is also the case in areas like Gaggio Montano (Fig. 3.5 e-f) where we obtained consistent results.

#### **3.4.3 Lama Mocogno: An example of local differences in SB-results with Cosmo-SkyMed**

The small town of Lama Mocogno is located ca. 40 km S of Modena. Here, fine grained turbiditic deposits of the Monte Venere Formation constitute the substratum (BETTELLI et al., 2002) and the landslide material is characterized by higher mechanical resistance when compared to the clay-shales of Carbona. The landslide complex shown in Fig. 3.8 is composed of several nested landslides and spans almost the entire slope South of Lama Mocogno. Sparse houses identify the localities La Borra and Vaglio. Five inclinometers were installed in the late 1990s on the northern margin of the landslide (Vaglio). Those inclinometers measured a small, yet constant deformation with a relative continuous vertical displacement profile and no

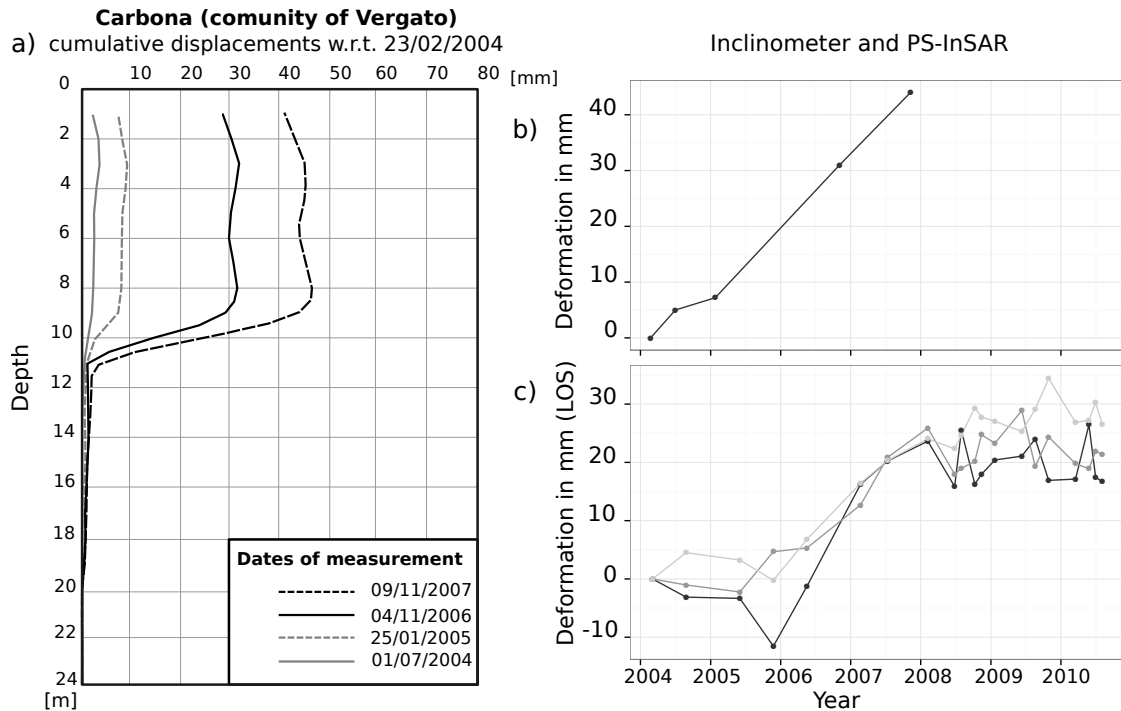


**Figure 3.7:** a) Inclinometer readings for the period between 2004 and 2007 at the Carbona landslide. b) Inclinometer timeseries in the transport zone and (c) time series of the PS-pixels from the source zone shown in the map of Fig.3.6 e). The PS time series show an acceleration of the slide in 2005 whereas the inclinometer reports a steady deformation in time. The displacement measured by the inclinometer is directed approximately downslope while the InSAR displacements are reported in movement along the line-of-sight of the satellite.

distinct slip surface (Fig. 3.9 a). One possible explanation is that the slip surface is actually deeper than the borehole, and hence only a continuous tilt is measured. During March of 2013, a series of intense precipitation events struck the region of Emilia Romagna and reactivated numerous landslides (PIZZIOLO et al., 2013). In the course of these events the southern part of the landslide complex started to move, causing severe damage to houses and infrastructure. The reactivation is highlighted in Fig. 3.8 as red polygon, which we refer to as the Borra landslide. In the aftermath of this reactivation three inclinometers were installed on the central part of the landslide and a clean measurement of one inclinometer tube is reported in Fig. 3.9 b. The inclinometer data suggests the presence of a slip surface at a depth of ca. 24 meters and a relative steady displacement for the period between September 2013 and May 2014 reaching an absolute deformation of ca. 10 mm directed approximately downslope.

### 3 Influence of digital elevation models on InSAR results

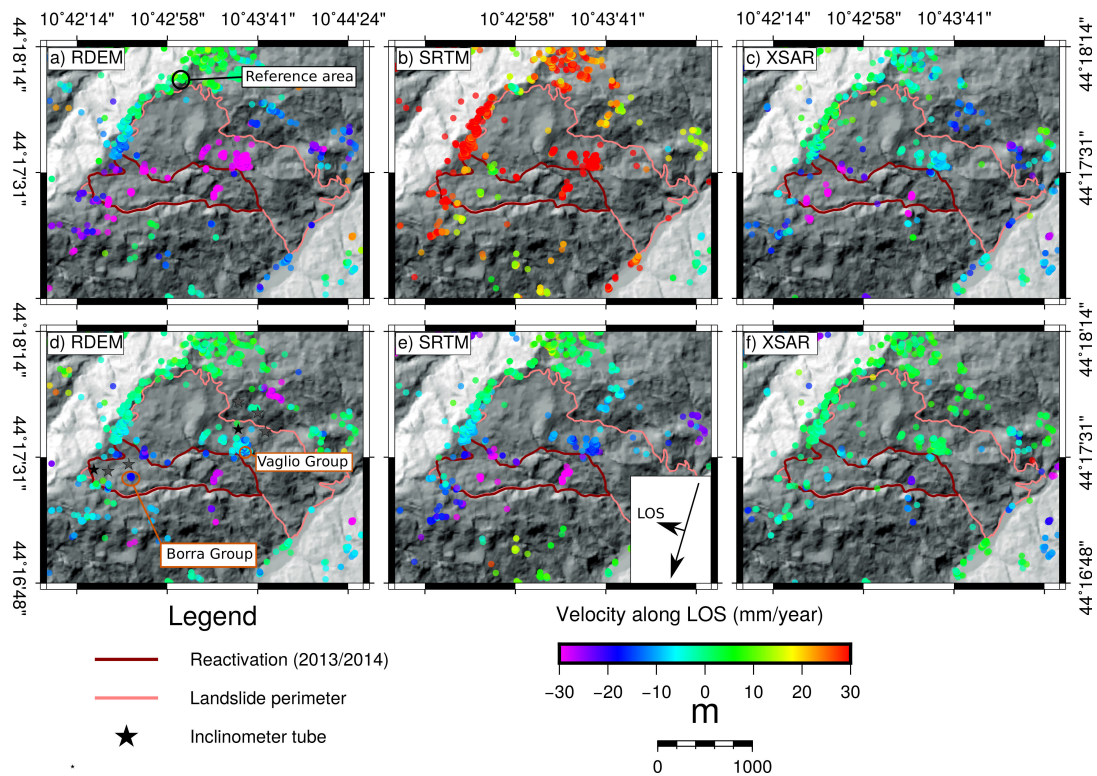


**Figure 3.8:** Top row (a-c): SB-results at the localities Borra and Vaglio (municipality of Lama Mocogno) after an initial run of StaMPS. The reference area is set with respect to a group of houses on a crest that is deemed to be relatively stable. While the results using a) RDEM and c) XSAR indicate a range decrease, a range increase is inferred, using SRTM. In all cases the time series were characterized by a significant amount of high frequency scatter. Bottom row (d-f): SB-results after the estimation of spatially correlated look angle error and iterative unwrapping. In all cases the high degree of noise was reduced and the results become consistent. However with d) RDEM and e) SRTM displacements were also measured in the Vaglio area contrary to f) XSAR.

The SB-pixels that were selected for the various DEMs show different displacement maps even though a consistent reference area is selected (Fig. 3.8 a - c). Again different numbers of points are selected and also the position of the pixels vary if different DEMs are used. Inside the large landslide complex StaMPS selected 432 points for RDEM, 339 pixels for SRTM and 273 points for XSAR. Inside the reactivated zone 87 points were registered for SRTM, 78 for RDEM and 69 for XSAR. Here the common SBAS-pixels correspond usually to groups of houses. These differences show that the number of pixels is a problematic measure for DEM-quality when examined in a limited area, and a careful analysis of the InSAR results over a broader region is necessary to evaluate which signal is the most reliable.

After an initial execution of the processing chain, including unwrapping and DEM error estimation, large differences can be observed for the different DEMs (Fig. 3.8 a-c). For SRTM, phase jumps occur in the direct vicinity of the reference area and cause a signal of opposite sign compared to the results obtained for the other DEMs. We attribute these differences again to problems during the unwrapping procedure in combination with an incorrect estimate of the DEM error. Ducret et al. (DUCRET et al., 2014) found that unwrapping results improve if the DEM error is estimated from the wrapped phase and subtracted before unwrapping. In addition, it is possible to run the unwrapping-, and the spatially correlated DEM error estimation, in an iterative way, by subtracting the DEM error estimate before each new unwrapping procedure and adding back afterwards. This procedure eliminates noise in the interferograms and resolves most unwrapping problems. The second row of Fig. 3.8 shows the deformation maps obtained by this method. Many differences vanish and the results obtained by RDEM and SRTM begin to converge. Also for XSAR a similar displacement is detected, although it is not as clear and intense as for RDEM and SRTM. The measured displacements indicate a range decrease, which, in accordance with the inclinometer data, can be interpreted as a downslope displacement.

The SB time series of the displacements show also after the iterative unwrapping procedure notable differences. Fig. 3.9 c shows the mean of the group of pixels located on the Borra landslide, which we refer to as the Borra group (Fig. 3.8 c). Clear displacements show up for RDEM and SRTM, while for XSAR the time series do not suggest any deformation. The time series obtained by SRTM show two accelerations, one during spring 2013 and a second during late summer/autumn. The first acceleration spans four time steps and is also recorded for RDEM. The second acceleration spans only one timestep and is obscured in the RDEM time series by a range increase in the preceding timestep. Both periods of intense displacement are associated with periods of large perpendicular baselines in the dataset (Fig. 3.2 b). However, an analysis of single interferograms that cover the periods in question suggest that the signal from the SRTM product is real. It should be noted however that StaMPS uses an unwrapping algorithm that works in time and space (HOOPER & ZEBKER, 2007). While this algorithm generally improves the quality of the unwrapped solution, a baseline-controlled DEM error cannot be excluded.

The time series that were measured using different DEMs on a group of pixels on the Vaglio landslide (referred to as Vaglio group in Fig. 3.8 c) are plotted in Fig. 3.9 d. Here the deformation maps suggest a displacement only for SRTM and RDEM. The time series are difficult to interpret because of high frequency scatter. Displacements of approximately 10 mm along the line of sight for the period between October 2012 and January 2014 are reasonable when compared to inclinometer readings that indicate displacements up to 9 mm for the period between March 1999 and March 2001. A projection of these displacements into the line of sight correspond to 3.3 mm/a which are slightly lower than the InSAR derived measurements (6 mm/a). Considering the uncertainties associated with the inclinometer and the different time frame, we think that both measurements are consistent with sustained slow movement.

An analysis of the SB time series for the Borra group is reported in the Appendix A. The time series show that the SRTM product contains the lowest degree of high frequency scatter compared to the time series obtained by the other DEMs. Moreover it appears that the DEM error estimation strategy in the time domain slightly overestimates the phase term due to the DEM error. We believe that the reason for this is the low number of timesteps/scenes (23) compared to the high number of interferograms (64) that span the parameter space of the error-estimate.

## 3.5 Discussion and concluding remarks

Because of non-zero perpendicular baseline between SAR acquisitions, DEMs are necessary for removing the topographic fringes from interferograms and revealing line-of-sight changes related to surface deformation. In this work, we have explored how InSAR results vary depending on the choice of the DEM. In the Northern Apennines of Italy, several DEMs are available, thereby allowing for a systematic evaluation. We statistically compared the differences in height of multiple DEMs. The statistical analysis of the residual heights in geographic and radar-coordinates can help to identify systematic errors in the DEMs. Large errors were identified in XSAR due to the sparse coverage and the acquisition geometry. Additionally, large local errors were identified in the national DEM (NDEM), while the other elevation

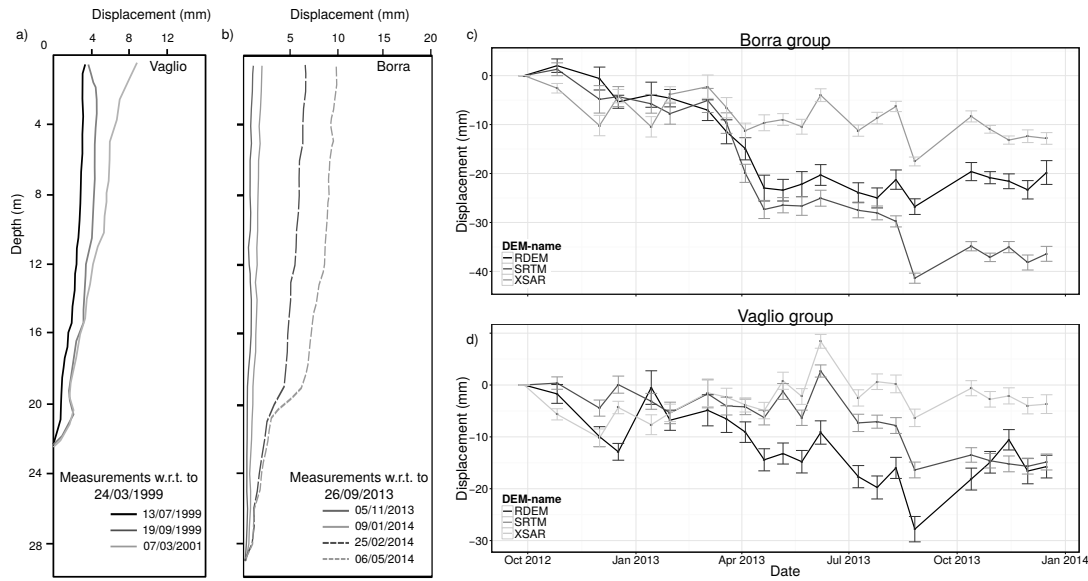


**Figure 3.9:** a) Inclinometer measurements from the Vaglio inclinometer tube (black star in Fig. 3.8 d). Although the vertical displacement profile is rather spatially continuous, we believe that the deformation at the top of the inclinometer are real. b) Inclinometer measurements at the locality Borra (black star in vicinity of the Borra Group in Fig. 3.8 d). A distinct slip surface is present at a depth of approximately 20 meters and displacements up to 10 mm were measured for the period between September 2013 and May 2014. c) Average of the cumulative displacements of all pixels located in the Borra Group (see Fig. 3.8 d) obtained for different elevation models. Only RDEM and SRTM show a clear acceleration signal during the spring of 2013 and only SRTM resolves a second acceleration during late summer 2013 is visible. d) Time series of the average cumulative deformation for all pixels located in the Vaglio group (Fig. 3.8 d) obtained with different DEMs. Only the time series obtained using SRTM and RDEM measured a steady displacement, while the timeseries from XSAR have no slope.

datasets presented no systematic errors. Many of these problems are mitigated when the DEMs are resampled and converted to radar coordinates.

InSAR stacks of both the Envisat and Cosmo-SkyMed interferograms show consistent results when the various DEMs are used. Thus, the choice of DEM has minimal impact on individual wrapped differential interferograms. The regional line-of-sight velocities showed considerable spatial variability when using different DEMs with the PS- and SB- implementation of StaMPS. Both the synthetic error analysis (see Fig. 3.4 h-k) and the statistical results in Tab. 3.1 suggest a relationship between the RMSE of the various residuals and the DEM error and the registered number of PS/SB-pixels. The X-band data appeared more sensitive to small DEM-errors, likely because of the large perpendicular baselines of the dataset and due to the short wavelength. The number of selected points vary about 3% from Envisat and

6 % for Cosmo-SkyMed, depending on which DEM is used. However, in general the 30 m SRTM DEM provided a high number of PS-, and SB-pixel for both Satellites. Inaccurate DEMs can reduce the number of selected pixels and as a consequence, a signal might not be visible. A low density of PS or SB-pixels can also introduce phase-jumps during unwrapping, which in our view produced the patch-like results in Fig. 3.5 and 3.8. Although a higher number of points were registered for Cosmo-SkyMed using the regional DEM (RDEM), there is no clear evidence that it significantly improved the results in terms of signal quality.

We documented localized differences on two landslide cases that illustrate how DEM inaccuracies can cause a signal loss, because the phase in time is dominated by a scatter that correlates with the baseline history (see also FATTAHI & AMELUNG, 2013 and Appendix A). This might lead ultimately also to the rejection of certain points by the PS/SB-pixel selection routines in StaMPS. Our inferences are likely applicable to other implementations of PS and SBAS, given that the underlying approaches are similar. The dependence of the results on different DEMs is largely dictated by varying attributed of the DEMs, including whether the DEM accurately reflects the morphology at the time of the SAR acquisitions. The results obtained with XSAR at Lama Mocogno suggest that errors due to the acquisition mode of the elevation data are also important. The example of Gaggio Montano showed that local differences can be resolved if stable reference pixels are selected close to the area of interest. In the case of SB-processing, the results became more consistent if DEM error estimation and unwrapping are executed in an iterative way.

In conclusion, it can be stated that the influence of the DEM on PS- and SB-processing is complex. Few significant statistical differences appear in the DEMs and the wrapped interferograms. In particular, the identification of local inaccuracies in digital elevation models, and hence the evaluation of DEM quality relevant for InSAR purposes before the actual processing, is difficult. Nevertheless, significant differences are observed in the post-processed deformation maps, most of which are related to pixel selection and unwrapping problems. The local examples at Carbona and Lama Mocogno show that the influence of the DEM is quite important and an inaccurate DEM can lead to a signal in time that correlates with the baseline history. This effect depends not only on the quality of the DEM, but also on the wavelength of the satellite and the baseline history in an InSAR dataset. A large variance in the perpendicular baselines and the baseline history should theoretically improve

the quality of the DEM error estimate. A high number of SAR acquisitions and a high number of interferograms should also improve the estimate for the topographic error term. In contrast, datasets with a low variance in perpendicular baselines (e.g. drifting baselines) or few observations would reduce the quality of this estimate. Since SRTM delivered in all cases the most reliable results, it is important in our view that the DEM reports the topography as the radar satellite would see it. Hence the DEM should contain the heights of the houses, structures, and vegetation as imaged by the SAR data. Even though high resolution elevation data from LiDAR was not available for our area, it would be interesting to see how a modern digital elevation model might perform. The SB-results obtained using XSAR indicate that there is not necessarily a benefit if the DEM has been acquired by a radar with the same wavelength.

### **3.6 Time series analysis of Carbona and Lama Mocogno**

InSAR results can differ locally if different DEMs are used to correct the interferograms for the topographic phase term. In order to explain the reason for these differences we analyse the time series of selected PS-and SBAS pixels that were selected by StaMPS with respect to the two local examples of Carbona (Envisat) and Lama Mocogno (Cosmo SkyMed). At Carbona the expected deformation signal was only detected when SRTM was used. Fig. 3.10 shows the time series of the unwrapped phase and different error estimates (converted into displacement) along the line-of-sight. The uncorrected phase of the pixels that StaMPS selects for SRTM are characterized by a lower degree of noise. As a result the DEM error estimate is also smaller than the remaining phase term. The spatially correlated noise estimate, which is expected to remove the atmospheric noise, seems also to remove parts of the phase that correlates with the perpendicular baseline. The resulting time series for SRTM are more consistent in that the PS-pixels inside the landslide bodies show similar displacements and contain less scatter compared to the time series of the other datasets. Even though this scatter is not present in the corrected time series, the absence of the expected deformation signal and the general high noise level in the

### 3 Influence of digital elevation models on InSAR results

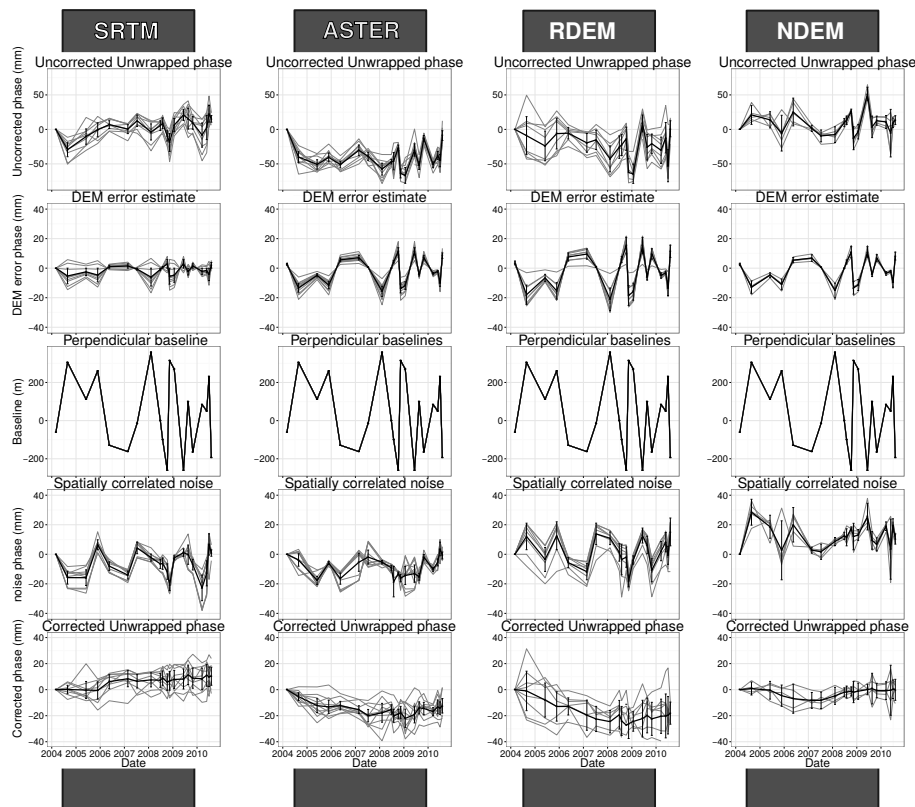


**Figure 3.10:** Time series of all pixels located inside the Carbona landslide. First row: uncorrected unwrapped phase; second row: DEM error estimate; third row: Perpendicular baselines; fourth row: Spatially correlated noise; last row: The corrected phase is obtained by subtracting the two error estimates from row two and four from the uncorrected phase in the first row.

uncorrected time series suggest that phase terms due to local DEM errors obscured the deformation signal, when the other DEMs were used.

Significant differences were also observed at Lama Mocogno, and a careful analysis of the time series located on the Borra landslide helped to identify the main reasons for this. In Fig.3.11 the time series of the pixels located on the Borra landslide are plotted together with the perpendicular baselines and the two DEM correction strategies. We chose these pixels because they represent the same physical objects on the ground and the deformation history of the landslide was known in advance. The first row shows the uncorrected time series. Only RDEM and SRTM registered the expected deformation signal, while the time series using XSAR contain a strong signal that correlates with the baseline. The second row shows the time series of the DEM error that was estimated on the inverted interferograms (as described in

FATTAHI & AMELUNG, 2013) while the third row shows the DEM error time series that were calculated in the interferogram domain. It appears that for our baseline network and the given interferograms, the time domain strategy estimates higher values, while the corrections in the interferogram domain are smaller. The fourth row shows the baseline history of our Cosmo SkyMed dataset. Note that there are jumps in baseline history in spring and late summer/autumn 2013. An incorrect estimate of the DEM error could introduce an artefact during these periods, particularly if the unwrapping process and the DEM error estimate is run iteratively. This is also the reason why it is difficult to tell if the two periods of acceleration visible in the time series of SRTM are a true signal or if they are a result of false DEM error estimates that are propagated via the unwrapping in time in the adjacent time steps. The two different DEM error correction strategies yield slightly different results. The mean velocity estimates are, as expected, not affected by this differences; the shapes of the time series differ. It appears that the correction in the time domain over-estimates the DEM error, which results in a slightly larger scatter in the time series. The time series that were corrected in the interferogram domain are smoother and also the variances between the single time series become smaller.

## Acknowledgments

The Digital elevation models ASTER and SRTM at 1 arcsecond have been downloaded from the USGS earth-explorer <http://eros.usgs.gov/>. The Cosmo-SkyMed data has been kindly provided by the Italian Space Agency (AGI) and Envisat have been distributed by the European Space Agency. The Region of Emilia Romagna provided the RDEM and the inclinometer data. We would like to thank three anonymous reviewers for useful comments and suggestions.

## 3.7 References

BERARDINO, P., FORNARO, G., LANARI, R. & SANSOSTI, E. (2002): A new algorithm for surface deformation monitoring based on small baseline differential SAR interferograms. – *Ieee Transactions On Geoscience and Remote Sensing*, **40** (11), pp. 2375–2383; New York.

### 3 Influence of digital elevation models on InSAR results

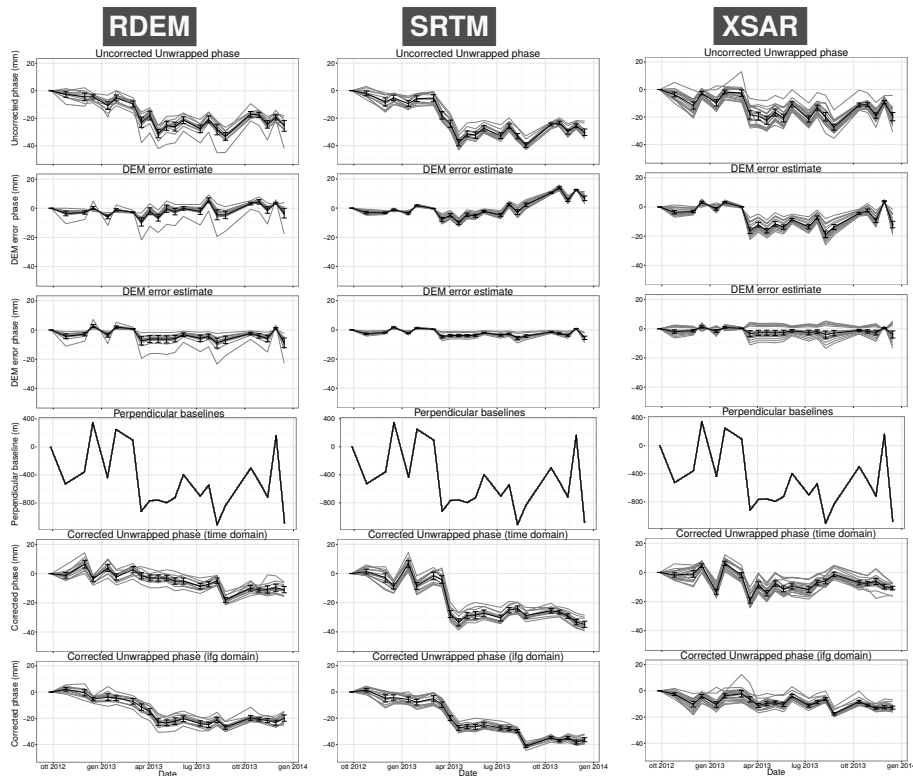


**Figure 3.11:** Time series of all pixels located inside the Borra landslide. First row: uncorrected unwrapped phase; second row: DEM error estimate obtained in the interferogram domain; third row: DEM error estimate obtained in the time domain; fourth row: Perpendicular baselines; fifth row: Unwrapped phase, corrected by the DEM error in the time domain (first row minus the third row). Unwrapped phase, corrected by the DEM error in the interferogram domain (first row minus the second row).

BERTI, M. & SIMONI, A. (2010): Field evidence of pore pressure diffusion in clayey soils prone to landsliding. – *Journal of Geophysical Research*, **115** (F3), F03001, 1–20; Washington DC.

BETTELLI, G., PANINI, F. & PIZZOLO, M. [eds.] (2002): Note illustrative della Carta geologica d'Italia alla scale 1:50.000, foglio 236 Pavullo nel Frignano. –; Firenze (Servizio Geologico d'Italia).

COLESANTI, C. & WASOWSKI, J. (2006): Investigating landslides with space-borne synthetic aperture radar (SAR) interferometry. – *Engineering Geology*, **88** (3-4), pp. 173–199; Amsterdam.

- CORSINI, A., FARINA, P., ANTONELLO, G., BARBIERI, M., CASAGLI, N., COREN, F., GUERRI, L., RONCHETTI, F., STERZAI, P. & TARCHI, D. (2006): Space-borne and ground-based SAR interferometry as tools for landslide hazard management in civil protection. – *International Journal of Remote Sensing*, **27** (12), pp. 2351–2369; London.
- CRUDEN, D. M. & VARNES, D. J. (1996): Landslide types and processes. – In: TURNER A. K. & Schuster, R. L. [ed.] (1996): *Landslides: investigation and mitigation*, special report 247, pp. 36–75; Washington DC (Transportation Research Board, National Research Council).
- DAEHNE, A. (2014): Innovative techniques for hazard analysis in slow-moving active earthslides-earthflows: Applications to the valoria landslide (Northern Apennines, Italy). – PhD Thesis, Università degli studi di Modena e Reggio Emilia – Dipartimento di scienze della terra, 199 pp.; Ph.D. dissertation, Department of earth sciences, University of Modena and Reggio Emilia.
- DUCRET, G., DOIN, M.-P., GRANDIN, R., LASSERRE, C. & GUILLASO, S. (2014): DEM Corrections Before Unwrapping in a Small Baseline Strategy for InSAR Time Series Analysis. – *Ieee Geoscience and Remote Sensing Letters*, **11** (3), pp. 696–700;
- ECKERT, S., KELLENBERGER, T. & ITTEN, K. (2005): Accuracy assessment of automatically derived digital elevation models from aster data in mountainous terrain. – *International Journal of Remote Sensing*, **26** (9), pp. 1943–1957;
- FATTAHI, H. & AMELUNG, F. (2013): DEM Error Correction in InSAR Time Series. – *Ieee Transactions On Geoscience and Remote Sensing*, **51** (7), pp. 4249–4259;
- FERRETTI, A., PRATI, C. & ROCCA, F. (2001): Permanent scatterers in SAR interferometry. – *Ieee Transactions On Geoscience and Remote Sensing*, **39** (1), pp. 8–20; New York.
- HANSSEN, R. F. (2001): *Radar interferometry: data interpretation and error analysis*. – 308 pp.; New York, Boston, Dordrecht, London, Moscow (Kluwer Academic Publishers).

- HOFFMANN, J. & WALTER, D. (2006): How complementary are SRTM-X and -C band digital elevation models? – *Photogrammetric Engineering and Remote Sensing*, **72** (3), pp. 261–268;
- HOOPER, A., SEGALL, P. & ZEBKER, H. (2007): Persistent scatterer interferometric synthetic aperture radar for crustal deformation analysis, with application to Volcan Alcedo, Galapagos. – *Journal of Geophysical Research-solid Earth*, **112** (B7), B07407; Washington DC.
- HOOPER, A. (2008): A multi-temporal InSAR method incorporating both persistent scatterer and small baseline approaches. – *Geophysical Research Letters*, **35** (16), p. L16302; Washington DC.
- HOOPER, A. & ZEBKER, H. A. (2007): Phase unwrapping in three dimensions with application to InSAR time series. – *Journal of the Optical Society of America A-optics Image Science and Vision*, **24** (9), pp. 2737–2747;
- KAMPES, B. & USAI, S. (1999): “Doris: The delft object-oriented radar interferometric software” In: 2nd International Symposium on Operationalization of Remote Sensing, Enschede, The Netherlands vol. 16 Citeseer, 1999, p. 20.
- KOLECKA, N. & KOZAK, J. (2014): Assessment of the Accuracy of SRTM C- and X-Band High Mountain Elevation Data: a Case Study of the Polish Tatra Mountains. – *Pure and Applied Geophysics*, **171** (6), pp. 897–912;
- MASSONNET, D. & FEIGL, K. L. (1998): Radar interferometry and its application to changes in the earth’s surface. – *Reviews of Geophysics*, **36** (4), pp. 441–500;
- PANINI, F., BETTELLI, G. & PIZZIOLLO, M. [eds.] (2002): Note illustrative della carta geologica d’Italia alla scala 1:50.000: Foglio 237, Sasso Marconi. – 176 pp.; Firenze (S.EL.CA. s.r.l).
- PINI, G. A. (1999): Tectonosomes and olistostromes in the argille scagliose of the Northern Apennines, Italy. – *Special Paper - Geological Society of America*, **335** (1), pp. 1–70; Boulder.
- PIZZIOLO, M., MONNI, A. & PRIMERANO, S. (2013): Con le piogge anomale frane da record. – *Ecoscienza*, **2013** (2), pp. 12–14; Bologna.

- RABUS, B., EINEDER, M., ROTH, A. & BAMLER, R. (2003): The shuttle radar topography mission - a new class of digital elevation models acquired by spaceborne radar. – *Isprs Journal of Photogrammetry and Remote Sensing*, **57** (4), pp. 241–262;
- RODRIGUEZ, E., MORRIS, C. S. & BELZ, J. E. (2006): A global assessment of the SRTM performance. – *Photogrammetric Engineering and Remote Sensing*, **72** (3), pp. 249–260;
- ROSEN, P. A., HENSLEY, S., JOUGHIN, I. R., LI, F. K., MADSEN, S. N., RODRIGUEZ, E. & GOLDSTEIN, R. M. (2000): Synthetic aperture radar interferometry - Invited paper. – *Proceedings of the Ieee*, **88** (3), pp. 333–382; New York.
- ROSEN, P. A., HENSLEY, S., PELTZER, G. & SIMONS, M. (2004): Updated repeat orbit interferometry package released. – *Eos Trans. AGU*, **85** (5), pp. 47–47; Malden.
- SAMSONOV, S. (2010): Topographic Correction for ALOS PALSAR Interferometry. – *Ieee Transactions On Geoscience and Remote Sensing*, **48** (7), pp. 3020–3027;
- SCHMIDT, D. A. & BÜRGMANN, R. (2003): Time-dependent land uplift and subsidence in the Santa Clara valley, California, from a large interferometric synthetic aperture radar data set. – *J. Geophys. Res.* **108** (B9), pp. 1–13; International.
- SERVIZIO GEOLOGICO, SISMICO E DEI SUOLI DELLA REGIONE EMILIA-ROMAGNA (2014): Carta Inventario delle frane a scala 1:10000 della Regione Emilia-Romagna. URL: <http://ambiente.regione.emilia-romagna.it/geologia/cartografia/webgis-banchedati/cartografia-dissesto-idrogeologico>; –.
- SIMONI, A., PONZA, A., PICOTTI, V., BERTI, M. & DINELLI, E. (2013): Earth-flow sediment production and Holocene sediment record in a large Apennine catchment. – *Geomorphology*, **188** (1), pp. 42–53; Amsterdam.
- SUN, Q., ZHANG, L., HU, J., DING, X. L., LI, Z. W. & ZHU, J. J. (2015): Characterizing sudden geo-hazards in mountainous areas by D-InSAR with an enhancement of topographic error correction. – *Natural Hazards*, **75** (3), pp. 2343–2356;

- TANTIANUPARP, P., BALZ, T., WANG, T., JIANG, H., ZHANG, L. & LIAO, M. (2012): Analyzing the Topographic Influence For the Ps-insar Processing In the Three Gorges Region. – In: Analyzing the Topographic Influence For the Ps-insar Processing In the Three Gorges Region (2012): 2012 Ieee International Geoscience and Remote Sensing Symposium (igarss) Munich, pp. 3843–3846; New York (IEEE).
- VAJEDIAN, S., MOTAGH, M. & NILFOUROUSHAN, F. (2015): StaMPS Improvement for Deformation Analysis in Mountainous Regions: Implications for the Damavand Volcano and Mosha Fault in Alborz. – Remote Sensing, **7** (7), pp. 8323–8347;
- WELCH, R., JORDAN, T., LANG, H. & MURAKAMI, H. (1998): ASTER as a source for topographic data in the late 1990's. – Ieee Transactions On Geoscience and Remote Sensing, **36** (4), pp. 1282–1289;

# **4 Ground surface deformations induced by tunneling under deep-seated landslides in the Northern Apennines of Italy imaged using advanced InSAR techniques.**

**Authors:** Benedikt Bayer, Alessandro Simoni, Lara Bertello and David Schmidt

**Publication details:** Accepted for publication in Engineering Geology

### **Abstract**

Synthetic Aperture Radar (SAR) interferometry (InSAR) is used to make measurements of small surface displacements in different situations including ground-settlement, landslides and excavations. We document the deformation history of four dormant deep-seated landslides in the Northern Apennines of Italy that were reactivated by the excavation of a double road tunnel. The tunnel is part of a larger infrastructure project that involves the improvement of the A1 highway which connects Bologna and Florence. The excavation of the tunnel under the landslides' basal shear surfaces started in 2011, and with the advance of the tunnel front, deformation began to occur, causing damages to homes and infrastructures. The tunnel passes under the small villages of Ripoli and Santa Maria Maddalena. The deformation slowed down after the tunnel was completed in November 2014, and low surface displacement rates were registered for the period between October 2014 and June 2016. We show the results of an InSAR analysis designed to measure surface movements between 2003 and 2016. The InSAR displacements are derived from the Envisat, COSMO SkyMed, and Sentinel 1 datasets and cover the main construction phase of the tunnel (2011-2015). A detailed geological and geomorphological mapping of the slope is developed based on the field evidence and on the spatial pattern of surface deformation provided by our InSAR analysis. Together with the map, a new conceptual geological model of the slope in tectonically sheared and weathered flysch is presented. The satellite InSAR data show good agreement with available ground based monitoring data that include inclinometer and GPS-measurements, while small differences occur with respect to deformation time series obtained from a ground-based InSAR instrument. In particular, the InSAR results for the X-Band data of COSMO SkyMed demonstrate the close relationship between the position of the excavation front and the displacement rates of previously dormant landslide deposits. Conversely, the concurrent rainfall does not appear to significantly influence the observed behaviour and, if any, had only a minor influence on the displacement history of the investigated landslides.

## 4.1 Introduction

Synthetic aperture radar (SAR) interferometry (InSAR) is a remote sensing technique capable of measuring millimeter-to-decimeter displacements of the earth surface. It has been successfully used to assess subsidence (SCHMIDT & BÜRGMANN, 2003), volcanic inflation or deflation (HOOPER et al., 2004) and the deformation field of earthquakes (BÜRGMANN et al., 2000; FIALKO et al., 2001). But it has also been applied to the deformation caused by landsliding (COLESANTI & WASOWSKI, 2006; HANDWERGER et al., 2013), as well as subsurface excavation and tunneling (PARCHARIDIS et al., 2006; MARK et al., 2012).

The excavation of a tunnel in mechanically weak sedimentary rocks, like flysch or *mélange* type rocks (MARINOS & HOEK, 2001) can be problematic (KONTOGIANNI et al., 2004). When the excavation is performed in a slope subject to gravitational instability, the stress redistribution induced by tunneling can reactivate or accelerate pre-existing landslides. SPAUN (1979) discusses several historical cases, where deep seated landslides were not correctly identified and caused severe damages during tunneling (Eisenhower Memorial tunnel, Denver USA), or the original tunnel even had to be abandoned after completion due to persisting deformations and failure of the tunnel frame (Frejus railway tunnel, Italian and French Alps). If excavation took place inside the landslide material or in a creeping rock mass, high deformation rates were documented on the tunnel lining, that were highest with respect to transition between landslide and bedrock (SPAUN, 1979; BOLDINI et al., 2004). When excavating inside a landslide, the material is looser with respect to the bedrock, which requires additional stabilization measures (ADAM et al., 2014), but may also permit higher excavation rates (THURO et al., 2001).

While effects of slope deformations on tunnel projects are frequently described in the literature, works that focus in detail on geomorphological aspects or report the spatio-temporal displacement patterns that a tunnel excavation induces on landslides are rare. GRIFFITHS et al. (1995) presented a detailed geomorphological model of the landslides on the British side of the channel tunnel and highlighted the importance of detailed reconnaissance maps during planning and construction phases. Ground based InSAR measurements were used in the past to measure and analyze landslide displacement (BOZZANO et al., 2011) and to backmodel partial failures of a slope affected by tunneling (BOZZANO et al., 2014; MAZZANTI et al., 2015).

NOFERINI et al. (2007) used a Ground based InSAR, GPS and inclinometers to measure the steady deformation of a deep seated rockslide over a tunnel in the Carnian Alps of Northern Italy, which resulted in a closure of this tunnel. ADAM et al. (2014) described tunneling induced deformation of a rockslide in *mélange* type rocks. They showed that landslide motion varied according to the excavation modality of the tunnel.

The San Benedetto tunnel is a section of the highway project "Variante di Valico" in the Northern Apennines of Italy and is located approximately 50 km south of Bologna and 10 km south-east of Vergato (Fig. 5.1). It passes under the small villages of Ripoli and Santa Maria Maddalena as well as under several sparse groups of houses. Soon after the beginning of the excavation in 2010, the movement of old dormant landslides caused moderate to severe damage to the houses of the aforementioned villages. Different parts of the present slope were studied and described from an engineering perspective by different groups of authors (BANDINI et al., 2015; BARLA et al., 2015; BARLA et al., 2016; D'EFFREMO et al., 2016).

The case of Santa Maria Maddalena and Ripoli is interesting for several reasons. Since both villages were exposed to high risk, the slope was instrumented, and the tunnel contractor published deformation data on a designated observatory homepage ([www-01](http://www-01)). This deformation data include inclinometer and piezometer readings. Furthermore, the Emilia Romagna Region performed periodic GPS campaigns and a terrestrial interferometry survey. The presence of two villages and several sparse groups of houses, in combination with small ground displacements that extend over a large area, makes this case also suitable for a space born InSAR survey. The high quality of the InSAR signal and the presence of independent ground truth data allowed us to compare the deformation data from different monitoring instruments. We document the InSAR results obtained with the Stanford Method of Persistent Scatterers (StaMPS HOOPER et al., 2007) for SAR data from Envisat, COSMO SkyMed, and Sentinel 1A missions. Based on detailed field survey, we produce a geomorphological map that keeps into account monitoring results and is further enhanced by geophysical investigations that include the analysis of Horizontal to Vertical Spectral Ratio of ambient seismic noise (HVSr in the following) and Multichannel Analysis of Surface Waves (MASW in the following). Based on the mapping and the InSAR derived deformations, we propose a detailed geological/ge-

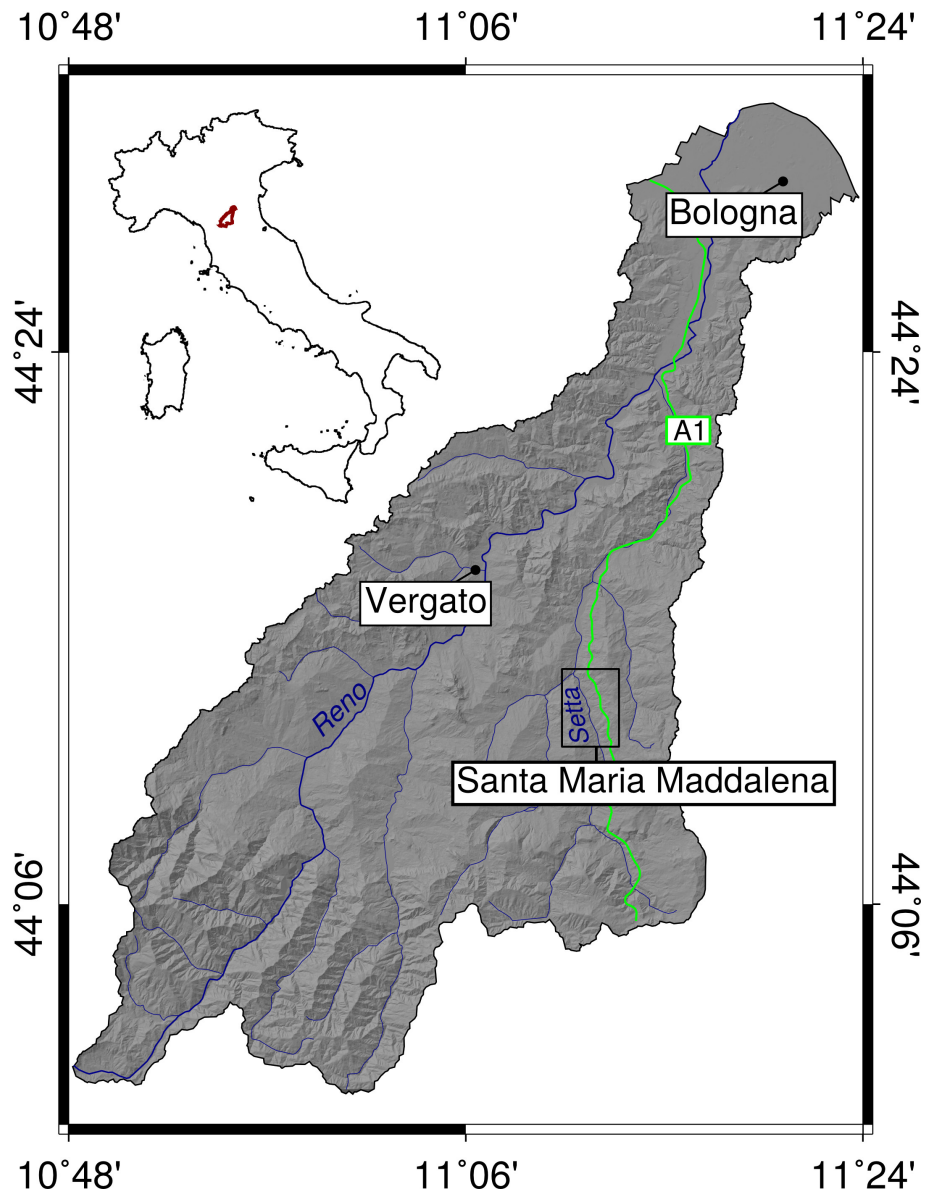


*Figure 4.1: The San Benedetto Val di Sambro tunnel is part of the highway project "Variante di Valico" and is located ca. 50 km South of Bologna. The tunnel passes under the villages of Ripoli and Santa Maria Maddalena.*

omorphological model of the slope and document the spatio-temporal development of landslide motion in relation to underground excavation.

**Table 4.1:** Main characteristics of the InSAR datasets that were used in the present work. No. of Ifgs are the number interferograms and  $B_{perp}$  range is the range of perpendicular baselines in the InSAR datasets

Satellite	Direction	Orbit	No. of scenes	No. of Ifgs	Period	$B_{perp}$ range
Envisat	ascending	444	40	56	16.10.'03 – 05.08.'10	-263 to +310
Envisat	descending	165	31	63	27.09.'03 – 21.08.'10	-291 to +289
CSK	ascending	26550	34	60	25.12.'09 – 24.01.'15	-563 to +561
CSK	descending	29090	16	29	31.01.'13 – 22.02.'15	-773 to +436
Sentinel 1A	ascending	117	41	115	13.10.'14 – 04.06.'16	-163 to 181
Sentinel 1A	descending	168	26	72	22.03.'15 – 15.05.'16	-126 to 137

## 4.2 Materials and Methods

### 4.2.1 InSAR processing

Different InSAR techniques were used in the past to retrieve spatial and temporal deformation of slow slope deformations (ROERING et al., 2009; BOVENGA et al., 2012; HANDWERGER et al., 2013; HANDWERGER et al., 2015). For a general treatment of InSAR terminology see for example MASSONNET & FEIGL (1998) or BÜRGMANN et al. (2000) and for more reviews of InSAR applications to landslides, the reader is referred to COLESANTI & WASOWSKI (2006) and WASOWSKI & BOVENGA (2014). Previous InSAR investigations, involving data from ERS and Envisat on slow moving landslides of the Northern Apennines (CORSINI et al., 2006; BERTI et al., 2013) found that sparse vegetation and land use often caused interferograms to be decorrelated and it was rarely possible to measure displacements higher than 26 mm in single interferograms (CORSINI et al., 2006) and velocities of more than 20 mm/year in PS-InSAR stacks (BERTI et al., 2013; TOFANI et al., 2013). Since the early 2000's various advanced post-processing strategies have been developed that are capable of reducing the problems related to decorrelation. The two most common techniques are the Persistent Scatterer approach (PS-InSAR, FERRETTI et al., 2001; ADAM et al., 2004) and Small Baseline Subset (SBAS, BERARDINO et al., 2002; SCHMIDT & BÜRGMANN, 2003; USAI, 2003). Both techniques were implemented in the open source framework of the Stanford Method of Persistent scatterers (StaMPS, HOOPER et al., 2007; HOOPER, 2008).

The study area is covered by several SAR-satellite missions. Although Envisat stopped acquiring data before the main excavation phase from 2010 to 2013, we used data from ascending and descending orbits of this satellite to obtain information

regarding slope movements before the excavation. The main excavation phase is covered only by COSMO SkyMed (CSK) and the period after the completion of the tunnel is covered by Sentinel 1A (S1A). The main characteristics of the datasets are summarised in Tab. 5.1. In the case of Envisat and COSMO SkyMed, interferometric processing was done with the open source software packages ROI-PAC (ROSEN et al., 2004) and DORIS (KAMPES & USAI, 1999).

Due to the limited number of interferograms, the time series of the descending COSMO-SkyMed products are often characterized by high frequency scatter. The mean velocity maps, on the other hand, can be used to integrate the data obtained by the ascending pass. The interferogram networks for both geometries contain several interferograms with large perpendicular baselines, which caused considerable problems during unwrapping and DEM error estimation in StaMPS. Although a large range of perpendicular baselines in the interferometric stack theoretically benefits the quality of the DEM-error estimate (FERRETTI et al., 2001), large baseline interferograms are also often affected by a higher degree of noise. Dropping those interferograms from the DEM error estimation and running DEM error estimation and unwrapping in an iterative way improved the final solution. Setting the stable reference area to a group of buildings close to the landslides also eliminated many problems during the unwrapping stage. For Sentinel 1A, interferometric processing was done with the software GMTSAR (SANDWELL et al., 2011). It was possible to form a high number of interferograms due to the high acquisition frequency and small perpendicular baselines, which are the two most influential parameters for decorrelation (ZEBKER & VILLASENOR, 1992).

In all cases, the Small Baseline module of StaMPS was used to produce InSAR time series. We included only interferograms that contained a clear phase signal. This selection criterion is very subjective and it involves trying different interferogram networks. However it helped significantly to improve the final results.

### **4.2.2 Monitoring data**

After the beginning of the main excavation stage of 2010, numerous inclinometer tubes were installed by the tunnel contractor. The readings of three of them are available to the public and are used in the present study (www-01, 2015, see also SM1, SM2, and SE1 in Fig.4.2 and Fig.4.3). The depths of the inclinometers

range from 80 m (SM1) to 50 m (SE1). Measurements were taken once a week during the excavation phase and continued with one measurement per month after 2014. Only SE1 is measured weekly due to relatively high displacement rates at this site. The readings of one piezometer is also available. It is positioned close to SM1 and contains two pressure sensors at depths of 10 and 20 meters.

A time-lapse GPS and a continuous GB-InSAR campaign were carried out by the Emilia Romagna Region between May and November 2011. An IBIS-L ground based radar was installed on the opposite slope of Ripoli/Santa Maria Maddalena and a corner reflector was positioned on a field north of Santa Maria Maddalena (Fig. 4.2). Furthermore, 15 points distributed along the deforming slope were periodically surveyed by means of a GPS. The GPS measurements were referenced with respect to a fixed station located at Vergato (Fig. 5.1) and measurements were carried out in non-regular intervals between one and three months.

### **4.2.3 Field survey and geophysical investigation**

In order to develop a detailed geotechnical/geomorphological model of the slope, we mapped the area during a field survey. We used aerial photos acquired during different periods (AZIENDA PER GLI INTERVENTI SUL MERCATO AGRICOLO, 1996; AGENZIA PER LE EROGAZIONI IN AGRICOLTURA –AGEA, 2008), a regional digital elevation model and the InSAR derived displacement maps to inform our interpretation of the slope. Moreover we used two surface geophysical techniques, known as HVSR or microtremor and MASW to acquire additional information regarding the underground geometry of one landslide. (NAKAMURA, 1989; CASTELLARO & MULARGIA, 2009). Similar techniques were successfully applied to the analysis of slope instabilities by DelGaudio2011 and Pilz2014.

## **4.3 Geological description of the slope**

### **4.3.1 Geological and geomechanical background**

The tunnel "San Benedetto" is part of the Highway project Variante di Valico that was approved in September 2001 (www-01, 2015). The excavation of the tunnel started during the first months of 2010. The project includes two circular tunnels

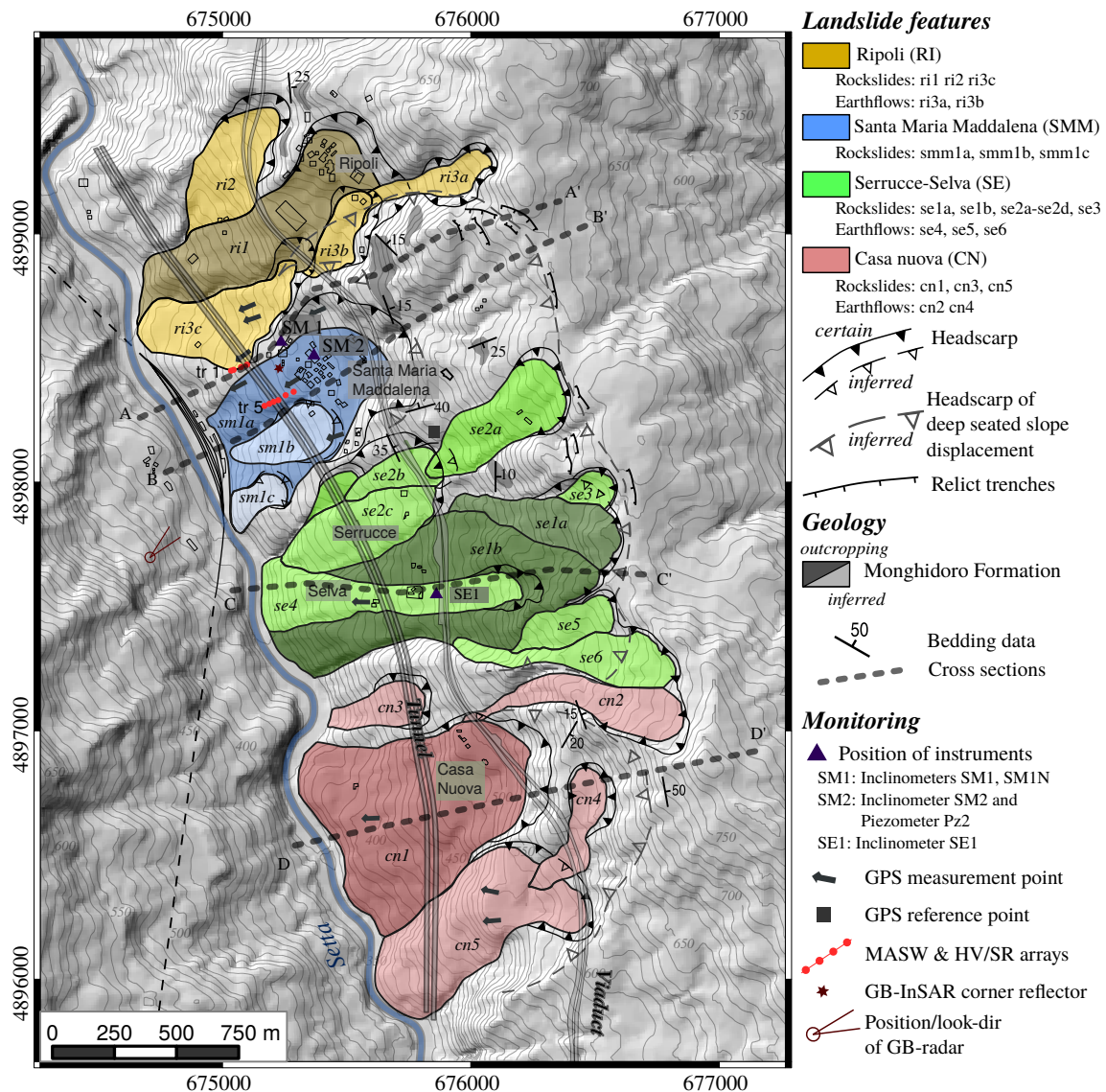


**Figure 4.2:** Geological and geomorphological map near Ripoli, Santa Maria Maddalena, Serrucce, Selva and Casa Nuova. Four different landslide complexes can be identified on the regional topographic map (scale 1:5000) based on geomorphological mapping. These landslide complexes are composed of one or more deep-seated landslides (dark colours) with nested superficial rockslides and earthflows (light colours, see text for details). Three inclinometer tubes were installed on the slope and a GPS campaign was carried out together with periodic measurements of a ground based InSAR. Moreover two MASW/HVSR arrays were extended on the Santa Maria Maddalena complex and on the crest next to the landslide body.

that run parallel to the Setta river valley and were excavated simultaneously using traditional techniques. Each tunnel has a total length of ca. 4 km, a diameter of 16 m and it is located at a maximum depth of ca. 120 m from the surface. Excavation

took place in both directions. From North to South, it passes under the villages of Ripoli and Santa Maria Maddalena, as well as under several groups of sparse houses that are called Serrucce, Selva and Casa Nuova. The old highway track was built in the 1950's and runs on the surface along the central part of the slope (Fig. 4.2).

The entire slope is made of turbidite deposits pertaining to the Monghidoro Formation (PANINI et al., 2002). It is a highly fissured and tectonically sheared sequence of sandstones, silts and clay-shales that crops out extensively in the Northern Apennines, often as overturned, folded and faulted slabs (MAXWELL, 1959). The slopes that develop on this geological formation are relatively gentle and rarely exceed 20 degrees. Outcrops are rare and, due to the complicated tectonic history, the rockmass is frequently sheared and fractured at the scale of the outcrop. Where the measurement of the orientation is possible, the bedding dips 10 to 40 degrees into the hillside (see Fig. 4.2). Although the regional geological map hypothesises a fold and an associated reverse fault in the central part of the slope (PANINI et al., 2002), field evidences are not sufficient to demonstrate the presence of meso-scale structures.

The climate in the study area is mediterranean with two rain periods, one that spans late September to early December and a second period from March to May. The periods between Autumn 2012 and Spring 2013, as well as Spring 2014 were characterized by unusual long and persistent rainfalls. At the rain gauge of Invaso (distance ca. 3 km) an average rainfall rate of 919 mm/year was registered for the years between 2000 and 2016 with 1271 mm and 1398 mm measured for years 2013 and 2014 respectively. The comparison with the longer historical series of the Montecuto rain gauge (distance ca. 4 km) confirms that these two years were unusually wet if compared to long time series (1950-2011). During the period 1950 to 2011, an average of 993 mm/year were registered and the annual precipitations of 2013 and 2014 were only surpassed 8 times.

The mechanical properties describing the behaviour of rock masses like the Monghidoro Formation are inherently difficult to estimate at the slope scale due to structural and lithological complexity MARINOS & HOEK (2001). The morphology of the relief in the outcropping area of the Monghidoro Formation provides guidance to interpret the behavior of the rock mass. Slope are gentle ( $15.5 \pm 7.3$  degrees) and landslide deposits are widespread, regardless of the relative slope-bedding orientation (area of mapped landslides / outcropping area: 31.9 percento ). Among authors who described the Monghidoro flysch, Borgatti2006 estimated GSI values of 19 with friction

angles ranging from 22 to 25.5 degrees and cohesion values ranging between 15 kPa and 1.9 MPa. In the study area, D'EFFREMO et al. (2016) report friction angles for the pelitic fraction that range from 14 to 24 degrees. They adopted 18 degrees (null cohesion) for landslide basal shear surfaces, and 35 degrees with 70 kPa cohesion were adopted for the bedrock. BANDINI et al. (2015) estimated low GSI values between 25 and 35 for the superficial portions of the rock-mass and values between 45 and 50 in greater depth. They attributed friction angles of 30 degrees and of 10 kPa cohesion to the landslide deposit and friction angles between 28 and 32 degrees and cohesions between 100 and 375 kPa. The fact that different authors report a large range of values for the same material illustrates well the difficulties involved in the geomechanical characterization of the Monghidoro Formation.

### 4.3.2 Geomorphology and landsliding

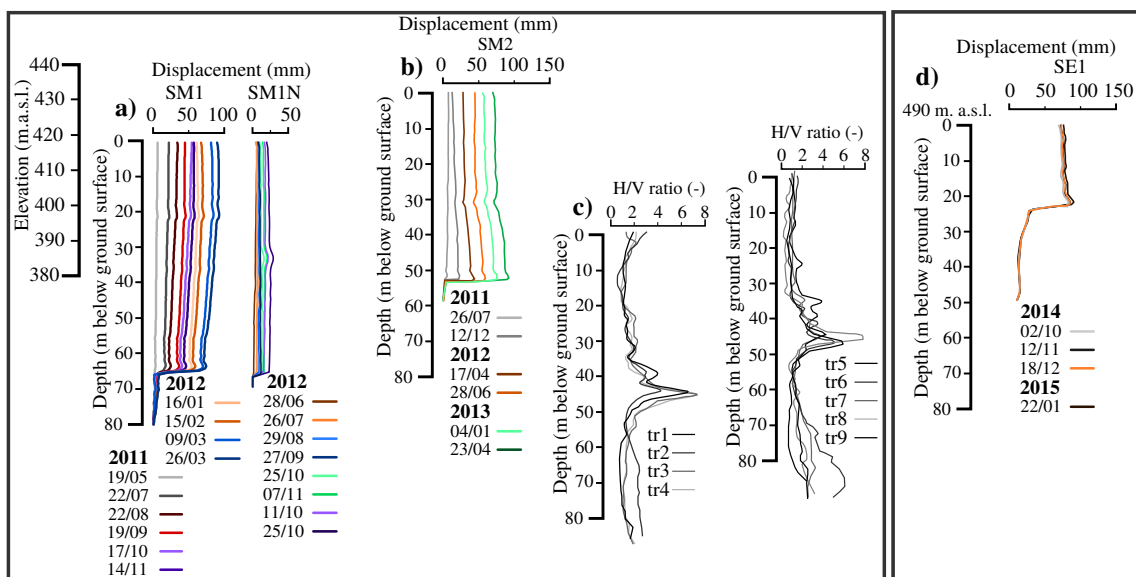


**Figure 4.3:** a) Inclinometer readings of the inclinometers SM1 SM1N. SM1N was installed close to SM1 after the latter one broke at a depth of approximately 60 m. Clear breaks in the deformation profile indicate slip surfaces at the depth of ca. 65 m in case of SM1. b) The inclinometer SM2 is located inside the mapped perimeter of the Santa Maria-complex and measures a slip surface in 55 m depth. c) HVSR/MASW measurements along the arrays tr1-tr4 and tr5-tr10 in the lower part of the slope show a peak in the ratio between horizontal and vertical shear wave velocities indicating a slip surface between 40 and 50 meters. d) The inclinometer SE1 measured a slip surface in 25 m depth. Vertical axis of charts in figures a), b) and c) are shifted to allow comparison in terms of absolute elevation (m a.s.l.).

Four main landslide complexes can be morphologically distinguished along the slope. Each complex is composed by a nested set of smaller landslides (Fig. 4.2). Most of the mapped landslides can be classified as compound rock-slides, rotational in the upper part and translational in the central and lower part (CRUDEN & VARNES, 1996). The headscarps, though partially reshaped, can be identified by relatively steep slope angles, whereas the deposits are characterized by convex and gentle morphology. Deposits may have experienced large, and possibly repeated, displacements during their history adding substantial disturbance to the rock mass that can locally appear as a soil BANDINI et al. (2015). The interpretation of the morphological features is complicated by the fact that most features are dormant and relatively ancient, most-likely post-glacial (BERTOLINI et al., 2005).

The northernmost complex is located under the town of Ripoli and includes one deep-seated gravitational failure and four associated landslides. In the following, we will refer to this group of landslides as the Ripoli-complex (yellow deposits in Fig. 4.2). The morphological interpretation suggests that the slip surface of the main landslide body (ri1 in Fig. 4.2) is located at a depth between 60 and 70 m from the ground surface. Two associated landslides (ri3a and ri3b in Fig. 4.2) are elongated and show flow-like morphology probably due to repeated movements. In this case (and in others later described), the landslide can be classified as earthflow (CRUDEN & VARNES, 1996; HUNGR et al., 2001; HUNGR et al., 2012). The interpretation of the topography and also the relation between length and width of the landslide body suggests that it is shallower compared to rock-slides and involves highly-to-completely weathered material. No inclinometer readings are available for this part of the slope, but four GPS-based surveys indicate a downslope displacement of the landslide body during the excavation (March 2012 through December 2013).

The second group of landslides is named after the village of Santa Maria Madalena and will be referred to as the Santa Maria-complex (blue deposits in Fig. 4.2). The main landslide is classified as a deep seated roto-translational rock slide (sm1a) and two minor rockslides can be distinguished (sm1b and sm1c) based on the local topography. The measurements of three inclinometers are available for this landslide (SM1, SM1N and SM2, Fig. 4.2). SM1 and SM1N are located next to each other at 420 m a.s.l. on the crest that separates the Ripoli complex from the Santa Maria-complex (Fig. 4.3 a), while SM2 is located inside the mapped perimeter of the Santa Maria-complex at a height of 435 m a.s.l (Fig. 4.3 b). The vertical displacement profile

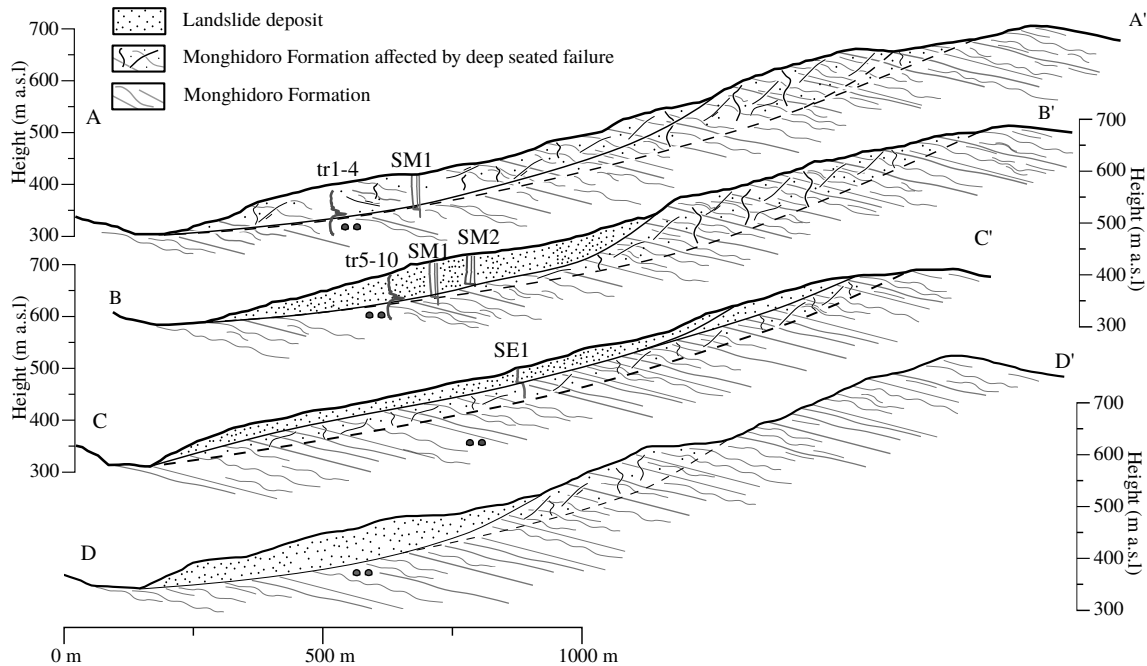


**Figure 4.4:** Four geological sections cross the main landslide complexes and show the conceptual geological model of the slope. See Fig. 4.2 for the position of the profile lines. A-A' profile along the crest between the RI and SMM complexes. B-B' profile along the thalweg of the SMM complex. C-C' crosses the SE-complex and D-D' the CN-complex.

of the inclinometer SM2 indicates the presence of a slip surface at a depth of 55 m. The topography of the slope suggests the presence of a slip surface that extends from the middle of the slope (550 m a.s.l.) down to the valley. However, partially reshaped, trench-like features were observed in the forested area at higher elevations (680 m a.s.l. in Fig. 4.2). The morphology of these features is variable, but in particular near the crest they appear as graben-like structures with an approximate depth of 1.5 m that can be traced in the map for ca. 500 m. Their slope-parallel orientation, their appearance in the field and their shape in the profiles compare well to morphologies that were described on old deep seated gravitative slope deformations in crystalline as well as in sedimentary rocks in the Alps and the Apennines (ZISCHINSKY, 1969; SPAUN, 1979; SORRISO-VALVO, 1995). The presence of a deep seated failure would also be supported by inclinometer measurements at SM1, that indicate a slip surface at ca. 65 m. Given the close small distance with respect to the inclinometer SM2 (Fig. 4.2), and their relative position in height (Fig. 4.3 a,b), it is unlikely that the slip surface in SM1 (65 m) corresponds to the slip surface in SM2 (55 m). In order to obtain additional information regarding the geometry

of the landslide complexes, we extended two HVSR/MASW arrays. One array is located along the crest between the Santa Maria and the Ripoli-complex (tr1-tr4 in Fig. 4.2) and the second array was extended inside the mapped landslide perimeter of the Santa Maria Maddalena complex (tr5-tr10 in Fig. 4.2). The vertical profile of the ratio between horizontal and vertical components of the ambient seismic noise shows a peak at an approximate depth of 50 m for both arrays (Fig. 4.3 c). The peak is caused by a contrast in seismic velocities with lower velocities above the peak and higher velocities in greater depths. This contrast is in our view best explained by the basal shear zone the Santa Maria complex and the deep seated failure.

Two geological sections A-A' and B-B' (Fig. 4.2 and Fig. 4.4) were chosen to illustrate our interpretation of the slope. The profile A-A' extends along the crest between the Santa Maria-complex and the Ripoli-complex shows landforms, that are common in deep seated gravitative slope deformations, like concave portions in the upper part, convex portions in the central part and a steep front towards the river (SPAUN, 1979). The slip surface measured in inclinometer SM1 is compatible with a deep slip surface that extends over the whole slope. The profile B-B' extends across the mapped part of the Santa Maria-complex. The slip surface measured in SM2 can be attributed to the mapped headscarp in the central part of the slope. Also in this orientation the topography suggests the presence of the aforementioned deep seated failure.

The third landslide complex is located further south and is composed of three rockslides, similar in their morphological characteristics. They are located in the vicinity of a group of houses called "Serrucce" and "Selva". Hence we will refer to this landslides as Serrucce-Selva complex. It is composed of two main landslides (se1a and se1b in Fig. 4.2) and several minor rock slides (se2-se6). Analogous to the Ripoli complex, the central main rockslide body hosts an elongated failure that has flow like morphologies (se4 in Fig. 4.2). Here the GPS measurements indicate a displacement directed along the slope and the inclinometer SE 1 is located in the central part of this earthflow. The vertical deformation profile of SE 1 shows a sliding surface at 25 m (Fig. 4.3 d). The morphology in the topographic profile along line C-C' (Fig. 4.4) suggests a deeper slip surface that extends from 680 m a.s.l. to the valley, which is not measured by the inclinometer due to insufficient depth. Also in this case, relict trenches are visible at intervals in close vicinity of the upper ridge of the slope (Fig. 4.2).

The southernmost group of landslides is separated from the Serrucce-Selva complex by a crest that can be considered relatively stable and extending towards the southern portal of the tunnel. The landslide complex is named after the group of houses in the lower part of the slope ("Casa nuova", red colors in Fig. 4.2) and downslope displacements were measured by GPS campaigns. A deep seated rockslide is associated with four minor failure zones. Two of them can be classified as earthflows (cn2 and cn 4 in Fig. 4.2). The cross section D-D' (Fig. 4.4) shows the main landslide body and another deep seated rock-slide can be deduced from the topography.

## 4.4 Kinematic behaviour of the landslide complexes

### 4.4.1 InSAR derived displacement maps

The period before the excavation is covered by the ESA satellite Envisat, and the SBAS results indicate the absence of notable displacements along the slope (Fig. 4.5 a-b). However, small deformations with less than 5 mm/year are visible on small parts of the Casa Nuova complex, which is consistent with results obtained with ERS results reported in BANDINI et al. (2015). No deformation is detected during the initial stage of the excavation, although the high degree of noise in these interferograms might mask the true signal. During the excavation, COSMO SkyMed acquired numerous scenes over the study area (Tab. 5.1). The SBAS results derived from the ascending dataset indicate a range decrease (movement towards the satellite, Fig. 4.5 c) while the descending pass measured a range increase and hence a movement away from the satellite along the line of sight (Fig. 4.5 d). This can be interpreted as a downslope-oriented movement, which is also consistent with the GPS measurements in Fig. 4.2). Displacement rates of up to 15 mm per year along the line of sight were measured with respect to the Santa Maria Maddalena complex and the Selva complex (Fig. 4.5 c and d), while the mean velocities remained below 10 mm per year for the other landslide groups. During the period that followed the excavation, deformation maps were derived from Sentinel 1A. Although mean velocities remain locally high for the Ripoli, the Selva and the Casa nuova landslide complexes, the villages of Ripoli and Santa Maddalena were not affected by detectable movements between October 2014 and May 2016 (Fig. 4.5 e and f).

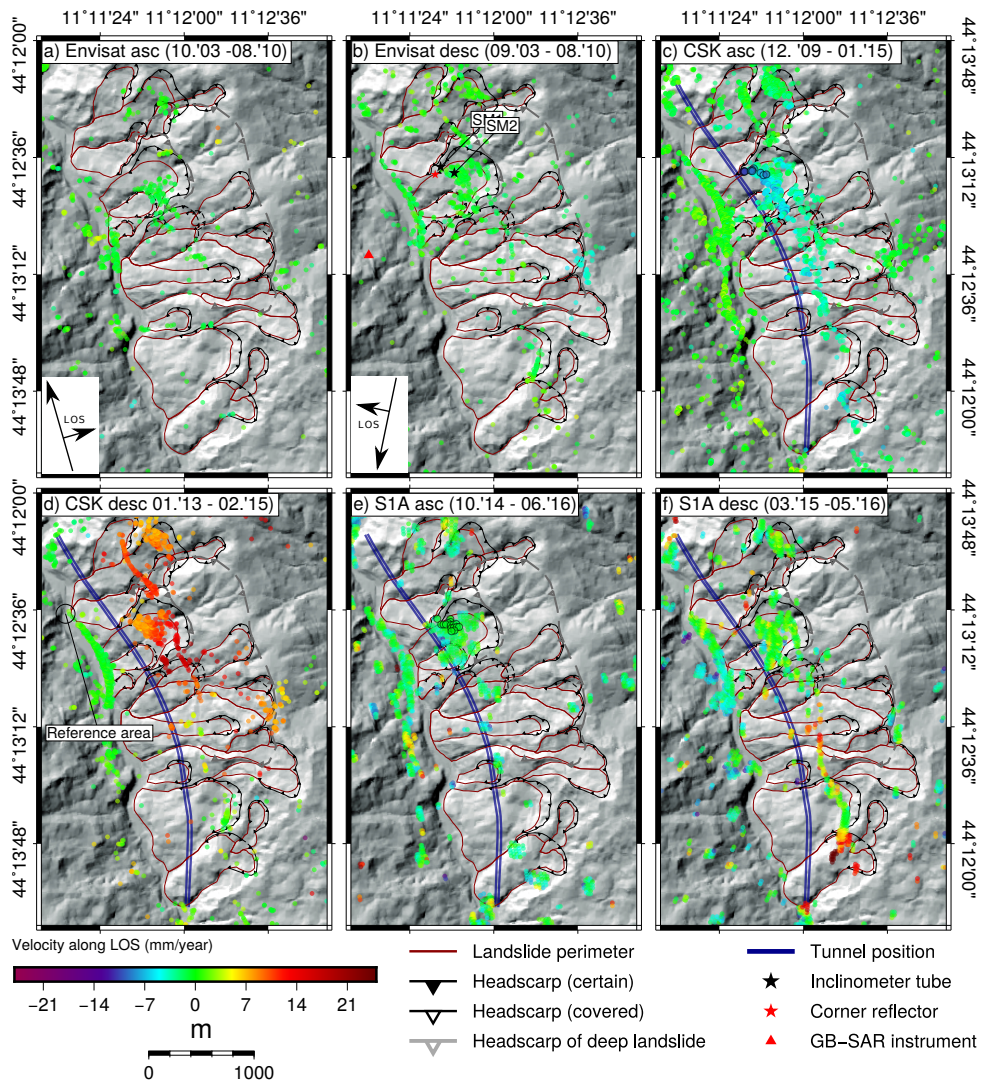


**Figure 4.5:** InSAR-derived velocity maps for the different small baseline datasets derived from the different satellites. *asc* indicates ascending and *desc.* indicates descending look direction, while blue colours indicate a range movement towards the satellite, yellow and red colours indicate a movement away from the satellite. a) The ascending Envisat dataset reports slow deformations in movement towards the satellite for the Casa Nuova complex, where the descending dataset measured deformations away from the satellite. Also a larger signal in movement towards the satellite is visible in the upper part of the slope. Since it is not visible in the ascending dataset and it crosses the main crest, it should be interpreted as noise. c) The ascending pass of COSMO SkyMed measured extensive movements towards the satellite on most parts of the slope. d) The descending pass of COSMO Skymed registered movement away from the satellite. e) The ascending pass of Sentinel measured also a range decrease where the f) descending track measured range increases.

#### 4.4.2 Deformation history at Santa Maria Maddalena

A common approach to visualize InSAR-derived displacements in time is to plot timeseries of cumulative displacement. This is not only useful to analyze the nature of the temporal displacement (i.e. steady, non steady, seasonal etc.), but it also offers the possibility to compare InSAR results to displacements that were measured by ground-based monitoring instruments. For this comparison, it is necessary to display the deformation in a common coordinate system. Because three dimensional displacements vary spatially on landslide bodies, we chose the look vector of the ascending viewing geometry of COSMO SkyMed as a reference coordinate system and projected the inclinometer and GB-InSAR displacements along its direction (see Appendix I for details regarding the projection procedure).

In the Santa Maria Maddalena complex, non-InSAR monitoring data were detailed enough to allow the comparison. The inclinometer SM 1 is located on the ridge between the Ripoli and Santa Maria Maddalena complexes (Fig. 4.2). It measured increasing displacement rates during 2012 when the excavation of the first tunnel approached the area (Fig. 4.6 a). Few months later, as excavation proceeded southward, also the inclinometer SM 2, registered increasing displacements rates. Peak values are measured when the excavation of both tunnels is active below the landslide complex. During this period the inclinometer SM1 was disturbed due to shear displacement, and new boreholes were drilled to continue inclinometer readings (SM 1, SM 1 N in Fig. 4.6 a).

InSAR-derived displacements for all SBAS pixels located on the houses next to the two inclinometers are consistent with their measurements (highlighted pixels in Fig. 4.5 c and e). The two InSAR time series in Fig. 4.6 a show the mean cumulative displacements of all highlighted pixels in Fig. 4.5. We chose to display the mean of the selected pixels in order to smooth the high-frequency noise often affecting in the time series of single pixels. The InSAR data also register an increase of displacement rates at pixels close to inclinometer SM 1 when only the first tunnel was being excavated under the landslide. Afterwards, slope deformation progressed southward in agreement with the excavation, with the highest observed displacement rates corresponding to the phase of simultaneous excavation of the two tunnels below the village of Santa Maria Maddalena. Displacements slowed down after the tunnel fronts moved south of the landslide complex although the SBAS results derived

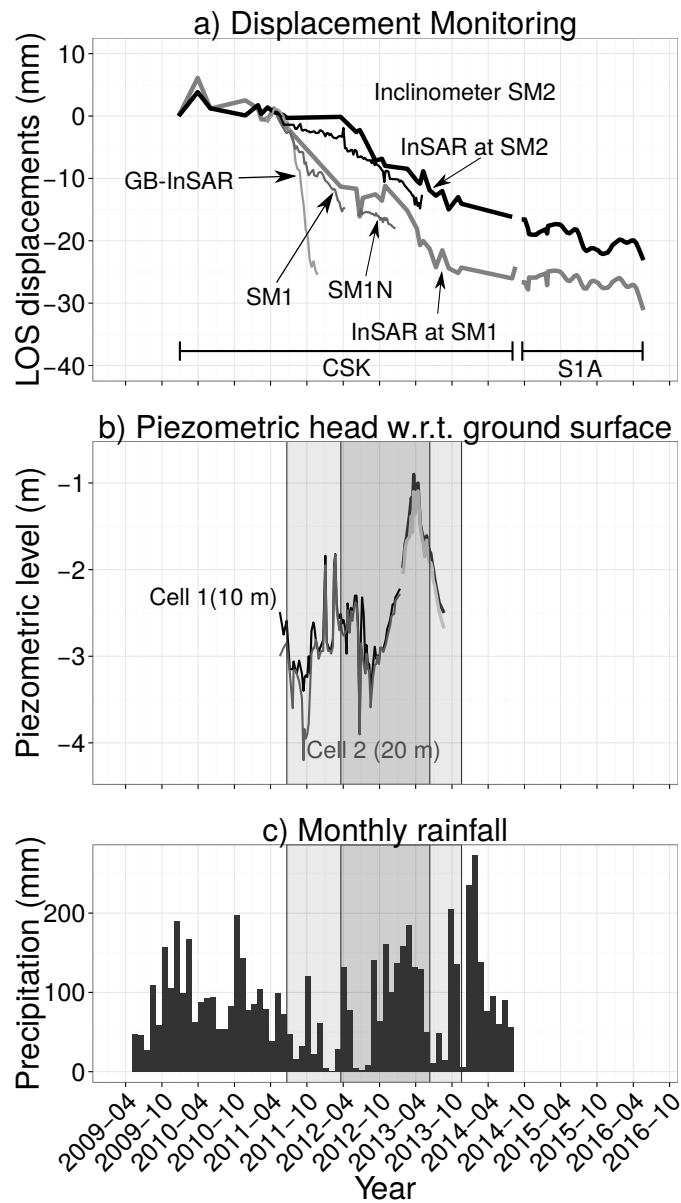


**Figure 4.6:** a) Mean cumulative displacements in time for the SBAS pixels that are located next to the inclinometers SM 1 and SM 2 together with the displacements derived from these inclinometers and the GB-InSAR measurements on the corner reflector of Santa Maria Maddalena. Both the inclinometer and the GB-InSAR displacements were projected into the line-of-sight vector of the ascending COSMO SkyMed geometry. b) Piezometric head with respect to the ground surface of Piezometer Pz 2 for the pressure cells at 5 and 10 m depth, respectively. c) Total monthly precipitation measured at the rain gage Invaso which is located in the adjacent valley at a distance of approximately 1 km towards North East with respect to Santa Maria Maddalena. The light grey area indicates the period during which one tunnel was excavated under the slope, while the dark grey area marks the period when both tunnels were excavated.

from Sentinel indicate locally small line-of-sight displacements (15-20 mm/a). The inversion of the sign for ascending and descending viewing geometry suggests a down-slope orientation of the real displacement vector.

A corner reflector was installed on an agricultural field west of inclinometer SM 1 (Fig. 4.5 b). On the corner reflector the relative acceleration of the landslide body was measured by the ground based InSAR, although it measured higher displacements if compared to the deformation reported by the inclinometer and the SBAS results (Fig. 4.6 a). It is possible that the projection of the GB-InSAR data led to an overestimation of displacements, because the projection is sensitive to the vertical component of the look vector of the GB-InSAR (see Appendix I). It is also possible that, due to soil creep, superficial displacements on the agricultural field were slightly higher than those measured by the inclinometer and the SBAS results.

In direct vicinity of the inclinometer SM 1, two piezometers measured pore pressures at 10 and 20 meters. The piezometric levels display very similar trends at increasing depth with slightly higher values at shallow depth that indicate the absence of significant flow barriers and a possible vertical recharge component (Fig. 4.6 b).

The precipitation for the period of interest, which are expressed in Fig. 4.6 c as average monthly rainfall, were enough to saturate the landslide body. In fact, the piezometric levels inside the landslide body rose steadily during winter and got close to the ground surface in May 2013 before decreasing during the following summer period (Fig. 4.6 b). As mentioned earlier, the spring periods of 2013 and 2014 were characterized by long enduring rainfall, which is why a similar piezometric response was probably caused by abundant spring rainfalls in 2014 (unavailable piezometric data). In terms of surface displacements, no accelerations are clearly correlated with precipitation in the spring seasons of 2013 and 2014. The fact that the displacement rates do not rise with pore water pressures supports the interpretation that surface deformation was caused by a deep seated rock-slide whose movement is related to the excavation and is less affected by fluctuations of interstitial water pressure at depth.

### **4.4.3 Spatial and temporal development of the displacements**

Since InSAR is capable of monitor displacements over large areas, we take advantage of this feature to relate the displacement rates along the slopes and the position of

#### 4 Deformations induced by tunneling under deep-seated landslides

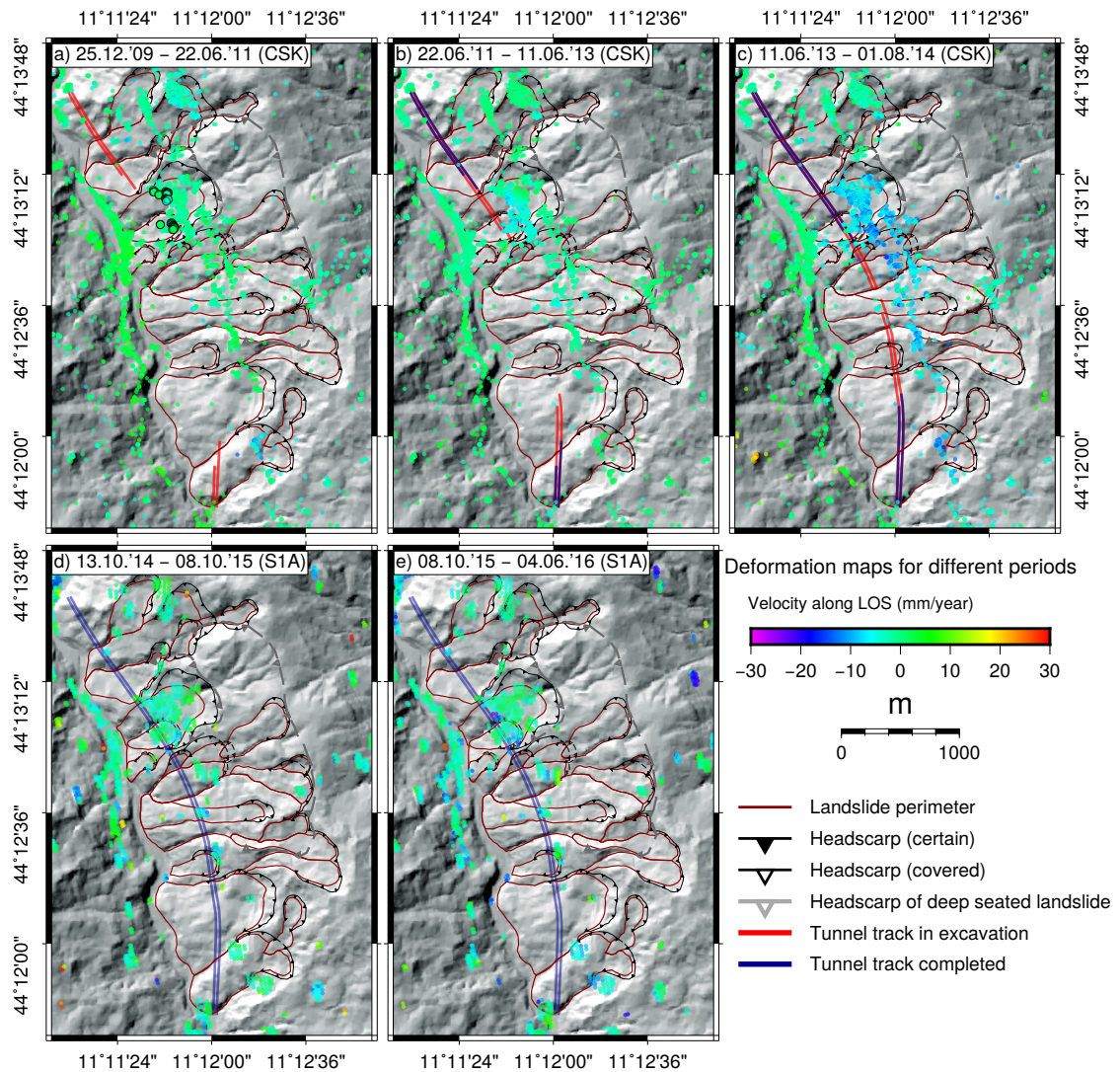


**Figure 4.7:** Spatial distribution and mean LOS displacement rates derived from the ascending passes of COSMO SkyMed and Sentinel for different periods in relation to the advance of the tunnel front. a) Mean velocities for the initial stages of the excavation. Slow displacements are visible at the villages of Ripoli in the North and the houses Casa Nuova in the South. The highlighted pixels were used for the velocity analysis in Fig. 4.8. b) As the tunnel front proceeds the displacement rates become high at Santa Maria Maddalena and slow down at Ripoli and on the Casa Nuova complex c) During the main stage of the excavation displacements are high on all landslide bodies and also the crests between the landslide complexes are affected by deformation. Displacement rates are highest at small distances from the tunnel fronts. d) Mean velocities decreased after excavation finished, although locally displacements continue to persist. e) Also during the second year after the excavation the situation improved in terms of displacement rates, yet also during the period between October 2015 and June 2016 displacements were measured.

the tunnel excavation front. The comparison between the spatial deformation pattern and excavation operations is done by calculating mean LOS velocities for five successive periods that are plotted in relation to the advance of the tunnel front (Fig. 4.7). The tunnel position was determined from status reports available on the homepage of the observatory ([www-01](http://www-01)). Between December 2009 and June 2011, small displacements were measured by InSAR within the northern Ripoli-complex and the southern Casa Nuova complex while other landslides located in the central part of the slope show negligible movements (Fig. 4.7 a). The excavation of the tunnels continued both from North to South and from South to North. Between June 2011 and June 2013, higher displacement rates were observed in the Santa Maria complex (Fig. 4.7 b), which is consistent with the time series reported in Fig. 4.6 a. This changed during the period between June 2013 and June 2014, which covered the final stages of the excavation. Right before the northern tunnels connected to the southern tunnels, mean velocities were elevated throughout the landslide complexes and two local areas of high displacement rates (up to 30 mm/year) are visible on the slopes above the tunnel fronts (Fig. 4.7 c). However, pixels with high LOS-velocities ( $> 10$  mm/year) are widespread across the entire slope. They are located on landslides overlying the tunnel fronts, landslides that were already surpassed by the excavation, as well as on ridges that separate the landslide complexes. In our view it is possible that this spatially extensive signal is caused by the slow deformation of a deep-seated gravitational movement that encompasses the previously described landslide complexes. After the tunnel was completed in late November 2014, displacement rates decreased and between October 2014 and October 2015 mean velocities were only locally significant in the Ripoli and the Selva complexes (Fig. 4.7 d). Also during the second year after the completion of the tunnels (Fig. 4.7 e), high displacements were spatially localized. In addition to Selva and Ripoli, also small portions of the Santa Maria and Casa Nuova complexes showed displacement rates higher than 10 mm/year.

In order to gain further insight into the slope dynamics, we focus on the Santa Maria Maddalena village that experienced the most severe damage. We exploit the high temporal resolution of InSAR measurements (Tab. 5.1) to compare displacement rates to the relative position of the tunnel front, the excavation rate and the precipitation. Because the velocity time series were affected by high frequency scatter, we used a local regression filter to smooth the velocity signal in time, and

#### 4 Deformations induced by tunneling under deep-seated landslides

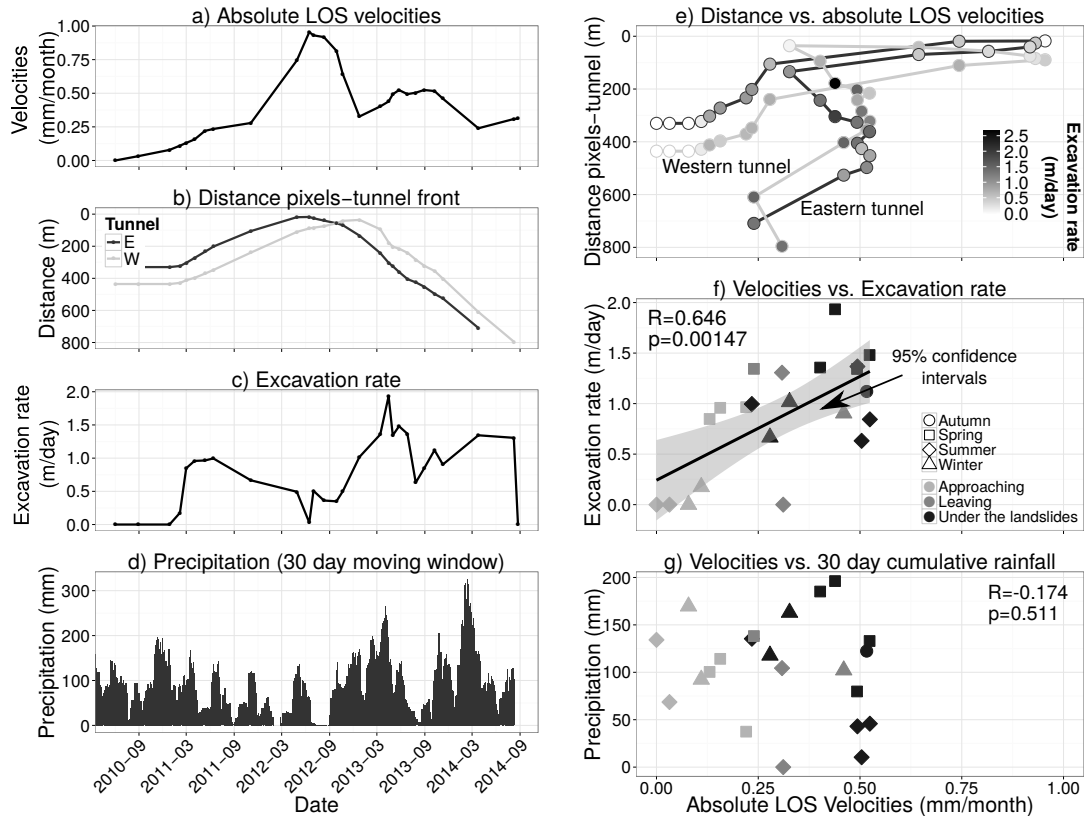


**Figure 4.8:** a) Absolute line of sight velocities for the pixels highlighted in Fig. 4.7 a). In this representation, positive values represent a range decrease and hence a movement towards the satellite. b) Distance between the tunnel position and the highlighted pixels. c) Variation of the excavation rate over time. d) Thirty days cumulative rainfall (see text for details). e) Relation between the velocities and tunnel position. The arrows represents the advance of the western and the eastern tunnel fronts, while the different grey scales of the filled points indicated the excavation rate. f) Relationship between velocity and excavation rate. The grey represents the 85 %confidence interval of linear regression. g) Relationship between velocity of thirty days of cumulative rainfall.  $R$ : correlation coefficient;  $p$ : p-value.

analyzed the mean of all pixels located on the houses of Santa Maria Maddalena (highlighted pixels in Fig. 4.7 a). Given the depth of the observed landslides, the deformation response to rainfalls is expected to be slow and, due to recharge/discharge characteristics of landslide material (e.g. BOGAARD & GRECO, 2016), will depend on the precipitation before the change in displacement style. In order to account for the antecedent rainfall we used a mobile window to sum the preceding thirty days to each daily precipitation value (total thirty day rainfall in the following).

The LOS velocities reached maximum values of approximately 1 mm/month (Fig. 4.8 a), when both tunnels were excavated (Fig. 4.8 b), and the daily precipitation was low

to moderate ( $<4$  mm/day and  $< 100$  mm total thirty day rainfall, Fig. 4.8 d). A second period of relatively high displacement rates (0.5 mm/month ca.) was measured during Summer/Autumn 2013, following intense and persistent rainfalls. During this period, also the excavation rate reaches maximum values and could also explain the second peak in velocities (Fig. 4.8 c). If the LOS velocities of each timestep are compared to the relative position of the tunnel front (Fig. 4.8 e), it becomes clear that the first peak of displacement rates is caused by the approaching excavation of the tunnel front. The tunnel excavation rate is represented in Fig. 4.8 e its maximum values precede the second peak of displacement rates. In order to evaluate the main influence on the second peak in the velocity time series, we compared the mean velocities to the excavation rate and the thirty day total rainfall. We excluded velocities greater than 0.6 mm/month to investigate these relationships (Fig. 4.8 f and g) because the peak values of velocity are clearly related to the position of the excavation front. Velocities and excavation rate are linearly related ( $R=0.646$ ), and their relationship can be considered statistically significant ( $p\text{-value}=0.001147$ ). We found no significant correlation between thirty day rainfall and velocities ( $R=-0.147$ ,  $p\text{-value}=0.51$  Fig. 4.8 g). Time steps of intense precipitation during 2013 or 2014 do not correspond to an increase in the displacement rates. No decline is recorded during the dry periods. On the contrary, peak displacement rates correspond to low precipitations in the record. Changing the timespan of antecedent rainfall to higher values of more than 180 days had little influence on both correlation coefficient and  $p\text{-value}$ .

## 4.5 Discussion and concluding remarks

The case of the San Benedetto Val di Sambro tunnel shows that the interaction between large infrastructure projects and geological features, like old dormant landslides, can be complex. We exploited different InSAR datasets to analyze the deformation behaviour of a slope before, during, and after the excavation of a double road tunnel. Large parts of the slope are covered by landslide deposits. Based on the analysis of existing data and geomorphological evidences, we identified four main landslide complexes. These complexes are composed by one main landslide body and several nested landslides, which can be mostly classified as deep seated

rock slides evolving, in few cases, to earthflows (CRUDEN & VARNES, 1996; HUNGR et al., 2001; HUNGR et al., 2012). Multiple evidence also suggests the presence of a deep seated gravitational slope movement, which extends over the whole slope and encompasses the multiple landslide complexes. First inclinometer SM1, located outside the mapped landslides, measured a distinct slip surface at a depth of approximately 65 meters. At the same depth, our microtremor measurements indicate the presence of a discontinuity. Second, relict morphological features, that can be interpreted as old re-modelled and eroded trenches, are visible in the upper part of the slope running parallel to slope crest. They correspond probably to the headscarp of this phenomenon. Third, our InSAR results revealed a spatially extensive signal that embraces the outlines of the deep seated gravitative slope displacement.

Extensive deformation occurred along the slope during the excavation of the tunnel. The main settlement (Santa Maria Maddalena) experienced widespread damage to the houses. Monitoring data that were made public by the tunnel contractor, showed that the landslide bodies started to move when the first tunnel front approached the limit of the landslide complex and constrain the depth of the sliding surfaces. The InSAR results show a progression of surface displacement in space and time. They demonstrate that deformation was associated to the reactivation of dormant landslides rather than to the subsidence due to the underground excavation. Displacements were highest when both tunnel fronts were being excavated under the landslide bodies and deformation rates decelerated after both tunnels were completed. The fact that displacement rates were higher during periods of low pore pressures suggests that the hydrological influence on the movement of these deep seated rock-slides is minor and that the tunnel is the main driver of the displacements. The relationship between the position of the tunnel and displacement is also visible in the deformation maps of Fig. 4.7.

The projection of the ground monitoring data into the reference coordinate system of COSMO SkyMed's ascending look vector enabled the comparison of the monitoring results. In particular the displacements derived from inclinometers and the SBAS results obtained by StaMPS are in good agreement.

A thorough comparison between mean LOS velocities at Santa Maria Maddalena and the position of the tunnel front in time, excavation rate and precipitation confirm that the tunnel is the key influence on the observed slope deformation. A clear relationship between the relative position of the tunnel front with respect to scat-

terers and the corresponding displacements rates is visible. Peak velocities are, in fact, measured when the spatial distance from the excavation front is minimum. A second period of acceleration is observed during the months following intense and prolonged rainfalls but, based on available data, it is more probably related to an increase in the excavation rates. For the complete period of our InSAR survey, no relationship between precipitation and displacements is indicated, and peak velocities are attained during dry periods. Hence we believe that rainfall only had minor influence on the displacement history of the investigated landslides.

Our analysis yields several conclusions. From a geomorphological and engineering geological point of view, the slope over the San Benedetto Val di Sambro tunnel hosts four landslide complexes composed mainly of deep seated rockslides. The monitoring results show that damages on the houses and the infrastructure were caused by the deformation of these landslide complexes rather than by subsidence.

In the case of the San Benedetto Val di Sambro tunnel, landslide accelerations are related to the ongoing underground excavation. The InSAR-derived spatio-temporal deformation patterns show a clear relationship between landslide displacement and position of the tunnel fronts. Data also suggest that high excavation rates may accelerate landslides while the comparison with rainfalls and piezometric data suggests that the hydrological regime of the slope had little impact on the deformation. The geomorphological mapping, the inclinometer measurements and the distribution of the InSAR derived velocity maps suggest that parts of the deformation were caused by a deep seated gravitative slope displacement that extends from the valley to the main crest of the slope.

Whether the interference could have been predicted in the design stage is a question we cannot answer, given that we were not involved in the design process. Anyway, the key issue is represented by the correct interpretation of landslide type, geometry and associated kinematics. On the one hand the morphology of the slope is complex and gravitational features are old and partially remodeled. On the other hand, widespread presence of large landslides deposits was reported by official geological maps before the excavation started. Probably, the most important factor that influences the interaction between tunneling and landslide deformation is the distance between the excavation and the landslide slip surfaces. Given that the slope was stable before tunneling commenced, monitoring would have yielded no additional information regarding the geometrical nature of the landslides. Hence

the position of the slip surfaces could be identified either by the interpretation of geomorphological maps and topographic cross section, or on the base of core drillings interpretation. The first approach is subjective and prone to large uncertainties. In case of borehole interpretation, the task is complicated by the high degree of tectonic disturbance of the bedrock material that can be confused with disturbance caused by gravitational movement. While recognizing the difficulties of interpretation, it can be stated that whenever underground excavation is performed in a slope where landslide deposits are recognized, the possible interactions have to be evaluated and extra-care has to be taken in the positioning of the tunnel with the aim to maximize the distance to overlying slip surfaces.

The deformations derived from Envisat show that the landslides were in a relative stable condition before the tunneling started. The deformation signals obtained from the last COSMO SkyMed acquisitions and from Sentinel 1A datasets illustrate the deceleration of most landslide bodies, although deformations remained high at the localities of Selva and Casa Nuova and did not decrease to the velocities measured before the excavation. From a remote sensing point of view, it can be stated that the InSAR derived deformations compare well to the results of the inclinometer measurements while GB-InSAR measurements indicate slightly higher displacement rates. The case is well suited for a spaceborn InSAR survey, because displacements occurred on a relatively large spatial extent and, due to the presence of houses, a high number of pixels was selected. Also the favourable west-facing orientation of the slope allows to satisfactorily resolve the displacement along the satellite line of sight. The results show also that the remotely sensed surface displacements can be used to integrate classical ground-based monitoring. InSAR data are especially useful because they can investigate a large area and embrace a long time span, providing a historical perspective of active processes and surrounding areas.

## Acknowledgements

We would like to thank the Geological Survey of the Region Emilia Romagna for providing GPS and GB-InSAR measurements. Also we would like to thank Marco Pizziolo and Mauro Generali for useful discussions regarding the geological model of the slope. Precipitation data was obtained from the dexter download system of

ARPA Emilia Romagna (<http://dexter-smr.arpa.emr.it/>, currently not available). We thank the Italian Space Agency (ASI) for delivering the COSMO SkyMed imagery and we thank the European Space Agency for the Envisat and Sentinel data. The comments by Janusz Wasowski, Paolo Frattini and Francesca Bozzano helped to improve an earlier version of the present manuscript.

## References

## Appendix I

Given the azimuth  $\beta$  and the slope  $\gamma$  of the real displacement and given the incidence angle  $\theta$  and satellite heading  $\alpha$  of the satellite it is possible to express the unit vectors for displacement  $\hat{d}$  and the look vector  $\hat{l}$  as:

$$\hat{d} = \begin{bmatrix} d_{north} \\ d_{east} \\ d_{vert} \end{bmatrix} = \begin{bmatrix} \cos(\beta) \sin(90 - \gamma) \\ \sin(\beta) \sin(90 - \gamma) \\ \cos(90 - \gamma) \end{bmatrix} \quad (4.1)$$

$$\hat{l} = \begin{bmatrix} l_{north} \\ l_{east} \\ l_{vert} \end{bmatrix} = \begin{bmatrix} -\sin(\alpha) \sin(\theta) \\ \cos(\alpha) \sin(\theta) \\ \cos(\theta) \end{bmatrix} \quad (4.2)$$

The line of sight displacement of a real displacement vector in three dimensions is then given by:

$$d_{los} = d_{real} \left( \hat{d} \cdot \hat{l} \right)^{-1} \quad (4.3)$$

The projected line of sight displacements in Fig.4.6 a) were derived for the inclinometer SM 1 with a slope of 15 degrees with respect to the horizontal and an azimuth of 230 degrees from North, while for the inclinometer SM 2 a slope of 17 degrees from the horizontal and an azimuth of 260 degrees from North were used. For the ground based InSAR survey the look vector of the GB-InSAR was derived

from the coordinates and heights of the instrument and the corner reflector. It can be expressed as:

$$\hat{l}_{gbs} = \begin{bmatrix} l_{gbsnorth} \\ l_{gbseast} \\ l_{gbsvert} \end{bmatrix} = \begin{bmatrix} lat_{cor} - lat_{gbs} \\ lon_{cor} - lon_{gbs} \\ h_{cor} - h_{gbs} \end{bmatrix} \quad (4.4)$$

Where  $lat_{cor/gbs}$  and  $lon_{cor/gbs}$  correspond to longitude and latitude of the corner reflector and the ground based SAR, while  $h_{cor/gbs}$  correspond to the heights of both instruments. In order to obtain all values in meters we chose the projected UTM/32N coordinate system that is however referenced to the WGS84 ellipsoid. The projection is done in analogy to equation 3:

$$d_{los} = d_{gbs} \left( \hat{l}_{gbs} \cdot \hat{l} \right)^{-1} \quad (4.5)$$

It should be noted that the projection is sensitive to the vertical components of the displacement vectors that are projected into the line of sight. In case of the inclinometers this corresponds to the angle between the displacement vector and the horizontal, while it corresponds to the difference in height between the radar antenna and the corner reflector in case of the ground based InSAR survey. Inclinometers can not measure the slope of the displacement vector, which is why we assumed an angle that corresponds to the inclination of the slip surface from the horizontal, which also compares well to the slope of the ground surface. While this worked well in the present case, it is not said that this might be similar in other landslides. Differences in the displacement unit vector would cause numerical differences in the absolute values between the monitoring data and InSAR time series. Relative trends, like the observed acceleration and deceleration in relation to the tunnel position are visible however in both datasets.

## 4.6 References

ADAM, D., MARKIEWICZ, R. & BRUNNER, M. (2014): Block-in-matrix structure and creeping slope; tunneling in hard soil and/or weak rock. – Geotechnical and Geological Engineering, **32** (6), pp. 1467–1476;

- ADAM, N., EINEDER, M. & KAMPES, B. (2004): Development of a scientific persistent scatterer system: Modifications for mixed ERS/Envisat time series. – ENVISAT & ERS Symposium, **6–10 settembre** (Austria), pp. 1–9; Salzburg.
- AGENZIA PER LE EROGAZIONI IN AGRICOLTURA –AGEA (2008): Ortofoto multifunzione Emilia Romagna. – versione digitale; Bologna (Regione Emilia Romagna).
- AZIENDA PER GLI INTERVENTI SUL MERCATO AGRICOLO (1996): Orthofoto AIMA bianco/nero 1996-97. – versione digitale; Bologna (Emilia Romagna).
- BANDINI, A., BERRY, P. & BOLDINI, D. (2015): Tunnelling-induced landslides: The Val di Sambro tunnel case study. – *Engineering Geology*, **196** (), pp. 71–87;
- BARLA, G., DEBERNARDI, D. & PERINO, A. (2015): Lessons learned from deep-seated landslides activated by tunnel excavation. – *Geomechanics and Tunneling*, **8** (5), pp. 394–401; Berlin.
- BARLA, G., TAMBURINI, A., DEL CONTE, S. & GIANNICO, C. (2016): InSAR monitoring of tunnel induced ground movements. – *Geomechanics and Tunneling*, **9** (1), pp. 15–22;
- BERARDINO, P., FORNARO, G., LANARI, R. & SANSOSTI, E. (2002): A new algorithm for surface deformation monitoring based on small baseline differential SAR interferograms. – *Ieee Transactions On Geoscience and Remote Sensing*, **40** (11), pp. 2375–2383; New York.
- BERTI, M., CORSINI, A., FRANCESCHINI, S. & IANNAcone, J. P. (2013): Automated classification of Persistent Scatterers Interferometry time series. – *Natural Hazards and Earth System Sciences*, **13** (8), pp. 1945–1958;
- BERTOLINI, G., GUIDA, M. & PIZZIOLo, M. (2005): Landslides in Emilia-Romagna region (Italy); strategies for hazard assessment and risk management. – *Landslides*, **2** (4), pp. 302–312; Heidelberg.
- BOGAARD, T. A. & GRECO, R. (2016): Landslide hydrology: from hydrology to pore pressure. – *Wiley Interdisciplinary Reviews-water*, **3** (3), pp. 439–459;

- BOLDINI, D., GRAZIANI, A. & RIBACCHI, R. (2004): Raticosa Tunnel, Italy: Characterization of tectonized clay-shale and analysis of monitoring data and face stability. – *Soils and Foundations*, **44** (1), pp. 57–69;
- BOVENGA, F., WASOWSKI, J., NITTI, D. O., NUTRICATO, R. & CHIARADIA, M. T. (2012): Using COSMO/SkyMed X-band and ENVISAT C-band SAR interferometry for landslides analysis. – *Remote Sensing of Environment*, **119** (1), pp. 272–285; New York.
- BOZZANO, F., CIPRIANI, I., MAZZANTI, P. & PRESTININZI, A. (2014): A field experiment for calibrating landslide time-of-failure prediction functions. – *International Journal of Rock Mechanics and Mining Sciences*, **67** (), pp. 69–77;
- BOZZANO, F., CIPRIANI, I., MAZZANTI, P. & PRESTININZI, A. (2011): Displacement patterns of a landslide affected by human activities: insights from ground-based InSAR monitoring. – *Natural Hazards*, **59** (3), pp. 1377–1396;
- BÜRGMANN, R., ROSEN, P. A. & FIELDING, E. J. (2000): Synthetic aperture radar interferometry to measure Earth’s surface topography and its deformation. – *Annual Review of Earth and Planetary Sciences*, **28** (), pp. 169–209;
- CASTELLARO, S. & MULARGIA, F. (2009): VS30 Estimates Using Constrained H/V Measurements. – *Bulletin of the Seismological Society of America*, **99** (2A), pp. 761–773;
- COLESANTI, C. & WASOWSKI, J. (2006): Investigating landslides with space-borne synthetic aperture radar (SAR) interferometry. – *Engineering Geology*, **88** (3-4), pp. 173–199; Amsterdam.
- CORSINI, A., FARINA, P., ANTONELLO, G., BARBIERI, M., CASAGLI, N., COREN, F., GUERRI, L., RONCHETTI, F., STERZAI, P. & TARCHI, D. (2006): Space-borne and ground-based SAR interferometry as tools for landslide hazard management in civil protection. – *International Journal of Remote Sensing*, **27** (12), pp. 2351–2369; London.
- CRUDEN, D. M. & VARNES, D. J. (1996): Landslide types and processes. – *Special Report - Transportation Research Board, National Research Council*, **247** () ed. by TURNER, A. K. & SCHUSTER, R. L., pp. 36–75;

- D'EFFREMO, M., DESIDERO, A., GARCIA MARTINEZ, M. F., GOTTARDI, G., RIC-CERI, G., SELLERI, A., SIMONINI, A. & TORSELLO, P. (2016): Analysis and monitoring fo a tunnelling-induced deep landslide reactivation. – In: AVERSA, S., CASCINI, L., PICARELLI, L. & SCAVIA, C. [eds.] (2016): Landslides and Engineering slopes. Experience, Theory and Practice Vol. 2, pp. 735–742; Naples (CRC Press).
- FERRETTI, A., PRATI, C. & ROCCA, F. (2001): Permanent scatterers in SAR interferometry. – *Ieee Transactions On Geoscience and Remote Sensing*, **39** (1), pp. 8–20; New York.
- FIALKO, Y., SIMONS, M. & AGNEW, D. (2001): The complete (3-D) surface displacement field in the epicentral area of the 1999 M(w)7.1 Hector Mine earthquake, California, from space geodetic observations. – *Geophysical Research Letters*, **28** (16), pp. 3063–3066;
- GRIFFITHS, J. S., BRUNSDEN, D., LEE, E. M. & JONES, D. K. C. (1995): Geomorphological Investigations For the Channel-tunnel Terminal and Portal. – *Geographical Journal*, **161** (), pp. 275–284;
- HANDWERGER, A. L., ROERING, J. J. & SCHMIDT, D. A. (2013): Controls on the seasonal deformation of slow-moving landslides. – *Earth and Planetary Science Letters*, **377–378** (1), pp. 239–247; Amsterdam.
- HANDWERGER, A. L., ROERING, J. J., SCHMIDT, D. A. & REMPEL, A. W. (2015): Kinematics of earthflows in the Northern California Coast Ranges using satellite interferometry. – *Geomorphology*, **246** (), pp. 321–333;
- HOOPER, A., ZEBKER, H., SEGALL, P. & KAMPES, B. (2004): A new method for measuring deformation on volcanoes and other natural terrains using InSAR persistent scatterers. – *Geophysical Research Letters*, **31** (23), p. L23611; Washington DC.
- HOOPER, A., SEGALL, P. & ZEBKER, H. (2007): Persistent scatterer interferometric synthetic aperture radar for crustal deformation analysis, with application to Volcan Alcedo, Galapagos. – *Journal of Geophysical Research-solid Earth*, **112** (B7), B07407; Washington DC.

- HOOPER, A. (2008): A multi-temporal InSAR method incorporating both persistent scatterer and small baseline approaches. – *Geophysical Research Letters*, **35** (16), p. L16302; Washington DC.
- HUNGR, O., LEROUEIL, S. & PICARELLI, L. (2012): Varnes Classification of landslide types, an update. – In: EBERHARDT, E., FROESE, C., TURNER, A. K. & LEROUEIL, S. [eds.] (2012): *Landslides and Engineering Slopes: Protecting Society through Improved Understanding* (Proceedings of the 11th international and 2nd North American symposium on landslides and engineered slopes, Banff, Canada, 3–8 June 2012, pp. 47–58; London (CRC Press).
- HUNGR, O., EVANS, S. G., BOVIS, M. J. & HUTCHINSON, J. N. (2001): A review of the classification of landslides of the flow type. – *Environmental & Engineering Geoscience*, **7** (3), pp. 221–238; College station.
- KAMPES, B. & USAI, S. (1999): “Doris: The delft object-oriented radar interferometric software” In: 2nd International Symposium on Operationalization of Remote Sensing, Enschede, The Netherlands vol. 16 Citeseer, 1999, p. 20.
- KONTOGIANNI, V., TZORTZIS, A. & STIROS, S. (2004): Deformation and failure of the Tymfristos Tunnel, Greece. – *Journal of Geotechnical and Geoenvironmental Engineering*, **130** (10), pp. 1004–1013;
- MARINOS, P. & HOEK, E. (2001): Estimating the geotechnical properties of heterogeneous rock masses such as flysch. – *Bulletin of Engineering Geology and the Environment*, **60** (2), pp. 85–92; Berlin.
- MARK, P., NIEMEIER, W., SCHINDLER, S., BLOME, A., HEEK, P., KRIVENKO, A. & ZIEM, E. (2012): Radar interferometry for monitoring of settlements in tunnelling. – *Bautechnik*, **89** (11), pp. 764–776;
- MASSONNET, D. & FEIGL, K. L. (1998): Radar interferometry and its application to changes in the earth’s surface. – *Reviews of Geophysics*, **36** (4), pp. 441–500;
- MAXWELL, J. C. (1959): Orogeny, gravity tectonics, and turbidites in the Monghidoro area, northern Apennine mountains, Italy. – *Transactions of the New York Academy of Sciences*, **21** (4), pp. 269–280;

- MAZZANTI, P., BOZZANO, F., CIPRIANI, I. & PRESTININZI, A. (2015): New insights into the temporal prediction of landslides by a terrestrial SAR interferometry monitoring case study. – *Landslides*, **12** (1), pp. 55–68;
- NAKAMURA, Y. (1989): A method for dynamic characteristics estimation of subsurface using microtremor on the ground surface. – *Railway Technical Research Institute, Quarterly Reports*, **30** (1);
- NOFERINI, L., PIERACCINI, M., MECATTI, D., MACALUSO, G., ATZENI, C., MANTOVANI, M., MARCATO, G., PASUTO, A., SILVANO, S. & TAGLIAVINI, F. (2007): Using GB-SAR technique to monitor slow moving landslide. – *Engineering Geology*, **95** (3-4), pp. 88–98;
- PANINI, F., BETTELLI, G. & PIZZIOLLO, M. [eds.] (2002): Note illustrative della carta geologica d'Italia alla scala 1:50.000: Foglio 237, Sasso Marconi. – 176 pp.; Firenze (S.EL.CA. s.r.l).
- PARCHARIDIS, I., LAGIOS, E., SAKKAS, V., RAUCOULES, D., FEURER, D., LE MOUELIC, S., KING, C., CARNEC, C., NOVALI, F., FERRETTI, A., CAPES, R. & COOKSLEY, G. (2006): Subsidence monitoring within the Athens Basin (Greece) using space radar interferometric techniques. – *Earth Planets and Space*, **58** (5), pp. 505–513;
- ROERING, J. J., STIMELY, L. L., MACKKEY, B. H. & SCHMIDT, D. A. (2009): Using DInSAR, airborne LiDAR, and archival air photos to quantify landsliding and sediment transport. – *Geophysical Research Letters*, **36** (), p. L19402;
- ROSEN, P. A., HENSLEY, S., PELTZER, G. & SIMONS, M. (2004): Updated repeat orbit interferometry package released. – *Eos Trans. AGU*, **85** (5), pp. 47–47; Malden.
- SANDWELL, D., MELLORS, R., TONG, X., WEI, M. & WESSEL, P. (2011): GMT-SAR: An InSAR Processing System Based on Generic Mapping Tools, URL: <http://www.escholarship.org/uc/item/8zq2c02m>; – retrieved 05.06.2016.
- SCHMIDT, D. A. & BÜRGMANN, R. (2003): Time-dependent land uplift and subsidence in the Santa Clara valley, California, from a large interferometric synthetic aperture radar data set. – *J. Geophys. Res.* **108** (B9), pp. 1–13; International.

- SORRISO-VALVO, M. (1995): Considerazioni sul limite tra deformazione gravitativa profonda di versante e frana. – *Memorie della Societa Geologica Italiana*, **50** (2), pp. 179–185; Roma.
- SPAUN, G (1979): Tunnelbau und Talzuschub. – *Rock Mechanics. Supplementum = Felsmechanik. Supplementum = Mecanique des Roches. Supplementum*, (8) ed. by MUELLER, L., pp. 333–347;
- THURO, K., EBERHARDT, E. & GASPARINI, M. (2001): Adverse tunnelling conditions arising from slope instabilities; a case history. – In: KUEHNE, M., EINSTEIN, H. H., KRAUTER, E., KLAPPERICH, H. & POETTLER, R. [eds.] (2001): *International conference on Landslides; causes, impacts and countermeasures*, pp. –; (Verl. Glueckauf, Essen).
- TOFANI, V., RASPINI, F., CATANI, F. & CASAGLI, N. (2013): Persistent Scatterer Interferometry (PSI) Technique for Landslide Characterization and Monitoring. – *Remote Sensing*, **5** (3), pp. 1045–1065;
- USAI, S. (2003): A least squares database approach for SAR interferometric data. – *Ieee Transactions On Geoscience and Remote Sensing*, **41** (4), pp. 753–760;
- WASOWSKI, J. & BOVENGA, F. (2014): Investigating landslides and unstable slopes with satellite Multi Temporal Interferometry: Current issues and future perspectives. – *Engineering Geology*, **174** (), pp. 103–138;
- [WWW-01]: OSSERVATORIO AMBIENTALE E SOCIO-ECONOMICO DELLA VARIANTE DI VALICO (2016): Monitoraggio a Ripoli, URL: <http://www.osservatoriovareiantedivalico.it>; – retrieved 22.06.2016.
- ZEBKER, H. A. & VILLASENOR, J. (1992): Decorrelation In Interferometric Radar Echoes. – *Ieee Transactions On Geoscience and Remote Sensing*, **30** (5), pp. 950–959; New York.
- ZISCHINSKY, U. (1969): Über Bergzerreissung und Talzuschub. – *Geologische Rundschau*, **58** (3), pp. 974–983; Berlin.

# 5 Deformation responses of slow moving landslides to seasonal precipitation in the Northern Apennines, measured by InSAR

**Authors:** Benedikt Bayer, Alessandro Simoni, Marco Mulas, Alessandro Corsini and David Schmidt

**Publication details:** Submitted to Geomorphology.

hhline multirow booktabs



## **Abstract**

Slow moving landslides are widespread geomorphological features in the Northern Apennines of Italy where they represent one of the main landscape forming agents. The lithology of the Northern Apennines fold and thrust belt is characterized by turbidites, also known as flysch, and chaotic clay shales. While flysch rocks host earthslides that occasionally evolve into flow like movements, earthflows are the dominant landslide type in chaotic clay shales. In the present work, we document the kinematic response to precipitation of landslides in these different lithologies using radar interferometry. The study area includes three river catchments that are located South of Bologna and Modena. Here the mediterranean climate is characterized by a first wet season in spring and a second one in autumn, separated by relatively dry summers and winters with moderate precipitation. We use SAR imagery from the X-band satellite COSMO SkyMed and from the C-band satellite Sentinel 1 to retrieve spatial displacement measurements between 2009 and 2016 for 25 landslides in our area of interest. We also document detailed temporal and spatial deformation signals for eight representative landslides, although high quality time series products were only obtained for the years 2013 and 2015. In spring 2013, long enduring rainfalls struck the study area and numerous landslide reactivations were documented by the regional authorities. During 2013, we measured higher displacement rates on the landslides in pelitic flysch formations compared to the earthflows in the clay shales. A general slow down on all landslide types during 2015. We analysed the temporal deformation signal of our eight representative landslides and compared the temporal response to precipitation. We show that earthslides in flysch formations accelerate faster than earthflows in chaotic clay shales and reach higher velocities, while the displacement signal in time remains smoother for the earthflows. Although we have no detailed porepressure measurements for the period of interest, the observed behaviour can be explained our view by the morphological and hydrological characteristics of the different landslide types. On the one hand landslide material and bedrock are more resistant for the earthslides in the flysch rocks which is why slopes can maintain higher angles. On the other hand, landslides in the flysch formations have often deeper slip surfaces, landslide material is more permeable and hence long persistent rainfall was necessary to saturate the landslide body, raise the

## 5 Deformation responses of landslides to seasonal precipitation

---

ground water to the ground surface and induce a variation in pore pressure that was sufficient to trigger displacement. Once in motion, higher displacement rates developed on the flysch landslides due to higher slope angles.

## 5.1 Introduction

In the Northern Apennines, slow moving landslides are among the most common landscape forming agents, in particular where mechanically weak rocks form the substrate (BERTOLINI et al., 2004; SIMONI et al., 2013). Most of these landslides failed in the past and exhibit slow deformation in their post failure stage. However, this slow motion may transition into high displacement rates, which is why these landslides represent a major natural hazard, that periodically causes damages to houses and infrastructure (BERTOLINI et al., 2005). Synthetic aperture radar interferometry (InSAR in the following) provides the possibility to assess deformations of these landslides on a regional scale and the technique was repeatedly used to infer spatio-temporal landslide displacement (COLESANTI et al., 2003; HILLEY et al., 2004; ROERING et al., 2005; IASIO et al., 2012; HANDWERGER et al., 2013; WASOWSKI & BOVENGA, 2014; HANDWERGER et al., 2015). HANDWERGER et al. (2013) and HANDWERGER et al. (2015) successfully measured seasonal deformation of large earthflows in a Northern Californian river catchment, that is characterized by melange type shales similar to those in the Northern Apennines. In this paper we present the results of an InSAR campaign that contain datasets derived from the X-band satellite COSMO SkyMed (CSK in the following) and the C-band satellite Sentinel 1A (Se1 in the following). CSK has a high spatial resolution of ca 3 m and a variable acquisition frequency, that in our case range from 16 to 30 days, while Se1 has a moderate spatial resolution of ca. 20 m and a high acquisition frequency of ca. 12 days. In this paper, we document the spatial deformation patterns of 25 landslides during the period 2013-2016 in three river catchments covering an area of ca. 3600 km<sup>2</sup>. Flysch rocks with high fraction of pelitic material and mélange type clay shales, both of which belong to the Ligurian Nappe of the Northern Apennines (BETTELLI & PANINI, 1992; PINI, 1999), are the two main lithologies that are affected by landsliding (BERTOLINI et al., 2005). During the spring 2013 the study area was struck by long enduring and intense rainfalls that caused severe damages due to landsliding in ca. 92 cases. 79 landslide reactivations were registered in pelitic flysch formations while 9 occurred in chaotic clay shales and only 4 were counted in other lithologies like coarse grained turbidites or marls (see also PIZZILOLO et al., 2013; PIZZILOLO et al., 2015).

In order to test if this different behaviour of the landslides in the two main lithologies is also observable in the InSAR derived displacement signals, we analysed morphological differences and similarities between landslides that yielded InSAR signals in different bedrock lithologies and compare their displacement history to climatic forcing. Seasonal trends and reactivation episodes are documented and discussed in detail for eight selected cases. We show that landslides in pelitic flysch formations exhibit temporal deformation patterns that correlate with periods of long persistent rainfall, while only weak seasonal trends are detected for landslides in clay shales.

### 5.2 Geological and geographical background

The Northern Apennines are a fold and thrust belt in Italy that formed due to the convergence of the European and Adriatic plates (BOCCALETTI et al., 1971; PICOTTI & PAZZAGLIA, 2008). Here, chaotic clay-shales with block in matrix fabric (PINI, 1999; VANNUCCHI et al., 2003) and deposits of turbidity currents, also known as turbidites or flysch (RICCI LUCCHI, 1986), are the most common lithologies. In particular the tectonically shearded formations of the Ligurian Unit have poor geomechanical characteristics and are prone to slope instability (BERTOLINI et al., 2005). In zones where clay shales form the substrate, earth-flows with distinct source, transport and deposition zones are the dominant typology of slope failure (SIMONI et al., 2013). Where the slopes are composed of pelitic flysch, a broader spectrum of landslide types can be observed, but often the failures have characteristics of translational or rotational earth- or rockslides in the upper portions of the landslide body and may propagate as earthflow down-slope (BORGATTI et al., 2006; CORSINI et al., 2006). Radiocarbon dating showed that most of the failures are reactivations of old dormant landslides that formed during the Holocene and in climatic conditions that differ from the present situation (BERTOLINI et al., 2004).

Today the Northern Apennines have a Mediterranean climate and total annual precipitation reaches on average 1300 to 1400 mm (BERTI et al., 2012). The temporal pattern is characterized by intense precipitations in spring and autumn, separated by dry summers and winter months with moderate precipitation (TOMOZEIU et al., 2000; TOMOZEIU et al., 2002; PAVAN et al., 2008). For the years 2000 until 2012, the total rainfall for the spring period between February and March remained

typically below 300 mm ( $\mu = 288.3$  mm,  $\sigma = 70.8$  mm) and maximum daily intensities rarely exceeded 40 mm/day ( $\mu = 35.18$  mm/day,  $\sigma = 13.54$  mm/day for the years 2000-2012). However, in our study area total spring rainfall accumulated to 532 mm in 2013, 426 mm during 2014 and 384 mm during 2015. Also maximum daily intensities were with 41 mm/day (2013), 40 mm/day (2014) and 39.181 mm/day (2015) higher than those during 2000-2012.

Although many landslides in the area of interest show empirical relationships between deformation and precipitation (BERTI et al., 2012), this relationship is often only clear on long temporal timescales (BORGATTI et al., 2006; RONCHETTI et al., 2007). Moreover surface deformation varies often for different areas of the landslide body (IVERSON & MAJOR, 1987; PETLEY et al., 2005) and the hydrological, hydrogeological conditions on a slope can be complex (CERVI et al., 2012), which is why a simple relationship between deformation and precipitation might not exist.

## 5.3 Materials and Methods

### 5.3.1 InSAR processing details

In the last decades, InSAR has advanced as an efficient tool to measure displacements of the ground surface that range from few millimeters to several decimeters (MASSONNET & FEIGL, 1998; BÜRGMANN et al., 2000). Due to decorrelation of the signal in rural areas, several advanced processing techniques were developed, the two most common of which are termed Persistent Scatterer interferometry (PS-InSAR, FERRETTI et al., 2001; ADAM et al., 2004; HOOPER et al., 2004) and Small Baseline interferometry (SBAS, BERARDINO et al., 2002; SCHMIDT & BÜRGMANN, 2003; USAI, 2003). The most recent evolutions of this techniques aim to combine the advantages of both approaches in order to maximise the quality of the final post-processed results (FERRETTI et al., 2011; HOOPER, 2008; HOOPER et al., 2012).

In the present work, we use the Small baseline implementation of the Stanford Method of Persistent scatterers (HOOPER et al., 2007; HOOPER, 2008) to post-process our interferometric results. We used DORIS (KAMPES & USAI, 1999) and ROI-PAC (ROSEN et al., 2004) to process the SAR data from the ASI COSMO SkyMed constellation, while we used GMTSAR (SANDWELL et al., 2011) for the processing of Sentinel 1A. A high resolution digital surface model (2 m) derived

## 5 Deformation responses of landslides to seasonal precipitation

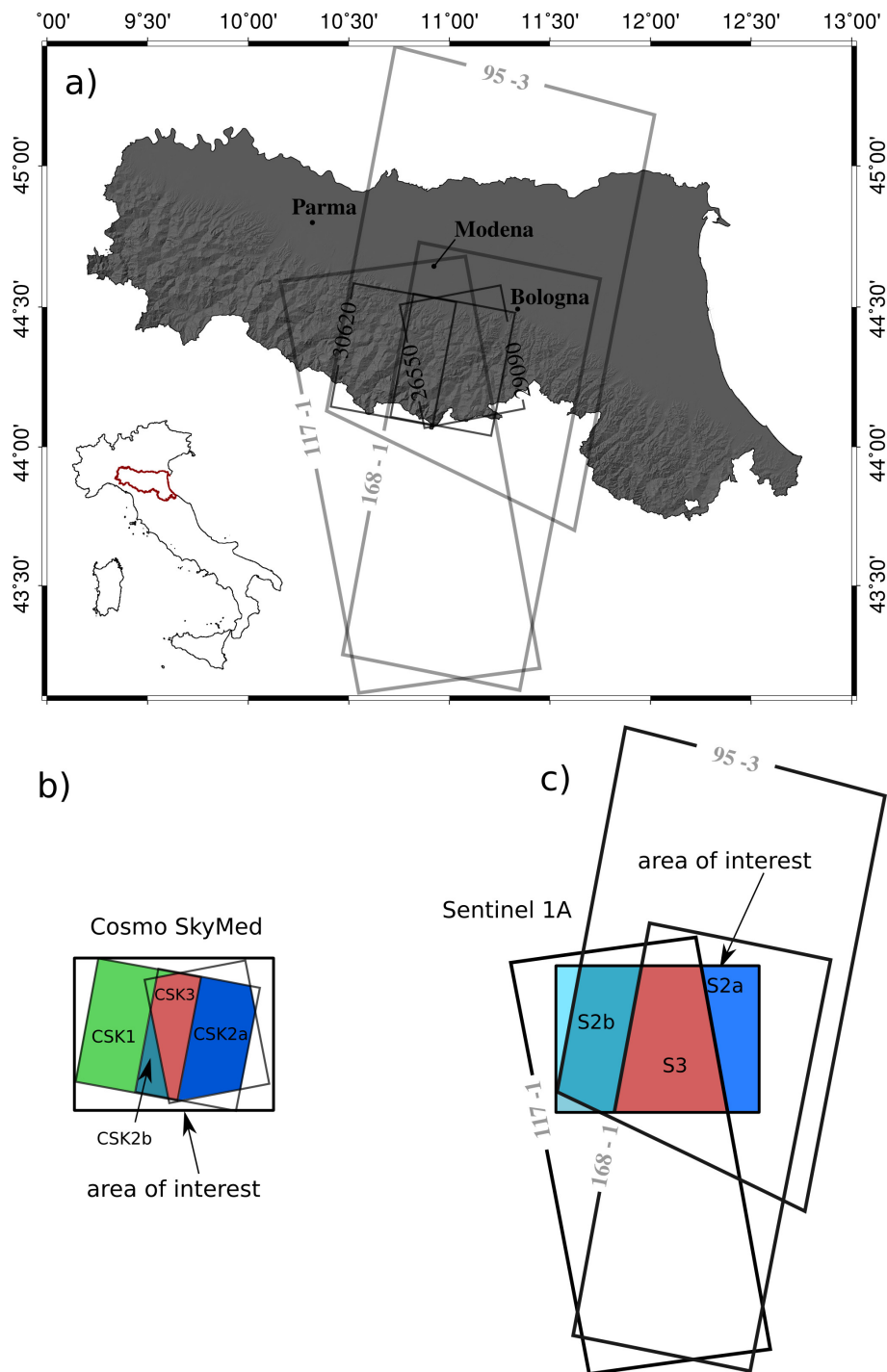


**Figure 5.1:** a) The area of interest is located in the Northern Apennines of Italy and is covered by several SAR frames in both ascending and descending viewing geometries. b) For COSMO SkyMed one ascending and two descending swaths were available. A small area is covered by all three datasets (CSK3), while most parts of our study area are covered by either two (CSK2a and CSK2b) or one dataset (CSK1). c) Also for Sentinel 1A one ascending and two descending tracks were processed, which results in a larger area covered by either two (S2a and S2b) or three InSAR datasets (S3). Details regarding the different datasets and their combination can be found in Tab. 5.1.

## 5 Deformation responses of landslides to seasonal precipitation

**Table 5.1:** Detailed information about single and combined InSAR datasets. *I*figs. is an abbreviation for interferograms

Combined dataset	Combined Ifigs./scenes	Direction	Orbit	No. of Ifigs./scenes	Sampling frequency (days)	Period
CSK 3	112/63	desc.	29090	29/16	16 to 224	31.01.'13–10.3.'15
		asc.	26550	45/25	16 to 272	22.06.'11–24.01.'15
		desc.	36020	51/22	16 to 48	29.09.'12–16.12.'13
CSK 2 a	89/54	asc.	26550	60/38	16 to 272	25.12.'09–25.02.'15
		desc.	29090	29/16	16 to 224	31.01.'13–10.3.'15
CSK 2 b	96/47	asc.	26550	45/25	16 to 272	22.06.'11– 24.01.'15
		desc.	36020	51/22	16 to 48	29.09.'12– 16.12.'13
CSK 1	51/22	desc.	36020	51/22	16 to 48	29.09.'12–16.12.'13
S3	229/80	asc.	117	115/41	12 to 24	13.10.'14– 23.5.'16
		desc.	168	72/26	12 to 24	22.3.'15– 27.5.'16
		desc.	95	42/13	12 to 36	12.10.'14– 27.5.'16
S2a	187/67	asc.	117	115/41	12 to 24	13.10.'14– 23.5.'16
		desc.	168	72/26	12 to 24	22.3.'15– 27.5.'16
S2b	157/54	asc.	117	115/41	12 to 24	13.10.'14– 23.5.'16
		desc.	95	42/13	12 to 36	12.10.'14– 27.5.'16

from aerial photos acquired in 2008 is available for our study area and was used to calculate and subtract the topographic phase from the interferograms.

Interferograms cover large areas and often whole mountain ranges (e.g. MASSONNET & FEIGL, 1998; BÜRGMANN et al., 2000), while single landslides produce local deformation signals in interferograms (e.g. ROERING et al., 2005; COLESANTI & WASOWSKI, 2006; HANDWERGER et al., 2013; WASOWSKI & BOVENGA, 2014). Since the landslide density in our study area is high, we are interested in both large scale information, like the detection of landslides as well as local aspects of the signal, like deformation time series for different parts of our landslides. We first used large spatial subsets of our interferometric results in order to identify clear signals that were caused by landsliding. We considered a line of sight signal to be attributed to a landslide if a consistent gradient is observed between neighbouring pixels that are not separated by rivers or ridges (ROERING et al., 2005). Then, we reprocessed local subsets of the interferograms that include single landslide cases and calibrated the processing parameters to suite the specific landslide under analysis.

### 5.3.2 Combining interferograms from different orbits

COSMO SkyMed acquires SAR imagery on two descending tracks and one ascending orbit over our area of interest (Fig. 5.1 a and b). The TopSAR acquisition mode of Sentinel acquired each SAR frame in three subswaths. We processed SAR imagery from three tracks over our study area (Fig. 5.1 a and c), one of which is acquired in ascending geometry (orbit 117 subswath 1), and two are acquired in descending geometry (orbit 95, subswath 3 and orbit 168 subswath 1). Often a given area of interest is covered by more than one swath and one viewing geometry, which is why interferograms from different orbits with different look angles can be combined. As a consequence different parts of our study area are covered by more than one combined InSAR dataset (different colours in Fig. 5.1 b and c). Details regarding the number of scenes, interferograms and temporal coverage of single and combined InSAR datasets are reported in Tab. 5.1. The acquisition frequency of COSMO SkyMed was variable throughout all datasets. For example during the period of 2013 acquisition frequency was high and almost every 16 days an image was available (Tab. 5.1). However, during the year 2014 data gaps of more than 200 days are present in both datasets over the eastern part of the study area. For Sentinel the acquisition frequency was more stable and generally the scenes are available at an interval of 12 days with some minor gaps of 36 days.

InSAR measures range increases or decreases along the satellite line-of-sight, which corresponds either to a movement away or towards the satellite. This reference coordinate system is not intuitive for scientists that are not familiar with radar interferometry. The availability of different viewing geometries and different look angles allows theoretically the estimation of the displacement vectors in three dimensions (WRIGHT et al., 2004). For landsliding, a common way of representing the InSAR derived displacements, is to back-project the measurements in the down-slope direction (e.g. HILLEY et al., 2004; HANDWERGER et al., 2013; HANDWERGER et al., 2015). This approach requires a DEM to calculate slope and aspect information for a given pixel in order to construct a down-slope unit vector. Then interferograms can be back-projected from the satellite coordinate system onto the down-slope unit vector. If more than one InSAR dataset is covering a given area of interest, we choose pixels that are common to all datasets. We modified one date at the beginning of each dataset, in order to have one common date in all datasets

and form a closed interferogram network. The date was chosen in order to minimize the period (less than 10 days) between the modified date and the original dates in the different datasets. Then we solved for the displacements in the single timesteps using the inversion implemented in StaMPS (HOOPER, 2008). This approach yields a series of combined downslope projected InSAR datasets which are listed Tab. 5.1. Their spatial coverage is illustrated in Fig. 5.1 b and c.

One advantage of combined InSAR datasets is that the sampling frequency is higher and that the timesteps are covered by a higher number of observations. For example, during the period of 2013 the COSMO SkyMed datasets have sampling frequencies that range from 16 to 48 days in the different orbits. After the combination of the interferograms the average acquisition rate of the combined dataset is 11 days, with values ranging from 1 to 36 days. For Sentinel, the sampling rate is generally 12 days before interferograms are combined and reach on average 8 days after inverting the back-projected interferograms from different orbital tracks. Also, this approach presents a convenient way to represent results obtained from different orbits. On the other hand, it can only be applied to pixels that are common to all datasets and hence the spatial detail present in a single viewing geometry is reduced. Two other problems are the presence of high frequency noise in the inverted time series results and a speckle like pattern in space. Parts of the high frequency artefacts in time are caused by atmospheric noise, instability in the inversion as well as differences between down-slope and the real displacement vector (SCHMIDT & BÜRGMANN, 2003; HANDWERGER et al., 2015). The speckle pattern in the velocity maps derive in our view from the difference in pixel positioning. We used a local regression filter (lowess, CLEVELAND, 1979; CLEVELAND & DEVLIN, 1988) to smooth the signal in time and a gaussian low pass filter to remove high frequency noise in space. Since COSMO SkyMed and Sentinel results rarely overlap in time and the position of the scatterers are often different, we treated the two datasets separately.

## **5.4 InSAR results at the catchment scale**

### **5.4.1 Morphology of InSAR-detectable landslides**

Both, chaotic clay shales and pelitic flysch formations have a high landslide density, and the majority of slopes are affected by slope instabilities (BERTOLINI et al., 2005;

## 5 Deformation responses of landslides to seasonal precipitation

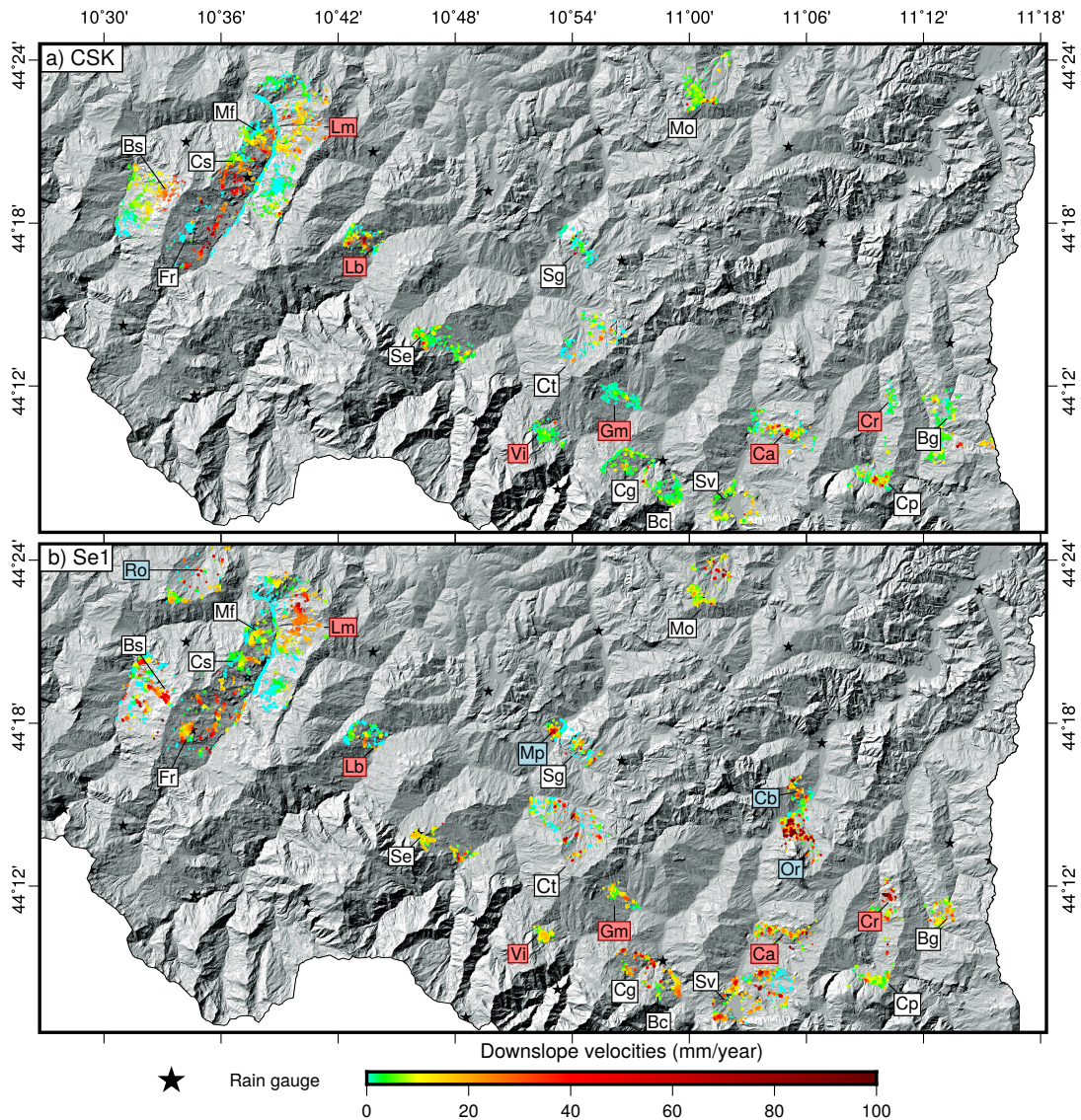


**Figure 5.2:** a) Calibrated InSAR results for all landslides that caused a clear deformation signal in the COSMO SkyMed datasets. Black stars indicate rain gauges that were used to retrieve regional rainfall that will be discussed together with displacement signals in section 4.2. b) Calibrated InSAR results for Sentinel 1A. The labels in a) and b) are localities, where distinct landslides were detected. From West to East and from South to North we have: Bs: Boschi di Valoria, Fr: Frassinoro, Cs: Casolare, Ro: Roncolo, Mf: Montefiorino, Lm: Lama di Monchio, Lb: La Borra, Se: Sestola, Vi: Vidiciatico, Sg: San Giacomo, Gm: Gaggio Montano, Ct: Castelluccio, Bc: Borgo Cappanne Mo: Monte Ombraro, Sv: Suviana, Ca: Camugnano, Cp: Castiglione dei Pepoli, Cr: Creda, Bg: Il Borgo. Red highlighted labels indicate selected landslide cases that are discussed in detail in section 5.5. Blue labels are cases that were only visible in the Sentinel dataset.

BERTI et al., 2012). We identified 25 landslides in 22 different localities that are associated to clear interferometric signals either in the CSK (Fig. 5.2 a) or the Se1 products (Fig. 5.2 b). Most cases are present in both datasets and only 3 landslides did not yield any signal for CSK (blue font in Fig. 5.2). We remapped the perimeters of the identified landslides, based on the topographic map, a regional digital elevation model, and aerial photography. All of the registered landslides are mapped in the regional landslide inventory (SERVIZIO GEOLOGICO, SISMICO E DEI SUOLI DELLA REGIONE EMILIA-ROMAGNA, 2014). InSAR displacement patterns are visible for 13 landslides in pelitic flysch formations and 12 landslides in chaotic clayshales.

We analysed the morphometric characteristics of the InSAR-detectable landslides in the two main lithologies (Fig. 5.3) and found that differences can be observed in particular with respect to width, length, area and slope angles of the landslides. Landslide length varies between 1100 m to 3360 m in flysch formations (mean: 2137 m), while landslides in the chaotic clay shales can be longer with landslide lengths ranging from 750 m to 3700 m (mean: 2137 m, Fig. 5.3 a). On the other hand, the slope failures in flysch are typically wider (mean: 1566 m, var: 600 m to 3600 m) than their equivalents in the chaotic clay shales (mean: 567 m, var: 196 m to 1450 m Fig. 5.3 b). Due to their larger variance in width, pelitic flysch landslides cover larger areas (mean: 3.06 km<sup>2</sup>, var: 0.16 km<sup>2</sup> to 10 km<sup>2</sup>) compared to the those in clay shales (mean: 1.2 km<sup>2</sup>, var: 0.12 km<sup>2</sup> to 4.34 km<sup>2</sup>, Fig. 5.3 c). Slope angles on landslide prone terrain in chaotic clay shales reach on average 11 degrees (var: to 15.5), while slopes in pelitic flysch formation maintain on average angles around 12.4 degrees (var: 9.5 to 14.9, Fig. 5.3 d). If we use slope angle as a proxy for mechanical properties of both bedrock and regolith, we can infer that chaotic clayshales have lower shear resistance than pelitic flysch. Comparing landslide width and length (Fig. 5.3 e), it can be stated that landslides in the pelitic flysch units can become wider with respect to their length and as mentioned earlier, are often complex landslides with characteristics of both rotational and translational sliding that may transition to classical earthflows. Since they are often composed by numerous geomorphological units or minor nested landslides and the mechanical properties correspond to a soil rather than a rock, they can often be classified as complex earthslides (CRUDEN & VARNES, 1996). On the other hand the InSAR detectable landslides in the clay shales have lower width/length ratios, and in most cases they exhibit a bowl-shaped source area, an elongated transport zone and a lobate toe,

which is why they can be classified as earthflows (CRUDEN & VARNES, 1996; HUNGR et al., 2001; HUNGR et al., 2012). Fig. 5.3 e shows however that certain slides in the chaotic clay shales can exhibit similar width/length ratios to those encountered in the pelitic flysch units. Hence, despite the different bedrock lithologies similar landslide types may occur in both clay shales and flysch formations.

We detected no clear InSAR signal on landslides that were smaller than approximately 500 m in width or length. In our experience, deformation of small landslides do not cause clear phase gradients in interferograms and although sparse groups of pixels can be identified on small landslides, their spatio-temporal signals are often ambiguous.

### 5.4.2 Differences in spatial displacement patterns

We analysed the mean velocities of all pixels that were located inside our selected landslides for two different periods. The first period is covered by COSMO SkyMed (2009 to 2015) and includes the aforementioned long enduring rainfall events of the years 2013 and 2014. Our Sentinel dataset covers the period between autumn 2014 and summer 2016.

If all pixels inside mapped landslide perimeters are considered, a certain number of stable pixels are always found on the large landslides. We generally found an increasing number of pixels in stable portions with increasing landslide area. These stable pixels bias the frequency distribution of velocities. To overcome this problem, we decided to use the 75th percentile of the inferred downslope velocity (Fig. 5.3 f) on a single phenomena (maximum velocity in the following), because we believe that it is a better indicator of the displacement rate attained by the movement and because it is not significantly influenced by the abundance of stable pixels.

During the year 2009-2014 (COSMO SkyMed) numerous pixels with mean velocities ranging from 20 to 40 mm/a were registered on the complex landslides of the flysch formations and only single pixels report mean velocities higher than 50 mm/a (Fig.5.3 f). On the landslides in the clay shales, pixels with lower mean velocities prevail and again only single pixels move faster than 50 mm/a. During the Sentinel era (2014-2016), the shape of the distribution changes and the differences between the landslide types vanish (Fig.5.3 f). In both cases more pixels with higher mean velocities were registered, which reflects in our view the capacity of a C-band

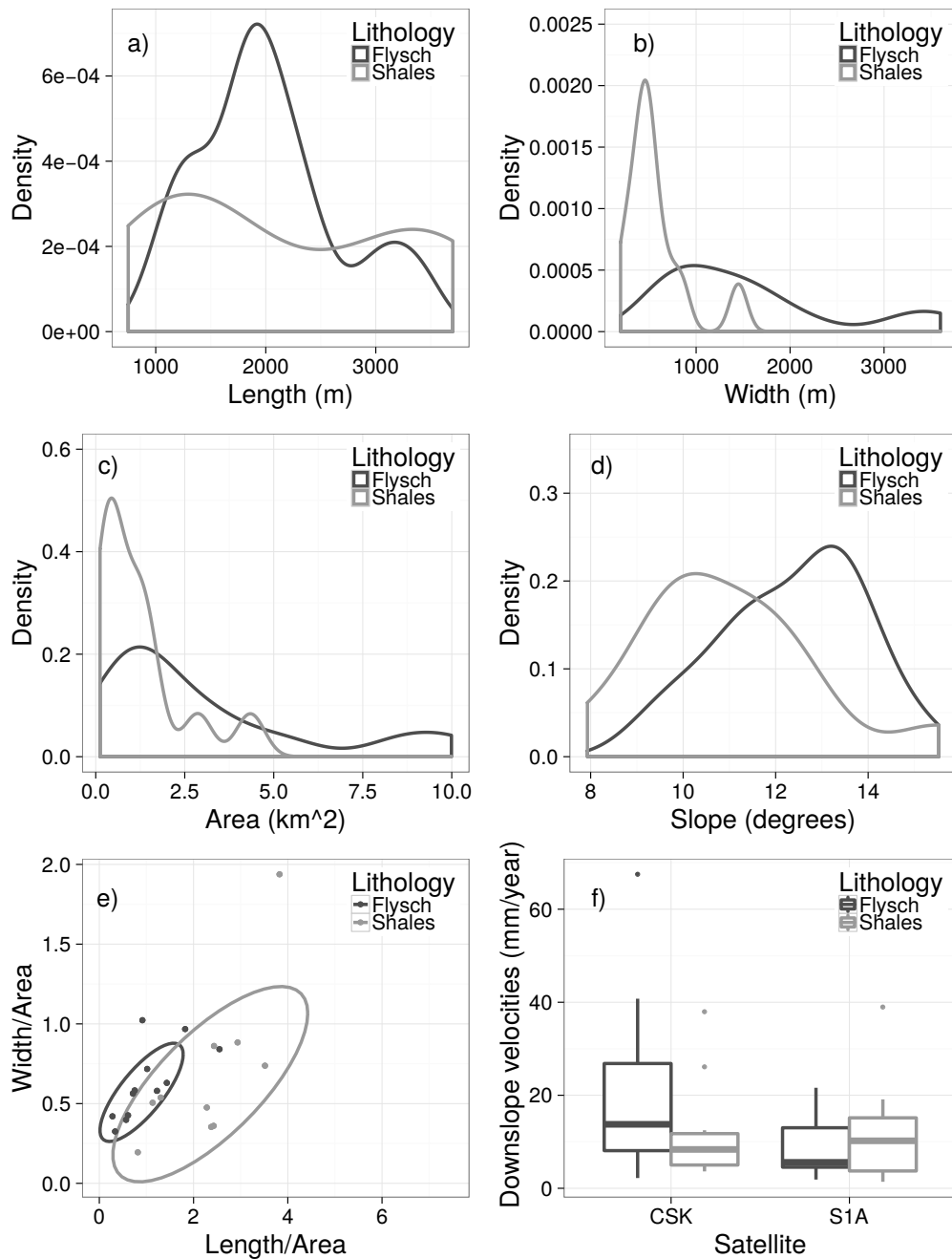


**Figure 5.3:** Density distributions calculated with a gaussian kernel of a) landslide lengths, b) widths, c) area, d) slope angles and e) the relationship between width and length, normalized by the landslide area for InSAR detectable landslides in our study area for the two main lithologies. f) 75 percentile of the mean downslope velocities measured on the landslides in pelitic flysch formations and chaotic clay shales

radar with high acquisition frequency to resolve higher displacement rates. In the CSK dataset (2009-2014) maximum velocities of flysch earthslides are higher than those registered on clay-shale earthflows and slowed down in the Sentinel dataset (2014-2016). Maximum earthflow velocities remained more stationary throughout all datasets, although the variance is higher for Sentinel (Fig. 5.3 f), which reflects again the technical advantage of Sentinel in vegetated areas with sparse groups of houses.

## 5.5 Kinematics of selected landslides

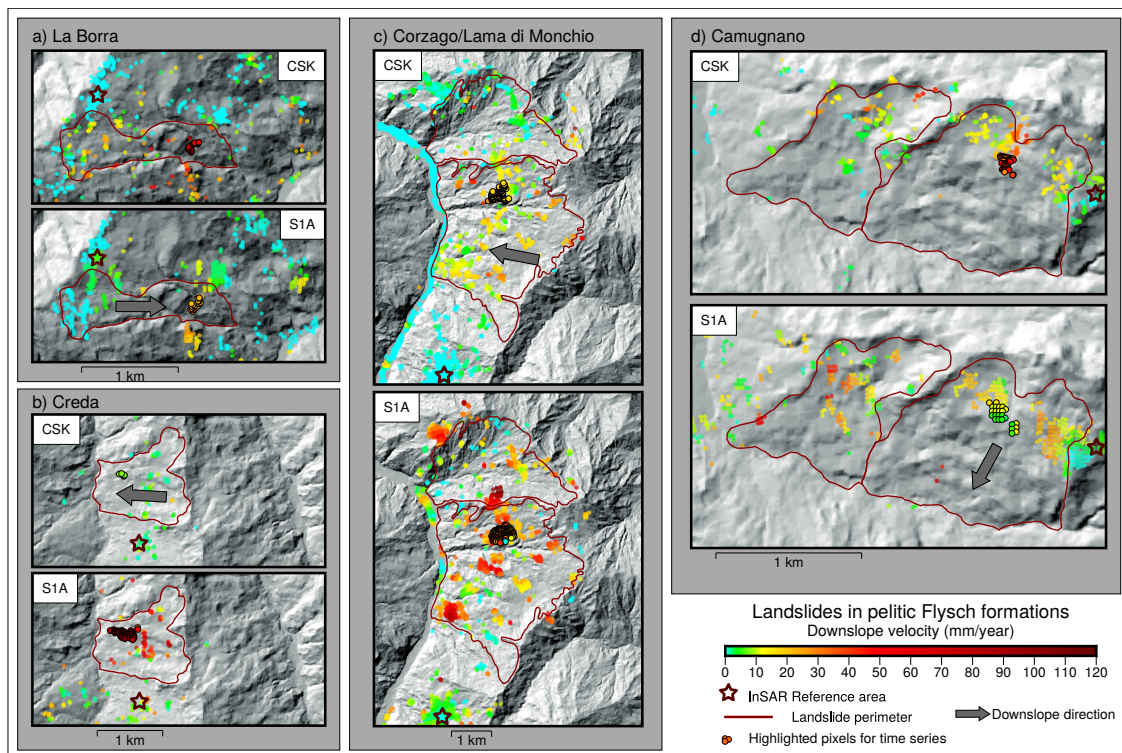


**Figure 5.4:** Deformation maps for selected rockslides in pelitic flysch formations. CSK and S1A results a) at La Borra, b) at Creda, c) at Corzago/Lama di Monchio, d) at Camugnano. Due to the high spatial resolution, the number of registered pixels are higher for COSMO SkyMed, yet Sentinel selects also points in areas, where COSMO SkyMed was decorrelated. Displacement patterns vary in space for the different periods and the highlighted pixels were used to produce the time series in Fig. 5.6 a) and d)

### 5.5.1 Local variations of different landslide types

Due to regional differences in mechanical characteristics of host rock, landslide material as well as local variations in precipitation, landslides may display a large range of kinematics. Here, we document eight selected cases, four of which involve pelitic flysch formations and four involve the chaotic clay shales. In order to exclude the possibility that our temporal deformation patterns are biased by our InSAR dataset, we chose these cases in different parts of our study area that are covered by different interferometric datasets. This excludes the possibility that our temporal displacement signals are biased by the dataset. Also, they are representative of the morphometric variability discussed in the previous section and can be considered representative for the study area.

La Borra is a large complex landslide exhibiting prevailing sliding in the upper part and flow-like morphology in the lower part (Fig. 5.4a). Creda (Fig. 5.4b) and Camugnano (Fig. 5.4d) are isometric deep-seated landslides, while Corzago/Lama di Monchio (Fig. 5.4c) is a large landslide complex whose width/length ratio is unusually high (ca. 1.5). The cases of La Borra and Camugnano illustrate well the change from high mean velocities during 2013 (CSK dataset) to lower displacement rates during 2015 (Sentinel dataset). In both cases the selected pixels are located in the most active part of the landslide body and the signal in the different dataset is most likely measured on the same physical objects on the ground. On the other hand, the cases of Creda and Corzago/Lama di Monchio show that Sentinel selects more pixels in rural areas and can better resolve locally high displacement rates. These high velocities are not caused by an acceleration of the landslide bodies, but by the technical differences between CSK and Sentinel. In our view it is possible that here displacement rates were even higher during 2013 (CSK), but were not fully resolved by the X-band satellite.

The four representative earthflows are reported in Fig. 5.5. Vidiciatico (Fig. 5.5a) and Gaggio Montano (Fig. 5.5b) are medium sized phenomena, while Monte Ombraro (Fig. 5.5c) and Sestola (Fig. 5.5d) are large earthflows. All of them exhibit the distinctive morphological features of apenninic earthflows (Simoni et al., 2013) with characteristic source area and accumulation zones. For the sake of this work (Fig. 5.5), we mapped the entire earthflow complex as a whole although multiple coalescent earthflows can be further recognized and separately mapped on a geomor-

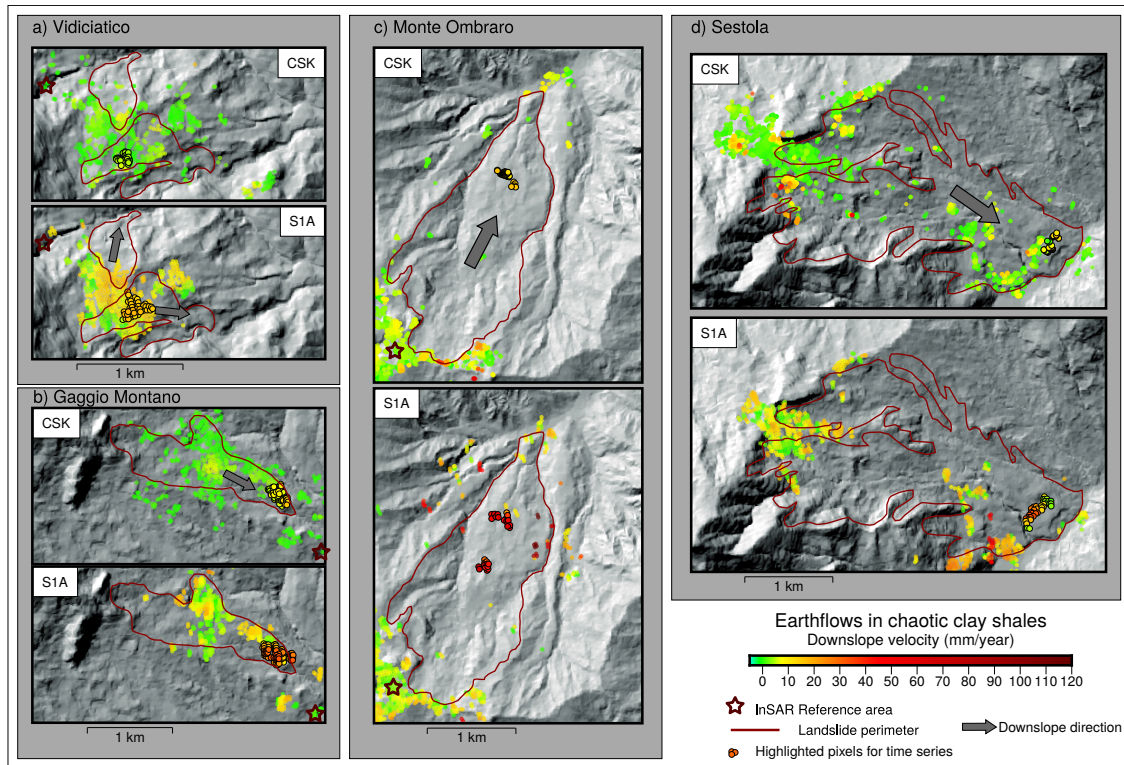


**Figure 5.5:** Deformation maps for selected earthflows in pelitic flysch formations. CSK and S1A results a) at Vidiciatico, b) at Gaggio Montano, c) at Monte Ombraro, d) at Sestola. Again, the highlighted pixels were used to produce the time series in Fig. 5.6 b) and e)

phological basis. At Vidiciatico and Gaggio Montano, the signal appears consistent throughout all datasets. In the case of Gaggio Montano, slow displacement rates were measurable also in older InSAR datasets (CORSINI et al., 2006) and confirm the sustained slow movement typical of these phenomena. The comparison between COSMO SkyMed and Sentinel datasets indicate that locally higher mean velocities are measured with the C-band satellite. This difference is well visible in the central and lower parts of Monte Ombraro (Fig. 5.5 c) and Sestola (Fig. 5.5 d).

### 5.5.2 Deformation responses to long enduring rainfall events

Landslides are complex hydrological systems and, as a consequence, a simple relationship between precipitation and displacements is rarely evident (e.g. CERVI et al., 2012; BERTI et al., 2012; BOGAARD & GRECO, 2016). Still, rainfall, infiltration and the resulting variation in pore pressures can be considered the main drivers of landslide motion (e.g. IVERSON, 2000; BERTI & SIMONI, 2012; BERTI et al., 2012;

HANDWERGER et al., 2013). In the following, we document the velocity time series of the highlighted pixels in Fig. 5.4 and Fig. 5.5 together with rainfall derived from rain gauges that are distributed over our study area (Fig. 5.2 a).

We report the velocity time series during 2013, because the sampling frequency was high for all CSK datasets (Fig. 5.6 a and b) and 2015 (Fig. 5.6 d and e), because all cases were covered completely by all Sentinel datasets. The rainfall data from all rain gauges was averaged for each day in order to obtain a mean value for the study area. Since our combined displacement measurements have average temporal sampling rates between 8 (Se1A) and 12 (CSK) days maximum time spans between acquisition of up to 36 days, we compared 20 days cumulated rainfall to our displacement measurements (black lines in Fig. 5.6 c and f). We also compared displacement rates to rainfall events as defined by BERTI et al. (2012) (grey bars in Fig. 5.6 c and f). Landslides in chaotic clay shales and pelitic flysch. First, peak velocities are higher for most flysch landslides during Spring 2013, reaching values up to 30 mm per month in the downslope direction (Fig. 5.6 a), while peak velocities in the earthflows remain below 8 mm/month (Fig. 5.6 b). Second, the displacement rates of the earthflows accelerate and decelerate more smoothly compared to gravitational movements in the flysch formations. The higher peak velocities in flysch landslides are consistent with the general trend observed in the overall higher velocities that were measured during this period for all flysch landslides in the study area. One exception is the case of Corzago/Lama di Monchio, which for the year 2013 shows displacement signals that do not exceed 8 mm/month, similar to those obtained on the earthflows.

During the year 2013 persistent rainfalls started by the end of January (Fig. 5.6 c) which increased displacement rates only at La Borra and Camugnano, while the velocities on the other landslides did not increase (Fig. 5.6 a). April 2013 was characterized by sustained rainfalls spanning 35 days, which define a single event characterized by moderate intensity (ca. 8 mm/day) but high absolute precipitation (ca. 270 mm, Fig. 5.6 c). This rainfall event caused notable accelerations on most of the flysch landslides. The first landslide to respond to these rainfalls was Camugnano, followed by La Borra and Creda, while Corzago/Lama di Monchio did not show any increase in displacement rate. It is worth to recall that the discussed landslides are spread over a relatively large territory (3600 km<sup>2</sup>) and that they are covered by different datasets. Still, the observed InSAR signals are coherent and often synchro-

## 5 Deformation responses of landslides to seasonal precipitation

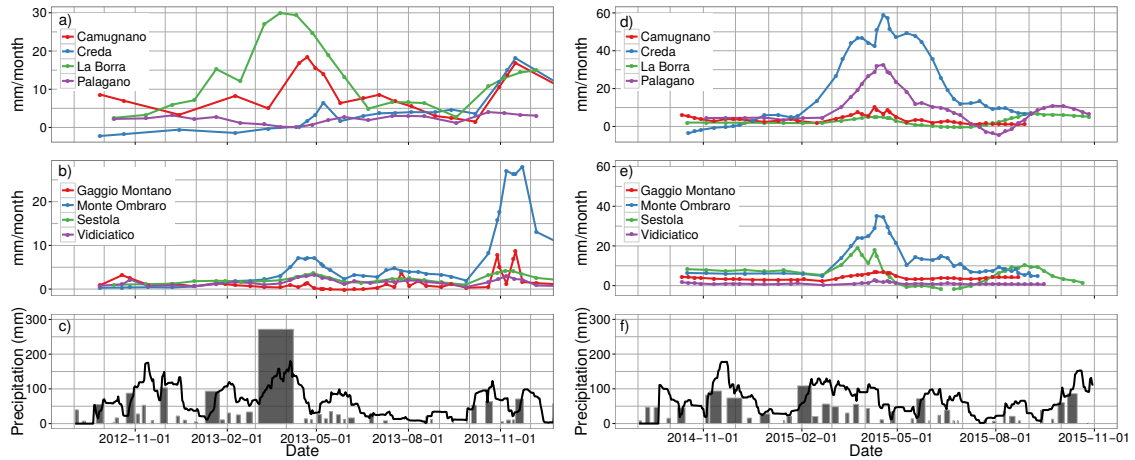


**Figure 5.6:** a) Velocity time series for landslides in pelitic flysch during for the year 2013. b) Velocity time series for earthflows in the chaotic clay shales for 2013. c) The black line are daily rainfalls that take into account the preceding twenty days of precipitation. The grey bars are rainfall events that were defined by the methodology proposed by BERTI et al. (2012). d) Displacement rates derived from Sentinel for the year 2015 on rockslides in flysch. e) Velocity time series for earthflows in mélange type rocks. f) Daily precipitation with rainfall of the preceding 20 days and rainfall events for the year 2015.

nized, which demonstrates in our view the relationship between acceleration and climate forcing. For all landslides that show an increase in displacement rate, peak velocities are reached between 20 and 60 days after the onset of the long rainfall event in April. The lag to peak velocity is consistent with the observations made by HANDWERGER et al. (2013) on slow moving earthflows in mélange type rocks of Northern California. We believe that this lag is not surprising for deep seated landslides, because different processes like surface infiltration and pressure diffusion (IVERSON, 2000), as well as the saturation of fissures (KRZEMINSKA et al., 2012) can delay the increase in porepressure.

During the spring 2015, total recorded rainfall resulted lower than the two previous years and also single rainfall events never reached magnitudes similar to the April 2013 event. However, the trend of cumulated 20 days rainfall shows that the wet season started in mid January with major rainfall events in January and February (Fig. 5.6f). Cumulated precipitation remained high until May, although rainfall was interrupted by several dry days. The displacement signals registered on landslides confirm the lithology-dependent variability described above. Higher peak velocities and accelerations are found on flysch landslides while the seasonal displacement rates resemble smoothly the pattern of the cumulated 20 days precipitation (black line

in Fig. 5.6f) for all landslides in clay shales. Those accelerating during spring 2015, reacted also after the precipitation events in January and February. If we consider the January event as the onset of the precipitation, the lag to peak landslide velocity is 20 to 60 days also in early 2015.

### 5.5.3 Relationship between deformation response and precipitation

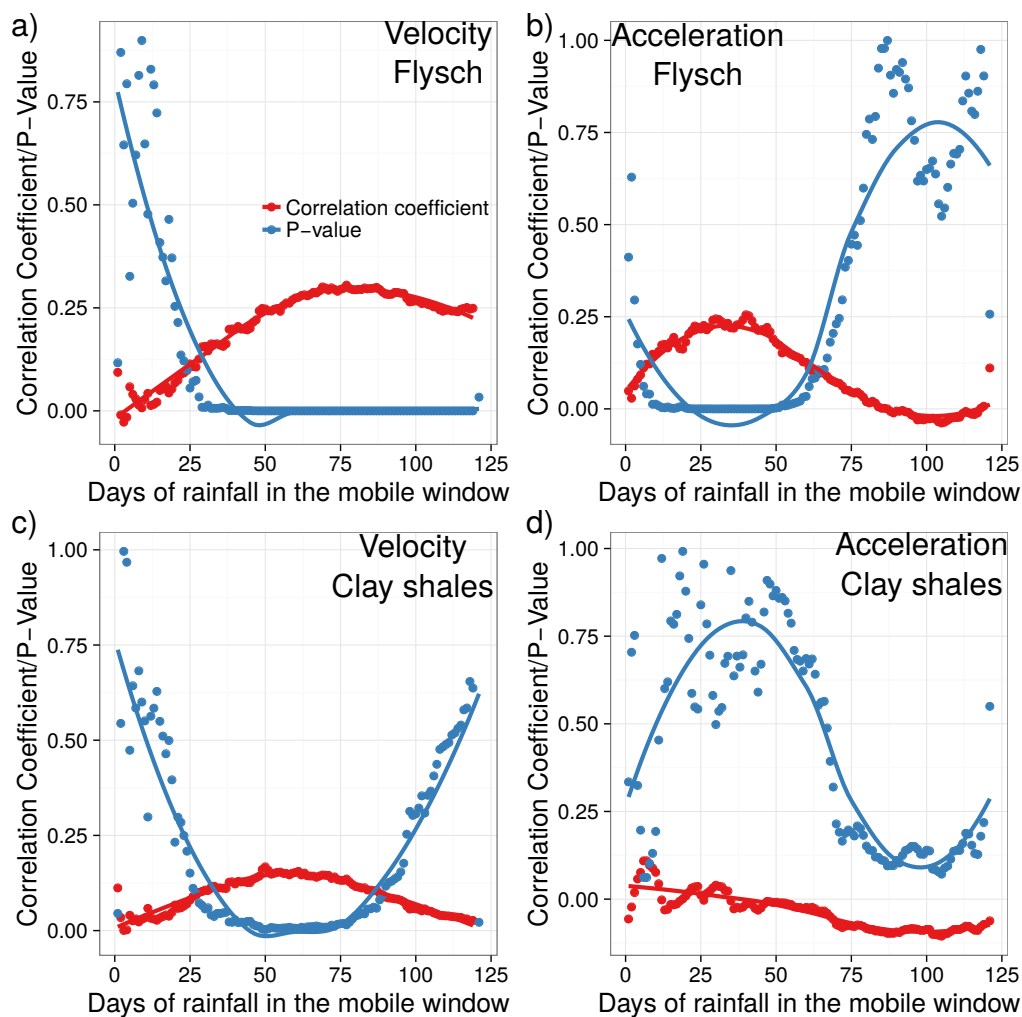


**Figure 5.7:** Correlation coefficients and  $P$ -values for the relationships between a) Velocity and precipitation and b) Acceleration on landslides in pelitic flysch formations and different days of preceding rainfall added to the daily precipitation values. c) Correlation coefficients and  $P$ -values for the relationship between Velocity and d) Acceleration on landslides in chaotic clay shales.

Mechanical aspects, like the tendency of the sheared clay material to contract or dilate (IVERSON, 2005) or hydrological aspects like the development of effective drainage pathways in time (BOGAARD & GRECO, 2016) impose non linearities on the relationships between precipitation, porepressure and displacement. COROMINAS et al. (2005) showed that the relationship between displacement rate and pore pressure is not linear and can be approximated by a third degree polynomial. MASSEY et al. (2013) have shown a high correlation between precipitation and pore pressure exists if more than 30 days of preceding rainfall is taken into account. CORSINI & MULAS (2016) reported that, adding the antecedent 40 days of rainfall to each precipitation cause high correlation between velocity measurements and precipitation on a Northern Apennines rock slide.

We tested the relationship between acceleration/velocity and rainfalls for different periods of antecedent rainfall (Fig. 5.7). A comparison between displacement rate and precipitation on landslides in pelitic flysch formations yielded only high correlation coefficients if more than 30 days of preceding rainfall is summed to the daily values and remains high if longer periods of preceding rainfall are considered (Fig. 5.7 a). MASSEY et al. (2013) reported similar high correlation between pore pressures and rainfall for long periods of preceding rainfall on a complex landslide in marine sand and siltstones in New Zealand. BERTI & SIMONI (2010) showed that pore pressure decay can take longer than it's rise and periods of relatively high porepressures can extend into the dry season. In analogy, once motion is triggered, periods of elevated displacement rates can be long and may extend into the beginning of the dry season.

Low but significant correlation coefficients (below 0.25) with low P-values were obtained for the relationship between precipitation and acceleration if more than 20 and less than 60 days of preceding rainfall were considered (Fig. 5.7 b). This is consistent with InSAR derived seasonal response times of slow moving earthflows in Northern California (HANDWERGER et al., 2013) and a rockslide in the Northern Apennines (CORSINI & MULAS, 2016). On the contrary, periods of acceleration and deceleration are short and if compared to a long window of antecedent rainfall, periods with no acceleration or deceleration will often have high total rainfalls and as a consequence low correlation-coefficients.

A comparison between displacement rate and rainfall for landslides in clay shales yielded moderate correlations with low P-values if more than 30 days and less than

80 days of preceding rainfall were considered (Fig. 5.7 c). No clear relationship between acceleration and deceleration can be observed for any period of antecedent rainfall (Fig. 5.7 d). We observe that, in analogy to periods of acceleration for flysch landslides, periods of high displacement rates were short and corresponded to the spring precipitation 2013 and 2015. On the other hand, acceleration and deceleration were longer and low in magnitude, which is why no correlation exists.

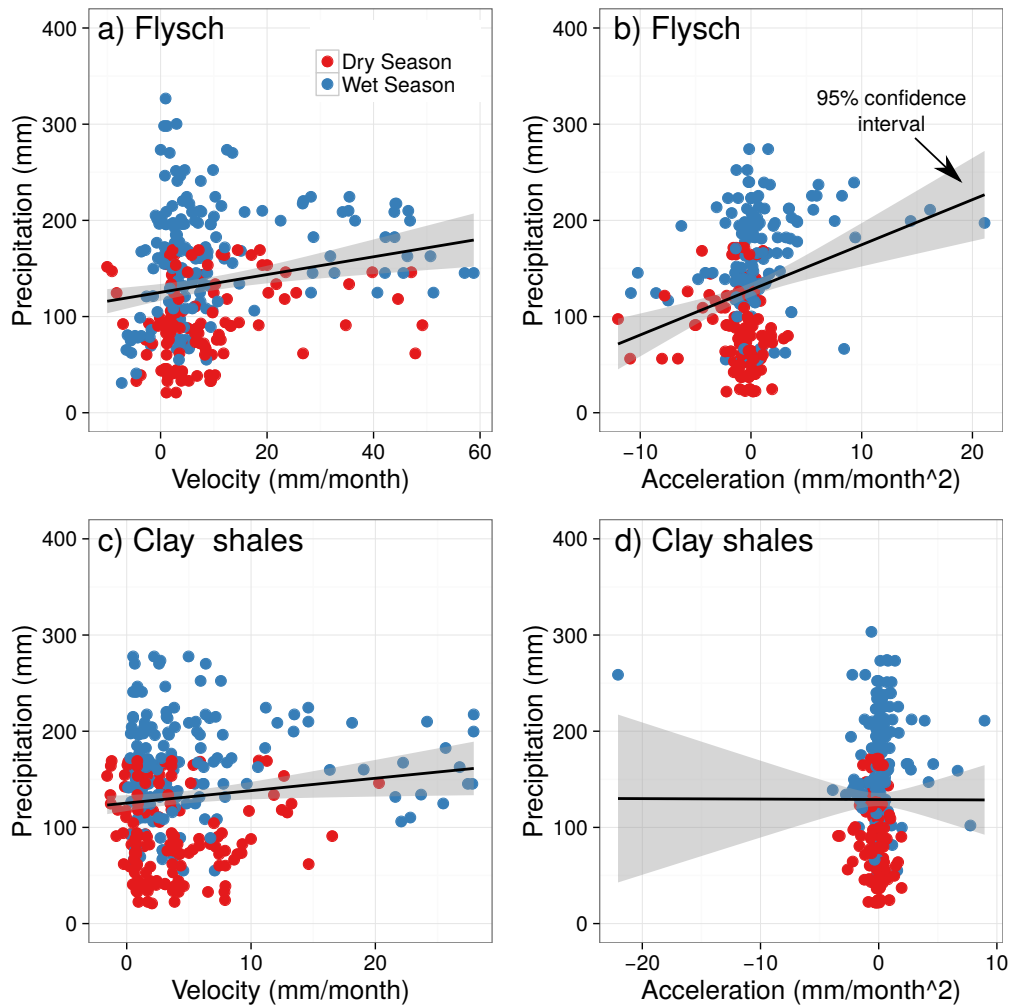


**Figure 5.8:** a) Relationship between Velocity on landslides in pelitic flysch and precipitation if 40 days of preceding rainfall are summed to the daily values. b) Relationship between acceleration and precipitation on flysch landslides. c) Comparison between Velocity and d) acceleration of landslides in chaotic clay shales and precipitation.

Since peak correlation coefficients were measured for periods between 20 and 50 days of preceding rainfall, we compare in the following the velocities and accel-

ations in the two lithotypes to daily precipitation that takes into account the preceding 40 days of rainfall (Fig. 5.8). Landslides in flysch show a weak relationship between velocity and precipitation (Fig. 5.8 a). A possible explanation for this low correlation is that, once displacement is triggered by the increase of pore-water pressure, velocity is regulated by the friction characteristics of the material, landslide geometry and inertia, together with the decay of pore-water pressure that is slower than its rise (BERTI & SIMONI, 2010). Acceleration appears more clearly related to rainfall (Fig. 5.8 b). In all cases, periods of high acceleration were measured during the wet seasons in autumn and spring, while periods of deceleration occurred mostly during the dry summer.

For landslides in chaotic clay shales a moderate relationship between velocity and precipitation can be observed (Fig. 5.8 c), while no correlation was measurable between rainfall and acceleration. Still, also for the landslides in clay shales periods of high velocities and acceleration were measured during the wet season.

## 5.6 Discussion

Slow moving deep-seated landslides can display a wide spectrum of displacement styles that include steady linear displacement, moderate seasonal variation in deformation rates, but they may also transition to catastrophic failure (KEEFER & JOHNSON, 1983; PETLEY & ALLISON, 1997; PETLEY et al., 2005). Only few studies exist that investigated temporal displacement patterns on the catchment scale (ROERING et al., 2005; HANDWERGER et al., 2013; HANDWERGER et al., 2015). In the present study the InSAR derived displacement rates remain typically below 10 cm/year in the downslope direction and only large landslides delivered clear signals. Detailed seasonal variation and linear displacement rates were documented for two years, although deformation maps derived from COSMO SkyMed and Sentinel datasets spanning more than five years suggest that these slow displacements are persistent in time. We would like to line out that these deformations are consistent with seasonal variations in long enduring creeping phases (PETLEY & ALLISON, 1997) and that sudden failure was not measurable in our InSAR survey.

The CSK dataset (2009-2015) allowed us to measure higher velocities on flysch landslides, compared the earthflows in the clay shales in particular during the

year 2013. Independent from landslide typology and bedrock lithology, overall displacement rates are lower in the Sentinel dataset (2015-16) compared to COSMO-SkyMed. However, locally higher displacements rates were resolved by Sentinel due to higher acquisition frequency and good coherence in rural areas.

The higher mean are in line with reports, that state a high number of reactivations of landslides in pelitic flysch units and only few reactivations of earthflows in clay shales (PIZZIOLO et al., 2013; PIZZIOLO et al., 2015). The InSAR derived displacement time series confirm that flysch landslides accelerated faster and reached higher peak velocities, while displacement responses were smoother on the earthflows in clay shales. The fact that the recorded precipitation events during the observation period consisted of sustained rainfall reaching only moderate intensities, suggests that these rainfalls had a critical impact on the landslides in pelitic flysch. It can be hypothesized that the specific rainfall pattern during spring 2013 had different impact on the pore-water pressure regime of the two lithotypes. Different mechanisms may contribute to the observed deformation responses. Hydrological characteristics are in all likelihood significantly different for the slopes in the two lithologies. Pelitic flysch units have higher hydraulic conductivity due to fissures and discontinuities that tend to close with depth but also to open with deformation. The water table can be located at various depth from the surface and exhibit significant seasonal variations (CERVI et al., 2012; BORGATTI et al., 2006). In our view large volumes of infiltrating water are required to raise the pore-water pressure within the pelitic flysch to trigger deformation. On the other hand, clay-shales have lower hydraulic conductivities and although networks of fissures may also be present (BERTI & SIMONI, 2010), they may not persist at depth where pore-water pressures remain high (close to hydrostatic) throughout the year (BERTI et al., 2013). It is possible that failures in clay-shales require rainfall with high intensities rather than long durations.

Both visual analysis of the displacement time series and statistical comparison between acceleration, velocity and precipitation suggests that landslide response times for our landslides vary between 20 and 40 days, which is consistent with the findings of HANDWERGER et al. (2013). COROMINAS et al. (2005) demonstrated that the relation between pore pressure and displacement is complex for periods shorter than 20 days and displacement rates higher than 60 mm/month, which were however not resolvable by our InSAR dataset. Here, we observed a weak but linear relationship

between precipitation and slow deformation rates if more than 20 days of preceding rainfall were taken into account. A possible explanation of the linear nature of this relationship is the fact that only slow deformations were registered and that the aforementioned non-linearities become more important at higher displacement rates and sudden failures, which can not be measured by radar interferometry.

### 5.7 Conclusions

In the present work we document InSAR derived spatio-temporal displacement patterns of 25 landslides in three river catchments of the Northern Apennines, where pelitic turbidites and chaotic clay shale formations constitute most of the substrate. We show that different lithologies host different typologies of landslides. The complex landslides of the pelitic flysch units responded with abrupt acceleration and higher displacement rates to long enduring rainfalls. Chaotic clay shales host classical earthflows that responded with overall lower displacement rates and smoother accelerations. The difference in kinematic behaviour can be explained by different hydrological and geomorphological characteristics. In particular permeability and slope angle, of bedrock and landslide material might play an important role. The landslides where creeping rate was related to precipitation, responded between 20 to 40 days after the onset of the spring precipitation. Because displacement rates were generally low, the relationship between different displacement measures and precipitation is approximately linear if longer periods of preceding rainfall was taken into account.

### 5.8 References

- ADAM, N., EINEDER, M. & KAMPES, B. (2004): Development of a scientific persistent scatterer system: Modifications for mixed ERS/Envisat time series. – ENVISAT & ERS Symposium, **6–10 settembre** (Austria), pp. 1–9; Salzburg.
- BERARDINO, P., FORNARO, G., LANARI, R. & SANSOSTI, E. (2002): A new algorithm for surface deformation monitoring based on small baseline differential SAR interferograms. – *Ieee Transactions On Geoscience and Remote Sensing*, **40** (11), pp. 2375–2383; New York.

- BERTI, M., MARTINA, M. L. V., FRANCESCHINI, S., PIGNONE, S., SIMONI, A. & PIZZILOLO, M. (2012): Probabilistic rainfall thresholds for landslide occurrence using a Bayesian approach. – *Journal of Geophysical Research-earth Surface*, **117** (), F04006;
- BERTI, M., CORSINI, A., FRANCESCHINI, S. & IANNACONE, J. P. (2013): Automated classification of Persistent Scatterers Interferometry time series. – *Natural Hazards and Earth System Sciences*, **13** (8), pp. 1945–1958;
- BERTI, M. & SIMONI, A. (2010): Field evidence of pore pressure diffusion in clayey soils prone to landsliding. – *Journal of Geophysical Research*, **115** (F3), F03001, 1–20; Washington DC.
- BERTI, M. & SIMONI, A. (2012): Observation and analysis of near-surface pore-pressure measurements in clay-shales slopes. – *Hydrological Processes*, **26** (14), pp. 2187–2205; New York.
- BERTOLINI, G., CASAGLI, N., ERMINI, L. & MALAGUTI, C. (2004): Radiocarbon data on lateglacial and Holocene landslides in the Northern Apennines. – *Natural Hazards*, **31** (3), European Geophys Soc;
- BERTOLINI, G., GUIDA, M. & PIZZILOLO, M. (2005): Landslides in Emilia-Romagna region (Italy); strategies for hazard assessment and risk management. – *Landslides*, **2** (4), pp. 302–312; Heidelberg.
- BETTELLI, G. & PANINI, F. (1992): Liguridi, melanges e tettoniti nel complesso caotico lungo la “linea del Sillaro” (Appennino settentrionale, Province di Firenze e Bologna). – *Mem. Descr. Carta Geol. d’It*, **XI** (VI), pp. 387–415; Roma.
- BOCCALETTI, M., ELTER, P. & GUAZZONE, G. (1971): Plate Tectonic Models for the Development of the Western Alps and Northern Apennines. – *Nature*, **234** (49), pp. 108–111; Oxford.
- BOGAARD, T. A. & GRECO, R. (2016): Landslide hydrology: from hydrology to pore pressure. – *Wiley Interdisciplinary Reviews-water*, **3** (3), pp. 439–459;
- BORGATTI, L., CORSINI, A., BARBIERI, M., SARTINI, G., TRUFFELLI, G., CAPUTO, G. & PUGLISI, C. (2006): Large reactivated landslides in weak rock masses; a case study from the Northern Apennines (Italy). – *Landslides*, **3** (2), pp. 115–124; Berlin, New York etc.

- BÜRGMANN, R., ROSEN, P. A. & FIELDING, E. J. (2000): Synthetic aperture radar interferometry to measure Earth's surface topography and its deformation. – Annual Review of Earth and Planetary Sciences, **28** (), pp. 169–209;
- CERVI, F., RONCHETTI, F., MARTINELLI, G., BOGAARD, T. A. & CORSINI, A. (2012): Origin and assessment of deep groundwater inflow in the Ca' Lita landslide using hydrochemistry and in situ monitoring. – Hydrology and Earth System Sciences, **16** (11), pp. 4205–4221;
- CLEVELAND, W. S. & DEVLIN, S. J. (1988): Locally Weighted Regression - An Approach To Regression-analysis By Local Fitting. – Journal of the American Statistical Association, **83** (403), pp. 596–610;
- CLEVELAND, W. S. (1979): Robust Locally Weighted Regression and Smoothing Scatterplots. – Journal of the American Statistical Association, **74** (368), pp. 829–836; New York.
- COLESANTI, C., FERRETTI, A., PRATI, C. & ROCCA, F. (2003): Monitoring landslides and tectonic motions with the Permanent Scatterers Technique. – Engineering Geology, **68** (1-2), pp. 3–14; Amsterdam.
- COLESANTI, C. & WASOWSKI, J. (2006): Investigating landslides with space-borne synthetic aperture radar (SAR) interferometry. – Engineering Geology, **88** (3-4), pp. 173–199; Amsterdam.
- COROMINAS, J., MOYA, J., LEDESMA, A., LLORET, A. & GILI, J. A. (2005): Prediction of ground displacements and velocities from groundwater level changes at the Vallcebre landslide (Eastern Pyrenees, Spain). – Landslides, **2** (2), pp. 83–96;
- CORSINI, A., FARINA, P., ANTONELLO, G., BARBIERI, M., CASAGLI, N., COREN, F., GUERRI, L., RONCHETTI, F., STERZAI, P. & TARCHI, D. (2006): Space-borne and ground-based SAR interferometry as tools for landslide hazard management in civil protection. – International Journal of Remote Sensing, **27** (12), pp. 2351–2369; London.
- CORSINI, A. & MULAS, M. (2016): Use of ROC curves for early warning of landslide displacement rates in response to precipitation (Piagneto landslide, Northern Apennines, Italy). – Landslides, (), pp. 1–12;

- CRUDEN, D. M. & VARNES, D. J. (1996): Landslide types and processes. – In: TURNER A. K. & Schuster, R. L. [ed.] (1996): Landslides: investigation and mitigation, special report 247, pp. 36–75; Washington DC (Transportation Research Board, National Research Council).
- FERRETTI, A., PRATI, C. & ROCCA, F. (2001): Permanent scatterers in SAR interferometry. – *Ieee Transactions On Geoscience and Remote Sensing*, **39** (1), pp. 8–20; New York.
- FERRETTI, A., FUMAGALLI, A., NOVALI, F., PRATI, C., ROCCA, F. & RUCCI, A. (2011): A New Algorithm for Processing Interferometric Data-Stacks: SqueeSAR. – *Ieee Transactions On Geoscience and Remote Sensing*, **49** (9), pp. 3460–3470; Piscataway.
- HANDWERGER, A. L., ROERING, J. J. & SCHMIDT, D. A. (2013): Controls on the seasonal deformation of slow-moving landslides. – *Earth and Planetary Science Letters*, **377–378** (1), pp. 239–247; Amsterdam.
- HANDWERGER, A. L., ROERING, J. J., SCHMIDT, D. A. & REMPEL, A. W. (2015): Kinematics of earthflows in the Northern California Coast Ranges using satellite interferometry. – *Geomorphology*, **246** (), pp. 321–333;
- HILLEY, G. E., BURGMANN, R., FERRETTI, A., NOVALI, F. & ROCCA, F. (2004): Dynamics of slow-moving landslides from permanent scatterer analysis. – *Science*, **304** (5679), pp. 1952–1955;
- HOOPER, A., ZEBKER, H., SEGALL, P. & KAMPES, B. (2004): A new method for measuring deformation on volcanoes and other natural terrains using InSAR persistent scatterers. – *Geophysical Research Letters*, **31** (23), p. L23611; Washington DC.
- HOOPER, A., SEGALL, P. & ZEBKER, H. (2007): Persistent scatterer interferometric synthetic aperture radar for crustal deformation analysis, with application to Volcan Alcedo, Galapagos. – *Journal of Geophysical Research-solid Earth*, **112** (B7), B07407; Washington DC.
- HOOPER, A. (2008): A multi-temporal InSAR method incorporating both persistent scatterer and small baseline approaches. – *Geophysical Research Letters*, **35** (16), p. L16302; Washington DC.

- HOOPER, A., BEKAERT, D., SPAANS, K. & ARIKAN, M. (2012): Recent advances in SAR interferometry time series analysis for measuring crustal deformation. – *Tectonophysics*, **514** (), pp. 1–13;
- HUNGR, O., LEROUEIL, S. & PICARELLI, L. (2012): Varnes Classification of landslide types, an update. – In: EBERHARDT, E., FROESE, C., TURNER, A. K. & LEROUEIL, S. [eds.] (2012): *Landslides and Engineering Slopes: Protecting Society through Improved Understanding* (Proceedings of the 11th international and 2nd North American symposium on landslides and engineered slopes, Banff, Canada, 3–8 June 2012, pp. 47–58; London (CRC Press).
- HUNGR, O., EVANS, S. G., BOVIS, M. J. & HUTCHINSON, J. N. (2001): A review of the classification of landslides of the flow type. – *Environmental & Engineering Geoscience*, **7** (3), pp. 221–238; College station.
- IASIO, C., NOVALI, F., CORSINI, A., MULAS, M., BRANZANTI, M., BENEDETTI, E., GIANNICO, C., TAMBURINI, A. & MAIR, V. (2012): Cosmo Skymed High Frequency - High Resolution Monitoring of An Alpine Slow Landslide, Corvara In Badia, Northern Italy. – 2012 Ieee International Geoscience and Remote Sensing Symposium (igarss), (), pp. 7577–7580;
- IVERSON, R. M. (2000): Landslide triggering by rain infiltration. – *Water Resources Research*, **36** (7), pp. 1897–1910;
- IVERSON, R. M. (2005): Regulation of landslide motion by dilatancy and pore pressure feedback. – *Journal of Geophysical Research-earth Surface*, **110** (F2), F02015;
- IVERSON, R. M. & MAJOR, M. M. (1987): Rainfall, Groundwater-flow, and Seasonal Movement At Minor Creek Landslide, Northwestern California - Physical Interpretation of Empirical Relations. – *Geological Society of America Bulletin*, **99** (4), pp. 579–594;
- KAMPES, B. & USAI, S. (1999): “Doris: The delft object-oriented radar interferometric software” In: 2nd International Symposium on Operationalization of Remote Sensing, Enschede, The Netherlands vol. 16 Citeseer, 1999, p. 20.

- KEEFER, D. K. & JOHNSON, A. M. (1983): Earth flows; morphology, mobilization, and movement (Geological survey professional paper 1264). – 56 pp.; Reston (U. S. Geological Survey).
- KRZEMINSKA, D. M., BOGAARD, T. A., ASCH, T. W. J. van & BEEK, L. P. H. van (2012): A conceptual model of the hydrological influence of fissures on landslide activity. – *Hydrology and Earth System Sciences*, **16** (6), pp. 1561–1576;
- MASSEY, C. I., PETLEY, D. N. & MCSAVENEY, M. J. (2013): Patterns of movement in reactivated landslides. – *Engineering Geology*, **159** (), pp. 1–19;
- MASSONNET, D. & FEIGL, K. L. (1998): Radar interferometry and its application to changes in the earth's surface. – *Reviews of Geophysics*, **36** (4), pp. 441–500;
- PAVAN, V., TOMOZEIU, R., CACCIAMANI, C. & DI LORENZO, M. (2008): Daily precipitation observations over Emilia-Romagna: mean values and extremes. – *International Journal of Climatology*, **28** (15), pp. 2065–2079;
- PETLEY, D. N., MANTOVANI, F., BULMER, M. H. & ZANNONI, A. (2005): The use of surface monitoring data for the interpretation of landslide movement patterns. – *Geomorphology*, **66** (1-4), Int Assoc Geomorphologists;
- PETLEY, D. N. & ALLISON, R. J. (1997): The mechanics of deep-seated landslides. – *Earth Surface Processes and Landforms*, **22** (8), pp. 747–758; Malden.
- PICOTTI, V. & PAZZAGLIA, F. J. (2008): A new active tectonic model for the construction of the Northern Apennines mountain front near Bologna (Italy). – *Journal of Geophysical Research-solid Earth*, **113** (B8), B08412;
- PINI, G. A. (1999): Tectonosomes and olistostromes in the argille scagliose of the Northern Apennines, Italy. – *Special Paper - Geological Society of America*, **335** (1), pp. 1–70; Boulder.
- PIZZIOLO, M., MONNI, A. & PRIMERANO, S. (2013): Con le piogge anomale frane da record. – *Ecoscienza*, **2013** (2), pp. 12–14; Bologna.

- PIZZIOLO, M., BERNARDI, M., DANIELE, G., GENERALI, M. & PIACENTINI, D. (2015): Landslide Occurrences During the High-Intensity Rainfall Event of March-April 2013 in the Emilia-Romagna Region (North Apennines, Italy). – Engineering Geology For Society and Territory, Vol 5: Urban Geology, Sustainable Planning and Landscape Exploitation, (), IAEG;
- RICCI LUCCHI, F. (1986): The Oligocene to Recent foreland basins of the Northern Apennines. – In: A., P. & HOMEWOOD, P. [eds.] (1986): Special Publication of the International Association of Sedimentologists, pp. 105–139; Oxford (Blackwell).
- ROERING, J. J., KIRCHNER, J. W. & DIETRICH, W. E. (2005): Characterizing structural and lithologic controls on deep-seated landsliding: Implications for topographic relief and landscape evolution in the Oregon Coast Range, USA. – Geological Society of America Bulletin, **117** (5-6), pp. 654–668; Boulder.
- RONCHETTI, F., BORGATTI, L., CERVI, F., LUCENTE, C. C., VENEZIANO, M. & CORSINI, A. (2007): The Valoria landslide reactivation in 2005-2006 (Northern Apennines, Italy). – Landslides, **4** (2), pp. 189–195;
- ROSEN, P. A., HENSLEY, S., PELTZER, G. & SIMONS, M. (2004): Updated repeat orbit interferometry package released. – Eos Trans. AGU, **85** (5), pp. 47–47; Malden.
- SANDWELL, D., MELLORS, R., TONG, X., WEI, M. & WESSEL, P. (2011): Open radar interferometry software for mapping surface deformation. – Eos, Transactions American Geophysical Union, **92** (28), pp. 234–234;
- SCHMIDT, D. A. & BÜRGMANN, R. (2003): Time-dependent land uplift and subsidence in the Santa Clara valley, California, from a large interferometric synthetic aperture radar data set. – J. Geophys. Res. **108** (B9), pp. 1–13; International.
- SERVIZIO GEOLOGICO, SISMICO E DEI SUOLI DELLA REGIONE EMILIA-ROMAGNA (2014): Carta Inventario delle frane a scala 1:10000 della Regione Emilia-Romagna. URL: <http://ambiente.regione.emilia-romagna.it/geologia/cartografie/webgis-banchedati/cartografia-dissesto-idrogeologico>; –.

- SIMONI, A., PONZA, A., PICOTTI, V., BERTI, M. & DINELLI, E. (2013): Earth-flow sediment production and Holocene sediment record in a large Apennine catchment. – *Geomorphology*, **188** (1), pp. 42–53; Amsterdam.
- TOMOZEIU, R., BUSUIOC, A., MARLETTO, V., ZINONI, F. & CACCIAMANI, C. (2000): Detection of changes in the summer precipitation time series of the region Emilia-Romagna, Italy. – *Theoretical and Applied Climatology*, **67** (3-4), pp. 193–200;
- TOMOZEIU, R., LAZZERI, M. & CACCIAMANI, C. (2002): Precipitation fluctuations during the winter season from 1960 to 1995 over Emilia-Romagna, Italy. – *Theoretical and Applied Climatology*, **72** (3-4), pp. 221–229;
- USAI, S. (2003): A least squares database approach for SAR interferometric data. – *Ieee Transactions On Geoscience and Remote Sensing*, **41** (4), pp. 753–760;
- VANNUCCHI, P., MALTMAN, A., BETTELLI, G. & CLENNELL, B. (2003): On the nature of scaly fabric and scaly clay. – *Journal of Structural Geology*, **25** (5), pp. 673–688; Oxford.
- WASOWSKI, J. & BOVENGA, F. (2014): Investigating landslides and unstable slopes with satellite Multi Temporal Interferometry: Current issues and future perspectives. – *Engineering Geology*, **174** (), pp. 103–138;
- WRIGHT, T. J., PARSONS, B. E. & LU, Z. (2004): Toward mapping surface deformation in three dimensions using InSAR. – *Geophysical Research Letters*, **31** (1), p. L01607;

## 6 Discussion and General conclusions

The general findings of the dissertation can be separated into two main aspects, one of which addresses technical issues related to the application of radar interferometry to the measurement of slow moving landslides. The second aspect treats geological and geomorphological questions that can be answered by the different InSAR datasets.

From a technical point of view, the experiments that analysed how InSAR results vary given the DEM, illustrate that local InSAR results can be improved by using an accurate DEM to forward model the topographic phase. Although high quality elevation data might help in many cases to obtain a better final interferometric results, it did not help to overcome widespread problems due to decorrelation in our study area. The analysis of the case study of Ripoli and Santa Maria Maddalena yielded the insight that InSAR derived displacements are accurate both in space and time. The displacements compare well to external monitoring data of inclinometer and GPS measurements when the latter datasets were projected in the satellite coordinate system. Furthermore, setting the InSAR reference area close to the deforming region improved accuracy of the displacement signals. The influence of atmospheric artefacts seem to play only a minor role, when looking at a single case. This is most likely due to the similar atmospheric conditions over the stable reference area and over the moving landslide. In the regional landslide analysis, it was possible to combine interferograms that were formed on different satellite tracks and in different viewing geometries. On the one hand, this reduced the detail in the spatial displacement signal, because only points that were common to all datasets were used for this approach. On the other hand, it permitted to constrain better real accelerations and decelerations, because the number of observations (interferograms) for single timesteps is higher. Another interesting aspect, is the high quality of the data that was acquired by the new ESA satellite Sentinel 1A. Due to the high acquisition frequency (ca. 8 days in our datasets) compared to Cosmo SkyMed (ca.

16 days in our datasets), and the longer wavelength, it was possible to obtain a clear signal for cases that were completely decorrelated in Cosmo SkyMed datasets.

From a geological point of view, the case study of Ripoli and Santa Maria Maddalena illustrate that tunneling under deep seated dormant landslides can trigger their deformation. The InSAR results resolved clear downslope displacements and not only subsidence. Deformation rates picked up as the tunnel front approached the landslides complexes and attenuated as the excavation proceeded away from the landslides. Clear correlations exist between tunnel position, excavation rate and displacements, while precipitation and porepressure seem to play only minor roles. InSAR revealed only small and localized deformation before the excavation started and registered the slow down of landslide motion after excavation works ceased. However locally the deformation rates remained high throughout the years 2015-2016 and did not return to values that were measured before the excavation. It is interesting to note that the deformation style in time is different for this case study compared to the precipitation induced displacements of the regional InSAR survey. While for the latter study seasonal deformation occurred during the spring months of 2013, at Ripoli and Santa Maria Maddalena displacement picked up in 2011, remained high during 2012, slowed briefly down during spring 2013 and accelerated again during summer 2013. These differences suggest that the underlying datastructure of our interferogram network did not bias our inverted time series and that the resolution of our datasets is high enough to resolve well non linear motion.

For the regional study in chapter 5, steep accelerations were measured on composite rockslides in the pelitic flysch formations, which are present in the Northern Apennines. On the contrary, earthflows in the chaotic clay shales showed smoother accelerations and deceleration in time. As a consequence, periods of high rainfall have a higher correlation with periods of acceleration for the flysch landslides, while correlation between landslide acceleration and rainfall is lower for the earthflows. The different behavior is caused by a combination of hydraulic properties of the landslide material and the style of precipitation. Slow moving rock slides in the flysch deposits have a higher permeability and hence long enduring rainfalls are necessary to raise the water table from a relative deep position close to the ground surface. This causes a relative high rise in normal pore-pressure compared to the condition in the dry period and initialize displacements. On the contrary, earthflows in the chaotic clay shales are less permeable and the water table is situated

also during the dry season only a few meters from the ground surface. Hence it might take longer to rise the water table, but the variation between dry and wet season is relatively small. Displacements remain lower and the acceleration appears smoother. After the end of the rainy season, the rockslides drain and decelerate also faster compared to the earthflows in the clay shales. This difference of behaviour is however only visible, if the spring period is characterized by enduring, persistent rainfalls, which are necessary to saturate the landslide bodies in the pelitic Flysch formations.

Concluding it can be stated that InSAR is a useful technique that helped to integrate our knowledge regarding slow moving landslides in the Northern Apennines. However, care needs to be taken during InSAR processing and interpretation of final timeseries products, if landslides are the focus of the study. In particular, different parameters for unwrapping and pixel selection have to be tested in order to obtain precise displacements in time. Also, a stable reference area has to be chosen as close as possible to the landslide in question (chapter 2). An accurate digital elevation model can help to improve the InSAR results, although problems related to overall low coherence in rural areas can not be mitigated. Large jumps in perpendicular baselines can introduce a temporal signal that is proportional to the DEM error and maybe misinterpreted as landslide deformation, in particular if this adjustment of the satellite orbit occurs during the wet season (chapter 3). Once processing parameters were optimized for a given landslide, the InSAR derived displacements compare well to conventional monitoring data and landslide displacement that was induced by tunneling was resolved well both in space and time by the technique. For large tunnel projects, care should be taken during the selection of the trace. In particular the interaction between the excavation and old dormant landslides should be considered, although the correct interpretation of ancient slope movements is prone to large uncertainties. Remote sensed deformation data might in selected cases prove helpful during the design- and construction phases (chapter 4). Different deformation responses were measured on landslides that are hosted in two common lithologies of the study area. Deformation occurred in flysch following long enduring rainfalls although long term repeated seasonal creep was not resolved due to the low acquisition frequencies of Envisat and Cosmo SkyMed. However, the results obtained by the C-band satellite Sentinel, which acquires since late 2014

images at a temporal rate of less than 12 days, were promising and suggest that InSAR will become a powerful tool for landslide monitoring (chapter 5).